Nano Research
2023, 16(7): 8684–8711

ISSN 1998-0124 CN 11-5974/O4
https://doi.org/10.1007/s12274-023-5670-6

Self-supported transition metal chalcogenides for oxygen evolution

Ting Zhang[1,2], Jianrui Sun[2] (✉), and Jingqi Guan[1] (✉)

[1] Institute of Physical Chemistry, College of Chemistry, Jilin University, 2519 Jiefang Road, Changchun 130021, China
[2] School of Chemistry and Life Science, Changchun University of Technology, Changchun 130012, China

Received: 7 February 2023 / **Revised:** 13 March 2023 / **Accepted:** 14 March 2023

ABSTRACT

Owing to stable spatial framework and large electrochemical interface, self-supported transition metal chalcogenides have been actively explored in renewable energy fields, especially in oxygen evolution reaction (OER). Here, we review the research progress of self-supported transition metal chalcogenides (including sulfides, selenides, and tellurides) for the OER in recent years. The basic principle and evaluation parameters of OER are first introduced, and then the preparation methods of transition metal chalcogenides on various self-supporting substrates (including Ni foam (NF), carbon cloth (CC), carbon fiber paper (CFP), metal mesh/plate, etc.) are systematically summarized. Subsequently, advanced optimization strategies (including interface and defect engineering, heteroatom doping, edge engineering, surface morphology engineering, and construction of heterostructure) are introduced in detail to improve the inherent catalytic activity of self-supported electrocatalysts. Finally, the challenges and prospects of developing more promising self-supported chalcogenide electrocatalysts are proposed.

KEYWORDS

self-supported chalcogenide, oxygen evolution reaction (OER), interface and defect engineering, heteroatom doping, heterostructure

1 Introduction

Nowadays, with the rapid consumption of primary energy fossil fuels, we are facing energy crisis, environmental pollution, and abnormal climate change, which force us to develop efficient energy storage and conversion technologies without delay [1–9]. Hydrogen is recognized as an energy carrier in the future sustainable system because of its renewability, high energy storage capacity, and high environmental friendliness [10–14]. Among current hydrogen production methods, electrochemical water splitting is an eco-friendly, safe, and simple method, which can be applied to commercial large-scale hydrogen production [15–20]. However, oxygen evolution reaction (OER) as the anodic half reaction during water splitting involves a multi-step and four-electron-transfer process, resulting in a high energy barrier to drive the reaction [21–24]. Although commercial RuO_2 and IrO_2 are high-efficiency electrocatalysts for the OER, their scarcity and high cost in the earth's crust hinder their wide commercial application [25–28]. Therefore, it is very urgent to develop non noble metal OER electrocatalysts with soil abundance, low price, high efficiency, and durability.

In recent years, non-noble-metal-based electrocatalysts such as metal oxides [29–33], metal hydroxides [34–37], sulfides [38–42], selenides [43–45], and tellurides [46–49] have been used as highly active OER electrocatalysts. During the preparation of the electrode, nano granular OER electrocatalysts are usually bonded to the glassy carbon electrode by a binder [50–52]. Nafion is used as a common polymer adhesive to ensure that the prepared electrocatalyst has good adhesion to the conductive matrix [53, 54]. However, the introduction of polymer adhesive will produce the following disadvantages: (I) it may lead to aggregation, which is not conducive to the gas adsorption and desorption process [55]; (II) the specific surface area is too small to provide a large number of active sites [56, 57]; (III) the mixed binder will inhibit the charge transfer efficiency, reduce the conductivity, and greatly affect the electrocatalytic activity [58, 59]. Therefore, it is very important to construct electrocatalysts as an independent self-supporting electrode without adhesive.

Transition metal chalcogenides have been developed as a kind of promising electrocatalysts for water splitting due to their unique physical and chemical properties, rich active sites, good conductivity, controllable electronic properties, and relatively mild manufacturing conditions [60–62]. However, most of the prepared transition metal chalcogenides are in powder form, and the disadvantages of poor durability and low catalytic OER activity are obvious, which greatly hinder the electrocatalytic application in water splitting [63–66]. Compared with the traditional powder catalyst, the growth of catalytically active electrodes on the conductive substrate has the following advantages: (i) The substrate material can disperse the catalyst, which is conducive to the gas adsorption and desorption process; (ii) without using the adhesive, the catalytic material can be closely combined with the conductive substrate, which not only simplifies the preparation process, but also ensures the rapid transfer of charge and improves the electrocatalytic activity; (iii) the conductive substrate enables high loading of the active components, providing abundant reactive active sites. Independent self-supporting chalcogenide electrocatalysts used as electrodes for commercial electrolytic cells have been widely reported [67–71]. Electrocatalysts are grown *in situ* on self-supporting conductive substrates, such as metal foam

Address correspondence to Jianrui Sun, goodluck@ccut.edu.cn; Jingqi Guan, guanjq@jlu.edu.cn

(such as Ni/Cu foam), carbon cloth (CC), graphite plate, carbon fiber paper (CFP), etc. Conductive materials can not only provide effective electron transport channels, but also increase the surface area of the electrocatalysts [72, 73].

Until now, there are seldom relevant reviews focusing on the development of self-supported transition metal chalcogenides toward OER. In this review, the research progress of self-supporting transition metal chalcogenide electrocatalysts is reviewed, with emphasis on their catalytic OER performance. The basic principles and evaluation parameters of OER are first introduced, and the preparation methods of various independent electrocatalysts are then introduced. Therewith, self-supporting transition metal sulfides, transition metal selenides, and transition metal tellurides are discussed for the OER. Afterwards, the advanced optimization strategies (including interface and defect engineering, and heteroatom doping) are introduced in detail to improve the inherent catalytic activity of self-supporting electrocatalysts. Finally, the challenges and prospects of the design and construction of self-supporting chalcogenide electrocatalysts are suggested, providing a direction for further research.

2 Basic principles and evaluation parameters of OER

2.1 OER mechanism

OER occurs on the anode of water electrolysis, and the possible mechanisms are explained in four steps. First, the adsorption vacancy on catalyst surface (*) combines with water or OH^- to form OH* ((Eqs. (1) or (5)). Second, OH* decomposes to form O* (Eqs. (2) or (6)). Third, the generated O* reacts with water or OH^- to generate OOH* (Eqs. (3) or (7)). Finally, O_2 is immediately created (Eq. (4)) under acidic conditions, while it needs to be combined with OH^- to release O_2 under alkaline conditions. Different from the hydrogen evolution reaction (HER), OER is a process of four electron transfer, involving intermediates such as OH*, O*, and OOH* [74, 75].

Under acidic conditions

$$* + H_2O \rightarrow OH^* + H^+ + e^- \tag{1}$$

$$OH^* + H_2O \rightarrow O^* + H_2O + H^+ + e^- \tag{2}$$

$$O^* + H_2O \rightarrow OOH^* + H^+ + e^- \tag{3}$$

$$OOH^* \rightarrow * + O_2 + H^+ + e^- \tag{4}$$

Overall

$$2H_2O \rightarrow 4H^+ + O_2 + 4e^- \tag{5}$$

Under basic conditions

$$* + OH^- \rightarrow OH^* + e^- \tag{6}$$

$$OH^* + OH^- \rightarrow O^* + H_2O + e^- \tag{7}$$

$$O^* + OH^- \rightarrow OOH^* + e^- \tag{8}$$

$$OOH^* + OH^- \rightarrow * + O_2 + H_2O + e^- \tag{9}$$

Overall

$$4OH^- \rightarrow 2H_2O + O_2 + 4e^- \tag{10}$$

Unlike HER electrolysis, OER is a heterogeneous reaction involving multiple steps, and the OER dynamics is much more complex and slower than HER (the theoretical OER precipitation voltage is 1.23 V) [76]. The mechanism of OER under alkaline conditions includes the adsorption evolution mechanism (AEM) and the lattice oxygen evolution mechanism (LOM) (Figs. 1(a) and 1(b)) [77]. For AEM, the activity of the catalyst is tightly linked to the adsorption energy between the metal active site and the OER intermediate. Therefore, it is theoretically possible to obtain the best active catalyst by adjusting the adsorption energy in the four-step reaction. For the reaction at LOM, O–O coupling occurs on the lattice oxygen, but the lattice oxygen directly involved in the oxygen precipitation will affect the stability of the catalyst. Thus, the OER is more difficult to occur than the HER.

To understand the OER mechanism more deeply, density functional theory (DFT) is proposed [65]. DFT calculation shows that there is a scale between the adsorption energies of OOH* and OH* intermediates, which can be used to evaluate the reaction kinetics and electrocatalytic activity of catalysts by the change of Gibbs free energy (ΔG) of OER pathway, and the difference value ($\Delta G_{O^*} - \Delta G_{OH^*}$) is suggested as the description of OER activity [80]. The adsorption free energy of intermediates in each of the four OER steps is various, which will affect the OER performance (Figs. 1(c) and 1(d)). The most unfavorable reaction step is considered as the OER potential determining step. Xu et al. synthesized carbon cloth supported $Co(Zn)S_2$ by co-deposition method and subsequent sulfation strategy [81]. X-ray photoelectron spectroscopy (XPS) studies showed that when Zn was added to the CoS_2 nanoarray, the formed Co (Zn) OOH + SO_4^{2-} and CoOOH + SO_4^{2-} served as the real active sites of OER. DFT calculations showed that Zn doping reduced the adsorption free energy of OER intermediates at the Co site. In addition, the free energy of Co (Zn) OOH + SO_4^{2-} is 0.05 eV lower than that of CoOOH + SO_4^{2-}, confirming that Zn doping effectively improved the OER catalytic activity. During OER, the sulfide surface will reconstruct, and hybridization of appropriate components that combine their individual advantages and exert synergistic effects is considered as an effective strategy to enhance OER activity of metal chalcogenides. Yan et al. prepared Co_9S_8@Fe_3O_4 heterojunction nanosheet array by two-step hydrothermal reaction [82]. XPS results showed the phase transition of Co surface structure in a dynamic process. In addition, the X-ray absorption fine-structure (XAFS) spectra indicated that the metal Co sites acted as active sites for surface reconstruction rather than Fe sites. In the electrocatalyst reconstruction process, the Co species in the Co_9S_8@Fe_3O_4 heterostructure were transformed into CoOOH species, which are called true active sites. The surface reconstruction enhanced hydrophilicity, improved conductivity, and lowered energy barrier, thus promoting OER performance.

2.2 Key evaluation parameters for the OER

2.2.1 *Overpotential*

The electrocatalytic OER can proceed at the equilibrium theoretical potential of 1.23 V (vs. RHE). However, it requires extra energy (overpotential, η) to surpass the kinetic barrier in reality. That is, when the catalytic reaction reaches a certain current (i), the actual required voltage (E_i) exceeds the theoretical voltage (E_t), and the applied potential can be expressed as Eq. (11)

$$\eta_i = E_i - E_t \tag{11}$$

The overpotential is one of the important parameters for measuring the OER performance. Under normal conditions, the overpotential (η_{10}) required to achieve a current density of 10 $mA \cdot cm^{-2}$ has been widely used to evaluate the activity of the catalyst [83, 84]. Using Prussian blue analog CoNiFe PBA as the precursor, Cheng et al. prepared a nano cubic structure electrocatalyst by hydrothermal treatment combined with evaporative sulfurization [85]. The optimized CoNiFe-350 °C

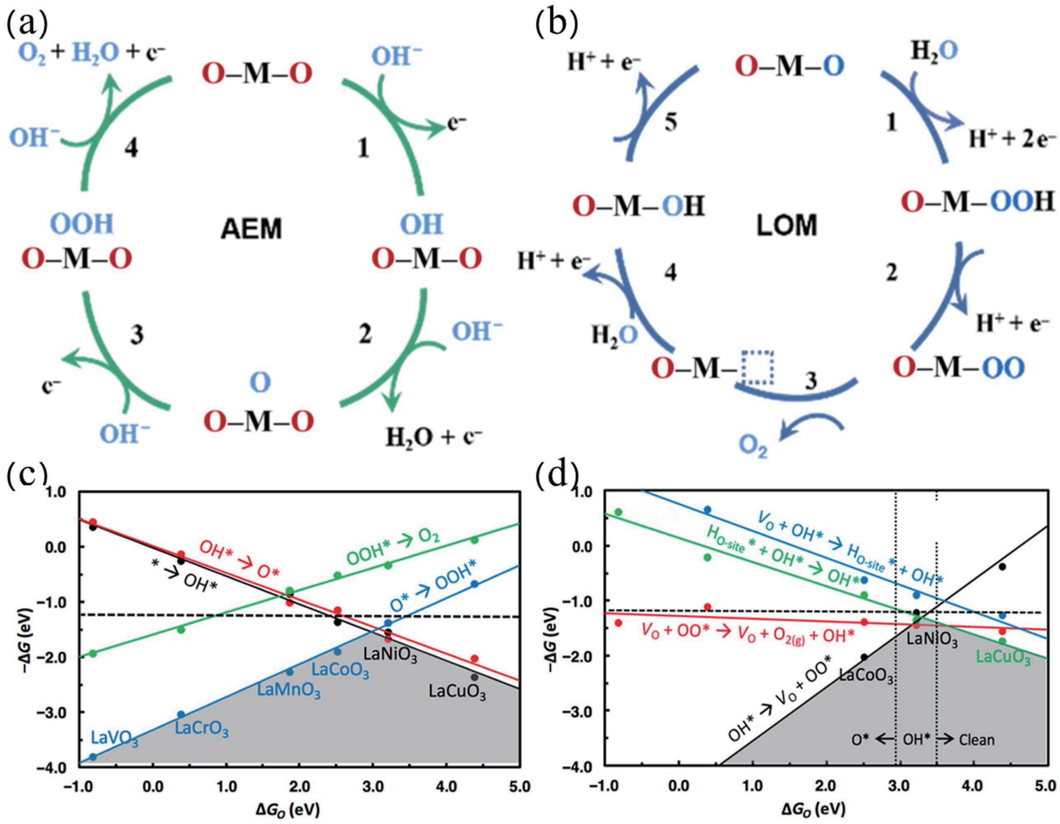

Figure 1 (a) Classic AEM mechanism. (b) LOM mechanism. Reproduced with permission from Ref. [78], © The Royal Society of Chemistry 2023. Negative reaction free energies vs. ΔG_O of each OER step via (c) AEM and (d) LOM. Reproduced with permission from Ref. [79], © American Chemical Society 2018.

catalyst showed excellent OER performance and durability. In alkaline medium, it has a low η_{10} of 288 mV. Wang et al. synthesized CoS_x/carbon nanotubes (CNT)-700 electrocatalyst on carbon nanotubes by coprecipitation and calcination [86]. The optimized electrocatalyst was obtained by adjusting the ratio of Co^{3+} and Co^{2+} and the calcination time, which showed an η_{10} of 320 mV in 1.0 M KOH. Under a specific current density, the lower the overpotential of the catalyst, the higher the catalytic ability for a target reaction [87]. Ma et al. used a vapor deposition method to grow CoFe PBA on carbon nanotubes as a precursor, and then combined with sulfidation to obtain S-CoFe/CNT [88]. In 1.0 M KOH, the catalyst showed an η_{10} of 258 mV.

2.2.2 *Tafel slope*

The Tafel slope is another key factor to analyze the kinetics and reveal the reaction mechanism of the OER process [89]. The Tafel equation can be used to express the relationship between overpotential and current density (Eq. (12)), in which b is the Tafel slope; j refers to the current density; and a is a constant. The smaller the Tafel slope is, the faster the current density increases when the applied potential increases slightly [90]. Catalysts with different activities show different free energies in different paths of O_2 generation, and the most energy required is the rate-determining step (RDS). Since the complex behavior of OER forms many reaction intermediate materials, it is challenging to derive the surface fraction coverage of the intermediates as a function of the reaction rate constant. OER theoretical analysis by Alobaid et al., OER dynamics demonstrated the formation of intermediate adsorbed peroxides (HOO) as a rate determination step, consistent with the 48.4 mV·dec^{-1} Tafel slope obtained from their calculated measurements [91]. Tafel slope can assess dynamics, and dynamics is the basis for electrochemistry.

$$\eta = b \log j + a \tag{12}$$

2.2.3 *Turnover frequency (TOF)*

TOF is used to characterize the intrinsic catalytic activity of active sites in electrocatalysts [92, 93]. The TOF value is usually derived from Eq. (13), where J is obtained at 95% iR-corrected overpotential of 300 mV, normalized by geometric area of working electrode; A is the geometric area of working electrode; F is the Faraday constant and η is the Faradaic efficiency (FE) calculated from equation ($\eta = 4F \times nO_2/Q$). n is the mole number of metal on the electrode. TOF can be used to calculate the increase of electron sites per unit time, which is another important basis for judging the overall catalytic performance [94, 95]. Prabakar et al. prepared $Cu_{2-x}S$/Co nanosheet electrocatalyst on Ni foam (NF) by chemical deposition and hydrothermal synthesis, showing a TOF of 0.038 s^{-1} at an overpotential of 300 mV [96]

$$\mathrm{TOF} = J \times A \times \eta / (4 \times n \times F) \tag{13}$$

2.2.4 *Faradaic efficiency*

In the electrochemical OER, FE is defined as the percentage between the experimental oxygen production and the theoretical oxygen production, that is, the electron conversion efficiency of oxygen generation [97–99], which is affected by temperature, applied voltage, electrolyte concentration, and other experimental conditions. The actual oxygen production rate can be measured by gas chromatography. The FE calculation is given by Eq. (14), where m is the actual molar number of the generator; n is the number of reaction electrons; F is the Faraday constant; I is the current; and t is the time. Li et al. prepared nitrogen doped porous $WC/Co_3W_3N/Co@NC$ catalyst by epitaxial growth and calcination. The Faraday efficiency of OER is 97.4% within 120 min by bubble extraction method [100]

$$\mathrm{FE} = m \times n \times F / (I \times t) \tag{14}$$

2.2.5 Electrochemically active surface area (ECSA)

ECSA can be used to express the effective contact area between the active site of catalyst and electrolyte. ECSA is usually measured by double-layer capacitance (C_{dl}) and is positively correlated with it [101]. Generally, the higher the C_{dl} value is, the more exposed surface active site are, and the better the activity of the catalyst is. [102, 103]. Du et al. prepared CoFe-MS/MOF nanosheet electrocatalyst by simple solvothermal synthesis [104]. The ultrathin nanosheets formed by the embedding of metal sulfide nanoparticles significantly increased the ECSA, making the system have high conductivity and high activity, thus effectively regulating the electronic state and promoting the electrochemical reaction. It can also be obtained from the Coulomb integral under the cyclic voltammetry (CV) curve outside the Faraday region, which is usually a 100 mV window centered on the open circuit potential (OCP) [105]. Compared with traditional electrodes, self-supporting electrodes (such as foam nickel (NF) electrodes) will expose rich active centers due to their own porous channels and large surface area after loading nano catalysts, resulting in the improvement of electrochemical performance. Li et al. prepared Co_3S_4/NiS@NF on NF by two-step synthesis route of hydrothermal and sulfurization, which showed an η_{10} of only 119 mV [106]. To find the reason of improved OER performance, the ECSA was calculated, showing that the ECSA is the key factor for the high OER performance, significantly increasing the number of heterogeneous active sites of the catalyst.

2.2.6 Stability

The long-term stability is the standard to evaluate whether the electrocatalyst can be used in commercial applications. Continuous CV is usually used to evaluate the stability. Another method often used is to measure the change of voltage (or current density) after several hours under constant current (or constant voltage), that is, chronopotentiometry or chronoamperometry. Universally, smaller change in the chronopotentiometric/chronoamperometric curve means that the OER stability of catalyst is better.

3 Synthesis method of self-supported chalcogenides

To date, various preparation techniques have been developed to synthesize electrocatalysts with specific structures and morphology. This paper describes six types of synthesis strategies: hydrothermal/solvothermal thermal reaction, chemical vapor deposition (CVD), electrodeposition, vacuum filtration, freeze-drying, and template synthesis, depending on the selective substrate and the target catalyst components.

3.1 Hydrothermal/solvothermal synthesis

Hydrothermal/solvothermal method is to heat the autoclave with aqueous solution or organic solvent as the solution in a special closed reaction vessel to make the chemical reaction in a high temperature and high pressure environment. The hydrothermal/solvothermal method is simple and low-cost [107, 108], which is an eco-friendly technology. Under the condition of high temperature and high pressure, it is easy to obtain an appropriate grain size, avoiding the possible grain defects and the introduction of impurities in the preparation process [109, 110]. This method is mostly used for large area or flexible substrates, which is of great significance for practical application. For example, Hu et al. successfully prepared catalysts with three dimensional (3D) porous structure on NF (Ni_3Se_2@NiFe-LDH/NF) by two-step hydrothermal method (Fig. 2(a)) [111]. NiFe-LDH nanosheets and Ni_3Se_2 nanowires formed *in situ* on NF are interlaced to form a porous core–shell structure, which provides a large surface area and accelerates electron transport efficiency. The η_{10} for HER and OER in 1 M KOH is 68 and 222 mV, respectively. Shang et al. developed a solvothermal strategy to *in situ* grow Ni_xS_y on NF (Ni_xS_y/NF) [112]. The crystalline phase structure of Ni_xS_y can be adjusted by changing the vulcanization quality. Scanning electron microscopy (SEM) image showed that Ni_xS_y had a unique aggregation sheet and interconnected porous structure. Luo et al. prepared vertically aligned Mn_3O_4/Fe_2O_3 heterojunction nanosheets on NF via changing the metal ratio [31]. By changing different molar ratios of Fe and Mn (Fe/Mn = 0.2/1, 0.4/1, 0.6/1, 0.8/1, and 1/1), the morphology of MnFeO-NF-*x* thin films was adjusted, showing different catalytic activities. MnFeO-NF-0.4 and MnFeO-NF-0.8 showed a clear microstructure and excellent OER performance.

3.2 CVD synthesis

CVD synthesis is usually carried out under atmospheric pressure or low vacuum, and gas–solid growth method is one of the most common chemical vapor synthesis methods. CVD can be used to obtain thin film coatings with high purity, good compactness, and good crystallization [113]. Simple equipment and convenient operation are needed. Generally, argon or hydrogen gas is introduced as the gas phase, and sulfur powder, selenium powder, or other powder raw materials can also be used as the gas phase [114]. CVD is widely used in the preparation of self-supporting electrodes. Zhou et al. synthesized selenided nanosheet array on CC ($CoSe_2$@ vertically-oriented graphene (VG)/CC) without any adhesive via an *in situ* CVD synthesis (Fig. 2(b)) [115]. The three dimensional porous VG framework not only provided an electron transmission channel, but also addressed the problems of volume expansion and particle aggregation. Ma et al. synthesized graphene encapsulated in S,N-codoped nanosheets on NF (3DSNG/NF) via an *in situ* CVD synthesis [116]. The OER properties of 3DSNG/NF with different S and N doping concentrations were further investigated. When the doping content of N and S is 2.56 at.% and 2.95 at.%, respectively, the catalyst showed good catalytic activity. Ali et al. synthesized multi-walled carbon nanotubes (MWCNTs)-graphene hybrid nanomaterials on Ni-silica nanocomposites by a simple CVD method [117]. The effects of the combination of Co, Fe, and Ni with silicon matrix on the structure of mixed carbon nanomaterials were studied, showing that MWCNTs graphene carbon nano material structure grown by Ni had better OER performance than the other two metals.

3.3 Electrochemical deposition

Electrochemical deposition synthesis (EDS) is a technology of coating on electrode by electrochemical reaction under the action of external electric field. It has the advantages of simple operation, low synthesis temperature, low cost, and high synthesis efficiency. Electrodeposition is usually used to fabricate self-supporting nano films on conductive substrates, which has been widely used [118–120]. Shang et al. synthesized Fe hydroxides film encapsulated in V-doped nickel sulfide nanowire on NF (uFe/NiVS/NF) composites via a controllable electrodeposition (Fig. 2(c)) [121]. They found that the best OER catalytic performance can be obtained at the electrodeposition time of 15 s. Xu et al. prepared CoPO@C on NF by simple electrodeposition [122]. The effects of different morphologies (cube, octahedron, sphere, and nanoflower) synthesized at different potentials on the OER performance were further studied, exhibiting that the catalyst with sphere morphology showed the best OER catalytic activity among all samples. Li et al. prepared NiFe LDH@Ni NTAs/NF 3D-layered nano array on NF via a facile electrochemical dealloying

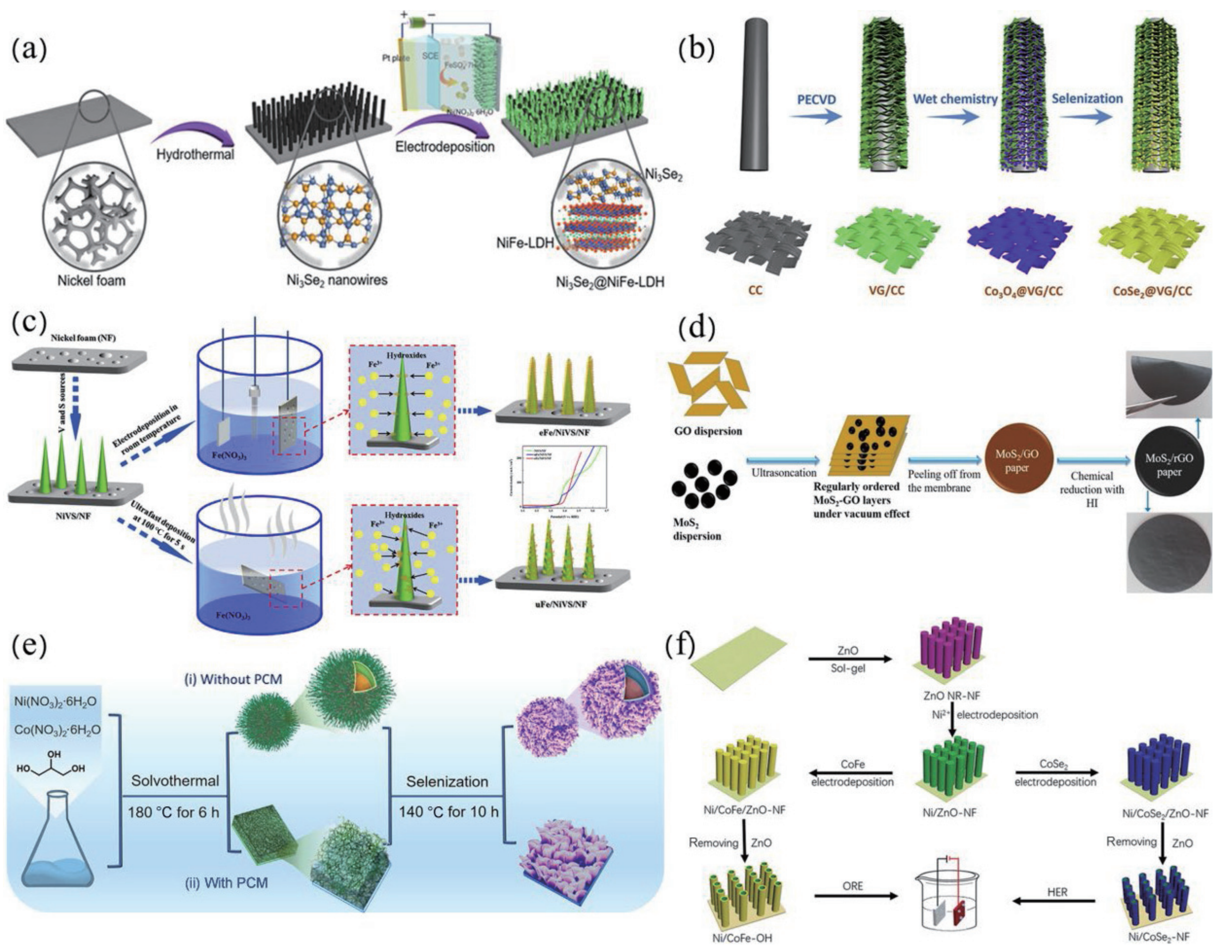

Figure 2 (a) Schematic fabrication process of Ni_3Se_2@NiFe -LDH/NF. Reproduced with permission from Ref. [111], © The Royal Society of Chemistry 2020. (b) Synthetic illustration of $CoSe_2$@VG/CC. Reproduced with permission from Ref. [115], © Elsevier Ltd. 2019. (c) Synthetic illustration of uFe/NiVS/NF. Reproduced with permission from Ref. [121], © Elsevier B.V. 2017. (d) Synthetic illustration of PtNLs-MoS_2/rGO. Reproduced with permission from Ref. [126], © Wiley-VCH Verlag GmbH & Co. KGaA, Weinheim 2018. (e) Synthetic illustration of $NiCoSe_2$@PCM. Reproduced with permission from Ref. [131], © Elsevier B.V. 2021. (f) Synthetic illustration of Ni/CoFe-OH and Ni/$CoSe_2$-NF. Reproduced with permission from Ref. [139], © The Royal Society of Chemistry 2020.

method coupled with the electrodeposition method [35]. Due to the hollow tube core layer structure, the internal and external electrons are highly dispersed, and a large number of active sites are exposed, which makes the catalyst show a low η_{10} of 191 mV for the OER.

3.4 Vacuum filtration

The separation of liquid and solid can be realized through a porous substrate by forcing vacuum on the opposite side of the filter using vacuum filtration method. The film thickness can be controlled by changing the concentration [123, 124]. Although the operation is simple, it consumes a good deal of solvent and time, and therefore, it has not been commonly used. Kong et al. prepared graphene oxide self-supported SnSe thin film electrode（ SnSe-TP@rGO） using a two-step synthesis technology of vacuum filtration and low-temperature annealing [125]. The unique three dimensional layered frame structure ensures the good stability of the system and accelerates the electron transfer efficiency. Kader et al. prepared an independently supported PtNLs-MoS_2/rGO graphene oxide paper catalyst by simple vacuum filtration and electrodeposition (Fig. 2(d)) [126].

3.5 Freeze drying

Freeze drying technology is a technology where the water in the mixture is first condensed into ice through cooling, and then the ice sublimates under vacuum conditions, so as to make the particles uniformly dispersed and obtain small particles [127, 128]. Freeze drying assisted method can be used to fully disperse one sample into another sample, and the combination of the two can provide better electrochemical performance [129]. For example, Shudo et al. carried out the freezing technology of $Ni(OH)_2$ to obtain a carbon free 3D structure Ni/NiO_x heterojunction material [130]. The 3D mass material formed by layer by layer stacking of two dimensional (2D) thin sheets by freeze-drying showed excellent electrochemical properties. Poorahong et al. synthesized $NiCoSe_2$@phase change material (PCM) by three kinds of synthesis techniques (Fig. 2(e)) [131]. Macroporous carbon conducting membrane (PCM) as a catalyst growth framework was synthesized by low temperature treatment, freeze drying, and carbonization. $NiCoSe_2$ nanosheets were vertically staggered on the PCM. Hu et al. synthesized N,P-codoped porous carbon aerogel (Ni_3S_4/N,P-HPC) by freeze-drying assisted sol gel method [132]. The cellular porous N,P-HPC surface is rich in metal binding sites. The freeze-drying process improves the agglomeration in the hydrogel preparation, making Ni_3S_4 nanoparticles firmly embedded on it. The synergistic effect between Ni_3S_4 nanoparticles and porous carbon aerogel promoted the OER activity.

3.6 Template synthesis

Template assisted preparation strategy can be divided into hard template method and soft template method [133–136]. ZnO and SiO_2 are typically used as hard templates, while polymer PEO_{106}–PPO_{70}–PEO_{106} (F127) and EO_{20}–PO_{70}–EO_{20} (P123) are typically soft templates [137, 138]. As presented in Fig. 2(f), using ZnO as self-template, Feng et al. synthesized hollow nanotube arrays on NF (Ni/CoFe–OH and Ni/$CoSe_2$–NF) by two-step CVD method [139]. Due to the special morphology of smooth hollow tube arrays, the obtained catalysts show fast reaction kinetics and good OER performance. Han et al. fabricated nitrogen-doped carbon nanocomposite electrocatalyst ($Co_{0.85}$Se-NC/C) using F127 as the soft template [140]. Furthermore, Yan et al. synthesized ternary NiFeMoS/NF-P nanorod arrays on NF via electrodeposition combined with hydrothermal methods [141]. The surface of the nanorods has a layer by layer scaly morphology due to the addition of the soft template P123 and MoO_4^{2-} morphology guiding reagent, and the whole nanorods are similar to anemones.

4 Self-supported transition metal chalcogenides for the OER

So far, various strategies have been reported to use nickel foam, carbon cloth, carbon fiber paper, metal mesh, etc., as substrates to prepare self-supporting electrocatalytic materials (Table 1). Self-supporting electrodes include metal and non-metal fluid collectors. Metal collector (such as copper foil, titanium mesh, and Ni foam) has high conductivity, but it has the disadvantages of high price and poor corrosion resistance. Since the conductivity of transition metal chalcogenides is very poor, the metal collector can be selected as a self-supporting electrode to improve the conductivity. Non-metallic fluid collection mainly includes carbon-based substrates, e.g., graphite plate, carbon fiber paper, and carbon cloth. Carbon substrate is widely used in electrode construction due to its low price, good flexibility, and simple preparation process. However, carbon-based supports are easily corroded by oxidation in an oxidizing oxygen evolution environment. To obtain excellent catalytic activity and stability of the electrocatalyst, it is particularly important to select a suitable substrate. The electrocatalytic activity is closely related to the structure and morphology of the electrocatalyst. Different synthesis methods would lead to different nanostructure and morphology. The study of electrode materials with self-supported structure has great potential to improve the performance of OER.

4.1 NF supported chalcogenides

Foam nickel (NF) is a kind of functional material with three dimensional porous, interconnected pores, and metal skeleton. This kind of material has a large electrochemical reaction surface interface, and has a great application prospect in electrochemical OER electrode [142, 143]. Among all the transition metal sulfide catalysts reported so far, nickel sulfide is the most studied transition metal sulfide. For instance, Chen et al. prepared Fe doped Ni_3S_2 nanosheets on NF by a simple hydrothermal synthesis method [144]. Due to the addition of Fe, the obtained catalyst showed an excellent OER catalytic activity with a small η_{20} of 246 mV and Tafel slope of 66 mV·dec^{-1} in 1.0 M KOH. DFT calculations showed that the OER performance is fundamentally enhanced by Fe doping. The incorporation of Fe alters the OER pathway and reduces the binding O^* energy barrier, and the ΔG_{O*} at the Fe active site is the lowest. Pan et al. prepared Ni_3S_2-FeS/NF-2 through one-step hydrothermal synthesis process, which has a unique 3D porous array structure and is conducive to increasing the exposure of electrocatalytic active sites, thus improving the electron transfer capacity and enhancing the release of gas. The Ni_3S_2-FeS/NF-2 electrode required an η_{100} of 253 mV in 1.0 M KOH [145]. Tang et al. prepared Cu_2S/Ni_3S_2-0.5@NF via two-step hydrothermal method (Fig. 3(a)) [146]. The interface regulation of Cu_2S/Ni_3S_2 sheets supported on NF was achieved with different molar ratios between Ni and Cu (Ni/Cu = 0.25/1, 0.5/1, and 1/1). SEM images indicated that Cu_2S/Ni_3S_2-0.5@NF with Ni/Cu of 0.5/1 demonstrated porous nanosheet structure, which afforded current densities of 100 and 500 mA·cm^{-2} at overpotentials of only 237 and 280 mV, respectively, and a low Tafel slope of 44 mV·dec^{-1} (Figs. 3(e) and 3(f)).

Ren et al. synthesized a bifunctional electrocatalyst on NF ($Co_{0.9}Fe_{0.1}$-Se/NF) by a simple one-step electrodeposition method [147], showing a small η_{10} of 246 mV in 1.0 M KOH. Zhao et al. used hydrothermal method and subsequent electrodeposition technology to design NiSe@Ni_3Se_2 nanowire arrays grown directly on NF (NiSe@Ni_3Se_2/NF) [148]. From the SEM images, the NiSe cluster arrays on the NF surface cross each other, forming a 3D network structure (Figs. 3(b)–3(d)). The porous structure and

Table 1 Brief summary of self-supported transition metal chalcogenides toward OER performance

Electrocatalysts	Substrate	Electrolyte	η_{10}(mV)	Tafel slope (mV·dec^{-1})	Ref.
Ni_3Se_2@NiFe-LDH/NF	NF	1 M KOH	222	61.3	[111]
$(Ni_{0.77}Fe_{0.23})Se_2$/CC	CC	1 M KOH	228	69	[162]
Ni_3S_2@Ni/CC	CC	1 M KOH	290.9	101.26	[158]
NiFe/Co_9S_8/CC	CC	1 M KOH	219	55	[160]
FeCoNiS_x/NF	NF	1 M KOH	231	55	[142]
Mn-$Co_{0.85}$Se/$NiSe_2$/NF	NF	1 M KOH	175	33.26	[149]
$Co_{0.9}Fe_{0.1}$-Se/NF	NF	1 M KOH	246	—	[147]
NiSe@Ni_3Se_2/NF	NF	1 M KOH	281	67.3	[148]
Co-O@Co-Se/Cu	Copper foil	1 M KOH	340	57.5	[184]
NiCoFe-S/Ti	Ti mesh	1 M KOH	230	65	[181]
$NiSe_2$@MoS_2	CFP	1 M KOH	267	85	[175]
$Cu_2S/TiO_2/Cu_2S$	TiO_2 backbone	1 M KOH	284	72	[195]
Ni_3S_2-NiO_x/NF	NF	1 M KOH	241	59	[196]
MgO/NCS-CC	CC	1 M KOH	145	114.7	[197]
P-Ni_3S_2/NF	NF	1 M KOH	256	30	[198]
Fe-$CoSe_2$/ NF	NF	1 M KOH	220	35.6	[199]
Mn-$NiCo_2S_4$/NF	NF	1 M KOH	220	29	[200]
$CoSe_2$@Se/CC	CC	1 M KOH	250	50.2	[164]

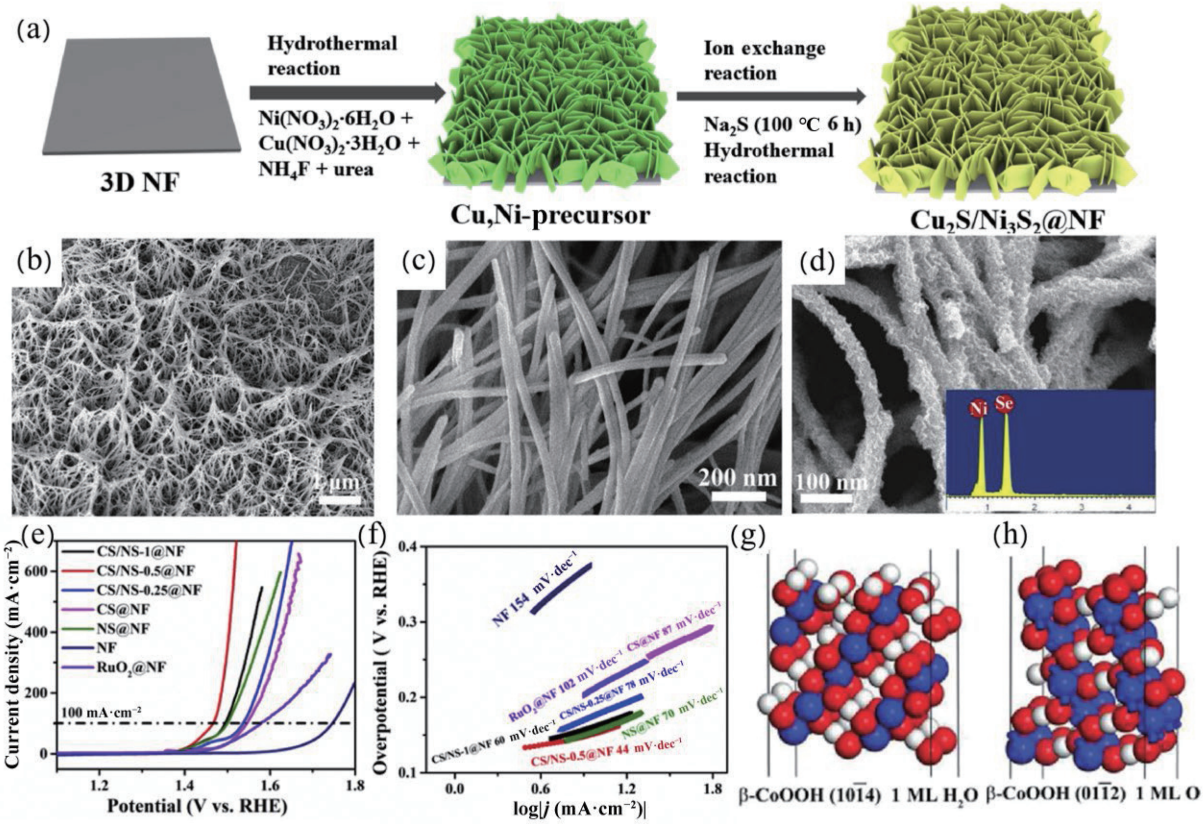

Figure 3 (a) Synthetic process of Cu_2S/Ni_3S_2-0.5@NF. Reproduced with permission from Ref. [146], © Hydrogen Energy Publications LLC 2021. (b)–(d) SEM images of $NiSe@Ni_3Se_2$/NF. Reproduced with permission from Ref. [148], © Elsevier Inc. 2020. (e) LSV curves of CS/NS-1@NF, CS/NS-0.5@NF, CS/NS-0.25@NF, NS@NF, NF, and RuO_2@NF. (f) Corresponding Tafel plots. Reproduced with permission from Ref. [146], © Hydrogen Energy Publications LLC 2021. (g) and (h) Side views of the surface terminations of β-CoOOH (1014) and β-CoOOH (0112) surface. The white, red, and blue spheres represent H, O, and Co atoms, respectively. Reproduced with permission from Ref. [151], © WILEY-VCH Verlag GmbH & Co. KGaA, Weinheim 2019.

large surface area accelerate the OER kinetics. $NiSe@Ni_3Se_2$/NF showed good OER catalytic activity with a small η_{10} of 281 mV. Zhou et al. synthesized interwoven 3D Mn-$Co_{0.85}Se/NiSe_2$ nanosheets on NF by two-step electrodeposition and vapor deposition [149]. The Mn-$Co_{0.85}Se/NiSe_2$/NF nanoarrays exhibited a superior OER catalytic activity with a small η_{10} of 174 mV in 1.0 M KOH owing to their large specific surface area and uniform pore structure. Qian et al. obtained $CoNiTe_2$/NF bimetallic nanosheets by hydrothermal method [150]. The unique thin and defective 3D morphology of $CoNiTe_2$/NF provided rich electrocatalytic active sites and fast charge transfer. Due to the strong covalent advantage of Te element, the optimized $CoNiTe_2$/NF displayed high durability and an outstanding OER catalytic performance with overpotentials of 181, 230, and 270 mV at 100, 500, and 1000 $mA \cdot cm^{-2}$, respectively.

Liu et al. used one-step hydrothermal method to fabricate vertically aligned CoTe and NiTe nano arrays on NF [151], and found that CoTe nanoarrays on NF exhibited superior OER catalytic activity with a small η_{100} of 350 mV. DFT calculations showed that the high OER activity of CoTe electrocatalyst is ascribed to the generation of CoOOH on the surface during the reaction (Figs. 3(g) and 3(h)). The d orbital of the Co site moved down due to the bonding orbital, which strengthened the adsorption of the intermediate and decreased the adsorption free energy. Sadaqat et al. prepared $Ni_{0.4}Fe_{0.6}Te_2$ nanosheet arrays on NF by hydrothermal synthesis strategy [152]. The synergistic effect of Ni and Fe metal atoms can not only improve the conductivity, but also cause lattice distortion of NiTe, thus optimizing the adsorption energy of hydroxide intermediates, and enhancing the OER activity.

4.2 CC supported chalcogenides

CC has good mechanical flexibility and thermal stability [153]. It can be easily cut into various sizes and shapes [154–157]. It shows good electrochemical performance and becomes a common self-supporting electrode material. Qian et al. synthesized Ni_3S_2@Ni/CC via electroplate followed by a sulfuration process [158]. The Ni_3S_2@Ni/CC with abundant active sites exhibited a good OER performance with η_{10} of 290.9 mV as well as a low Tafel slope (101.26 $mV \cdot dec^{-1}$) and good stability for 30 h in 1.0 M KOH. Jiang and co-workers fabricated metal and heteroatom co-doped nanoplates with fiber carbon nanostructures on CC (Fe_3O_4/NiS@CC) via two step carbonization process [159]. Fe_3O_4/NiS nanoplates on CC exhibited a superior OER catalytic activity with a small η_{10} of 310 mV in 1.0 M KOH due to their large specific surface area (1796 $m^2 \cdot g^{-1}$) and high conductivity. Through chemical bath deposition and hydrothermal treatment, Zhan et al. prepared three metal nanoarrays with vertically layered nanostructures on CC (NiFe/Co_9S_8/CC) (Fig. 4(a)) [160]. The Co_9S_8 nanotubes with hollow structure vertically grown on CC are covered with a layer of NiFe nanosheets (Figs. 4(b) and 4(c)) and there are two synergistic effects among Co_9S_8 nanotubes and the substrate and NiFe nanosheets. The unique hierarchical structure of NiFe/Co_9S_8/CC can not only increase the numbers of active sites, but also improve electron transfer efficiency, thus boosting the OER intrinsic catalytic activity. Besides, there are two synergistic effects between NiFe/Co_9S_8 and Co_9S_8/CC, resulting in fast electron transfer rate and high intermediate absorption/desorption capacity. The optimized NiFe/Co_9S_8/CC exhibited a superior catalytic activity and required an η_{10} of 219 mV in 1.0 M KOH. Li et al. fabricated P-CoS_2 HNA/CC via a vulcanization reaction coupled with a phosphorization strategy [161]. P-CoS_2

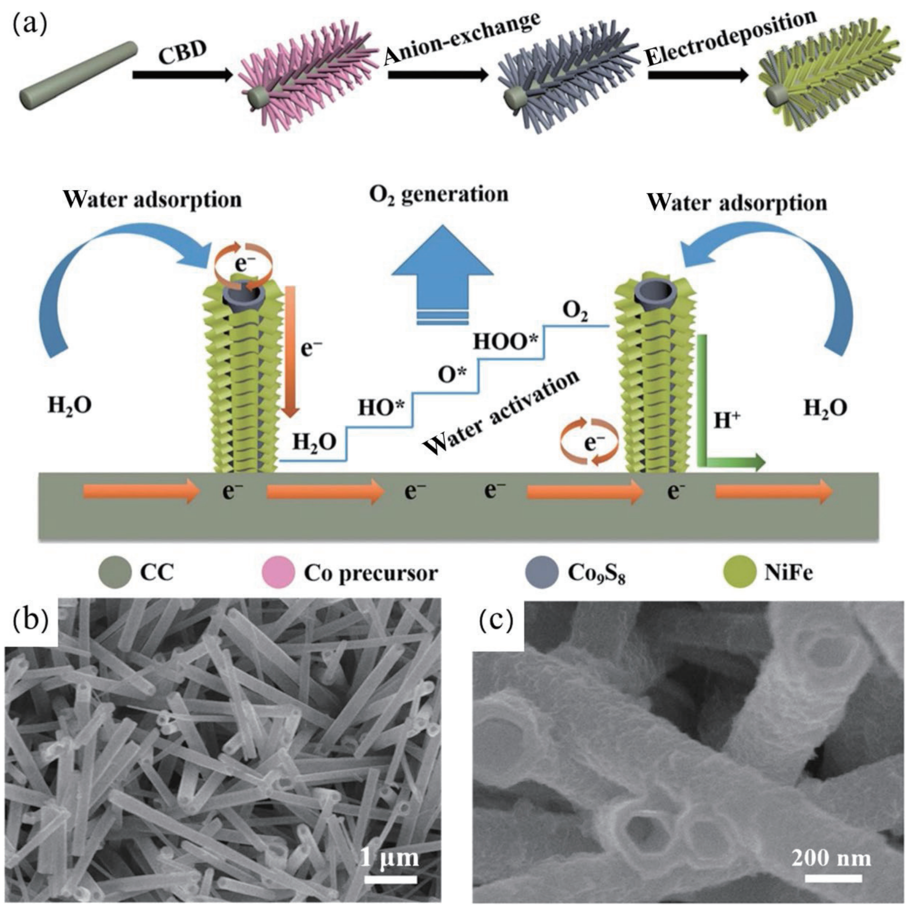

Figure 4 (a) Synthetic process of NiFe/Co_9S_8/CC. (b) and (c) SEM images of NiFe/Co_9S_8/CC. Reproduced with permission from Ref. [160], © The Royal Society of Chemistry 2019.

HNA/CC possessed a unique hollow nanostructure, which can be in favor of promoting the exposure of active sites, enhancing electron transfer, and accelerating gas generation. The P-CoS_2 HNA/CC electrode required an η_{10} of 250 mV in 1.0 M KOH.

Yan et al. synthesized $(Ni_{0.77}Fe_{0.23})Se_2$/CC with 3D layered structure on CC by selenidation process [162]. After selenidation of NiFeLDH/CC hydroxide nanosheets, a large number of nanopores were added on the surface. The introduction of porous structure increased the electron transfer and improved the conductivity of the system. The $(Ni_{0.77}Fe_{0.23})Se_2$/CC electrode showed a small η_{10} of 228 mV, and maintained the stability for 40 h. Ghoshvia et al. prepared hexagonal nanosheets on CC ($NiSe_2$/CC) by electrodeposition process [163]. The electrocatalyst composed of hexagonal flakes has many hydrophilic active sites, which increases the electron transfer efficiency. The $NiSe_2$/CC electrode required an η_{10} of 210 mV in 1.0 M KOH for the OER. Selenium-coated cobalt selenide ($CoSe_2$@Se) nanoflake catalyst on CC (Fe_2O_3-$CoSe_2$@Se/CC) was prepared via a hydrothermal synthesis and immersion method (Fig. 5(a)) [164]. The unique three dimensional coral originating from Fe_2O_3-$CoSe_2$@Se/CC provided more abundant electrocatalytic active sites and fluent electrolyte diffusion. The optimized Fe_2O_3-$CoSe_2$@Se/CC-1.0h displayed an outstanding OER catalytic performance with η_{10} of 252 mV (Figs. 5(b) and 5(c)). Liu et al. prepared vertically grown nanostructures on CC (Cu–Ni–Se@CC) by hydrothermal method [165], which showed an η_{10} of 270 mV.

Yang et al. synthesized S doped CoTe nanoarrays on carbon cloth (S-CoTe/CC) via a hydrothermal approach [166]. The incorporation of S into CoTe nanosheets favored the chemical structure transformation from CoTe@CoOOH to S-CoTe@CoOOH during the OER, which serves as the real active sites. DFT calculations demonstrated that S-CoTe@CoOOH required a lower Gibbs adsorption energy of the OER intermediate (O*) compared to pristine CoTe@CoOOH and CoOOH (Fig. 5(d)), which might account for the ameliorated OER catalytic activity. After the incorporation of S element, the energy barrier is reduced (Figs. 5(e) and 5(f)), the electronic structure is adjusted, the conductivity is enhanced, and the reaction kinetics is promoted. The optimal S-CoTe/CC showed an excellent OER performance with a small η_{10} of 257 mV. Xu et al. synthesized Ni_3Te_2-CoTe/CC composite electrocatalyst by simple hydrothermal method [167]. DFT calculations showed that the Ni_3Te_2 component has a d-band center close to the Fermi level, and the electron density is enhanced, which means that the interaction weakens the adsorption strength of the intermediate, thus showing the internal enhancement of OER performance. Moreover, the introduction of CoTe phase into the composite increases the effective specific surface area, and thus improves the electrocatalytic activity.

4.3 CFP supported chalcogenides

CFP has a macroporous network structure, good chemical inertia and mechanical strength, and high conductivity, which can be used as 3D support for self-supporting electrocatalysts on a large scale to improve electrocatalytic performance [168–170]. Guo et al. prepared turf-like NiS nanowires on flexible CFP by two simple methods: hydrothermal method and calcination method [171]. NiS was directly and uniformly grown on the conductive CFP substrate, which not only has large specific surface area, but also has small charge transfer resistance and high conductivity, thus enhancing the electrocatalytic activity. The NiS/CFP catalyst showed excellent electrocatalytic HER and OER performance. For total water splitting, only 1.59 V was required at 10 mA·cm^{-2}. Li et al. used a two-step hydrothermal method to prepare *in-situ* 3D

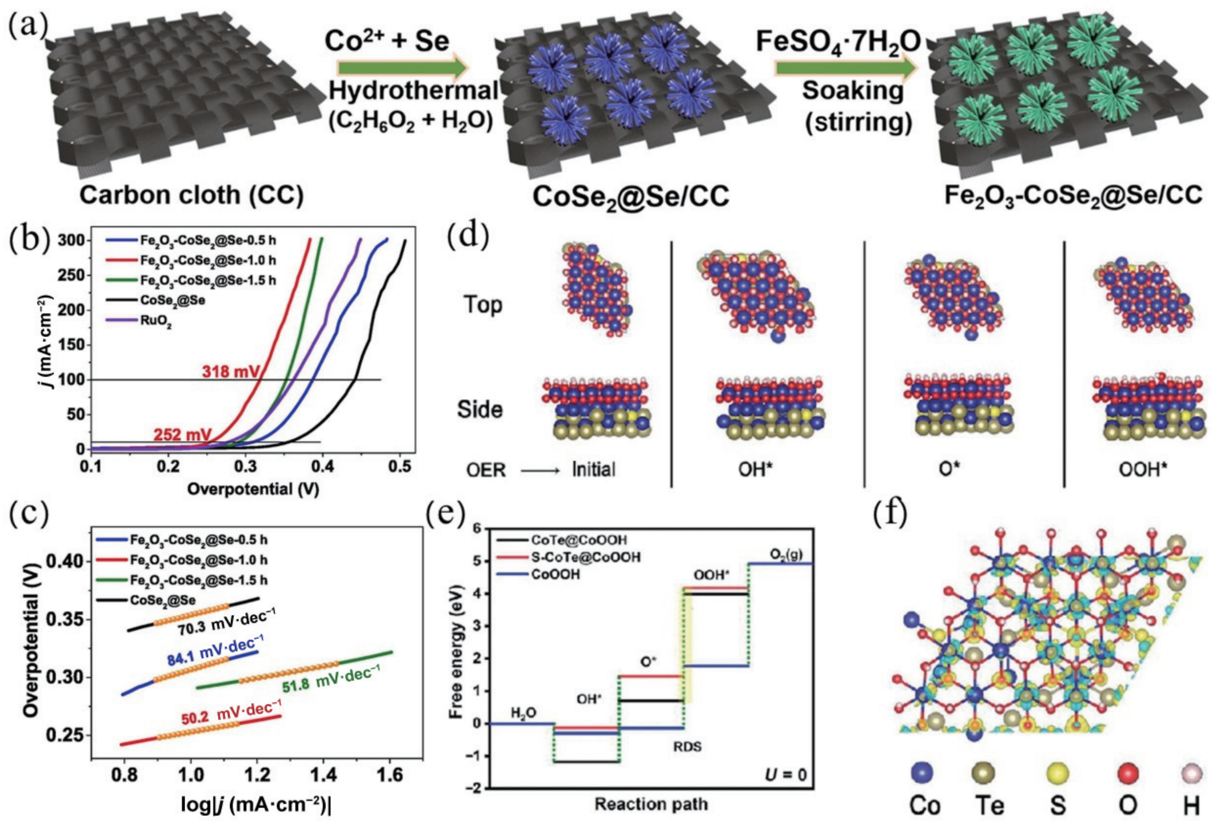

Figure 5 (a) Synthetic process of Fe_2O_3-CoSe@Se/CC. (b) LSV curves of Fe_2O_3-$CoSe_2$@Se/CC-0.5h, Fe_2O_3-$CoSe_2$@Se/CC-1.0h, Fe_2O_3-$CoSe_2$@Se/CC-1.5h, and $CoSe_2$@Se. (c) Tafel plots. Reproduced with permission from Ref. [164], © Elsevier B.V. 2021. (d) Different intermediate configurations generated during OER. (e) Calculated free energy diagram. (f) The deformation charge density of S-CoTe@CoOOH. Reproduced with permission from Ref. [166], © Wiley-VCH GmbH 2021.

interconnected Fe doped NiS nanosheets on CFP (Fe–NiS@CFP) for the OER (Fig. 6(a)) [172]. The effects of Fe doping on the microstructure and electronic regulation were studied. The morphology of 3D interwoven nanosheets remained after Fe doping (Figs. 6(b) and 6(c)), but the length and thickness of the nanosheets decreased, while the specific surface area increased, meaning that the addition of Fe introduced defects and holes, and adjusted the electronic state, which was more conducive to the adsorption and desorption process of O_2. The optimal Fe–NiS@CFP showed an η_{100} of 275 mV and maintained stability for 50 h in 1.0 M KOH (Figs. 6(d) and 6(e)). Huang et al. synthesized an electrocatalyst composed of Co_9S_8 and porous carbon on CFP [173]. The Co_9S_8 nanoparticles treated by dicyandiamide decomposition showed better catalytic performance (η_{10} = 280 mV) than the untreated nanoparticles due to synergistic effect with N-doped carbon matrix. Liu et al. prepared Co_{2-x}SP/CFP nanosheets by two-step electrodeposition [174]. The first step is to deposit cobalt sulfide nanosheets onto CFP, which improves the inherent stability. The second step is to deposit non-metallic P onto cobalt sulfide nanosheets, which is uniformly doped on the surface of cobalt sulfide. By adjusting the number of P deposition cycles, different P-doping species can be obtained, so as to achieve different valence states of Co (Co^{2+} and Co^{3+}). The substitution of P increased the content of Co^{3+} and changed the surface morphology of the catalyst. The large pore size was more conducive to electron transport. The optimal Co_{2-x}SP/CFP exhibited OER activity with an η_{10} of 279 mV, a low Tafel slope of 54 mV·dec^{-1}, and excellent long-term stability of 60 h.

Huang at al. synthesized heterostructure electrocatalyst CFP@$NiSe_2$@MoS_2 by simple electrodeposition method combined with hydrothermal method [175]. Due to the synergistic effect between $NiSe_2$ and MoS_2, the corresponding X-ray diffraction (XRD) peak showed an obvious blue shift, which was helpful to improve the catalytic activity of OER. Ni doping into MoS_2 formed defect heterostructure, increased the active sites on the surface of MoS_2, and reduced the energy barrier of OER (η_{10} = 267 mV). Sancho et al. constructed $NiCo_2S_4$ NW/CFP nanowires by hydrothermal method and selenidation process [176]. The nanowires increased the electrochemical active surface area, while the porous configuration improved the electrolyte penetration, and the CFP substrate avoided the aggregation of nanoparticles. DFT calculations showed that the density of states (DOS) of $NiCo_2S_4$ is significantly higher than that of oxidized $NiCo_2O_4$ (Figs. 6(f)–6(h)), which improved the conductivity and carrier concentration, thus enhancing the catalytic OER performance.

4.4 Metal mesh/plate supported chalcogenides

Metal mesh/plate has excellent conductivity and flexibility [177, 178]. It can be used as a metal source to grow catalysts on the surface [179, 180]. Li et al. constructed NiCoFeS nanosheets with three-metal layered structure in the form of hydrangea on Ti mesh（NiCoFeS/Ti）via hydrothermal combined vulcanization process (Fig. 7(a)) [181]. SEM images showed that NiCoFe-LDH was uniformly grown on the surface of Ti mesh (Figs. 7(b) and 7(c)), which presents the shape of large hydrangea and intersects with each other. The hydrangea shape was not changed after vulcanization, but the surface changed from smooth to rough (Fig. 7(d)). For the OER, it showed a low η_{10} of 230 mV (Fig. 7(e)). Zhang et al. prepared Ti@$Co_{0.85}$Se electrocatalyst by one-step hydrothermal method [182]. The ohmic contact between the Ti mesh with good conductivity and the $Co_{0.85}$Se interface greatly reduced the electron transfer resistance (Fig. 7(f)), and the electrons can easily flow back to the metal (Fig. 7(g)). The optimal Ti@$Co_{0.85}$Se exhibited OER activity with an overpotential of 570 mV at 29.6 mA·cm^{-2} and long-term stability of 30 h. Chen et

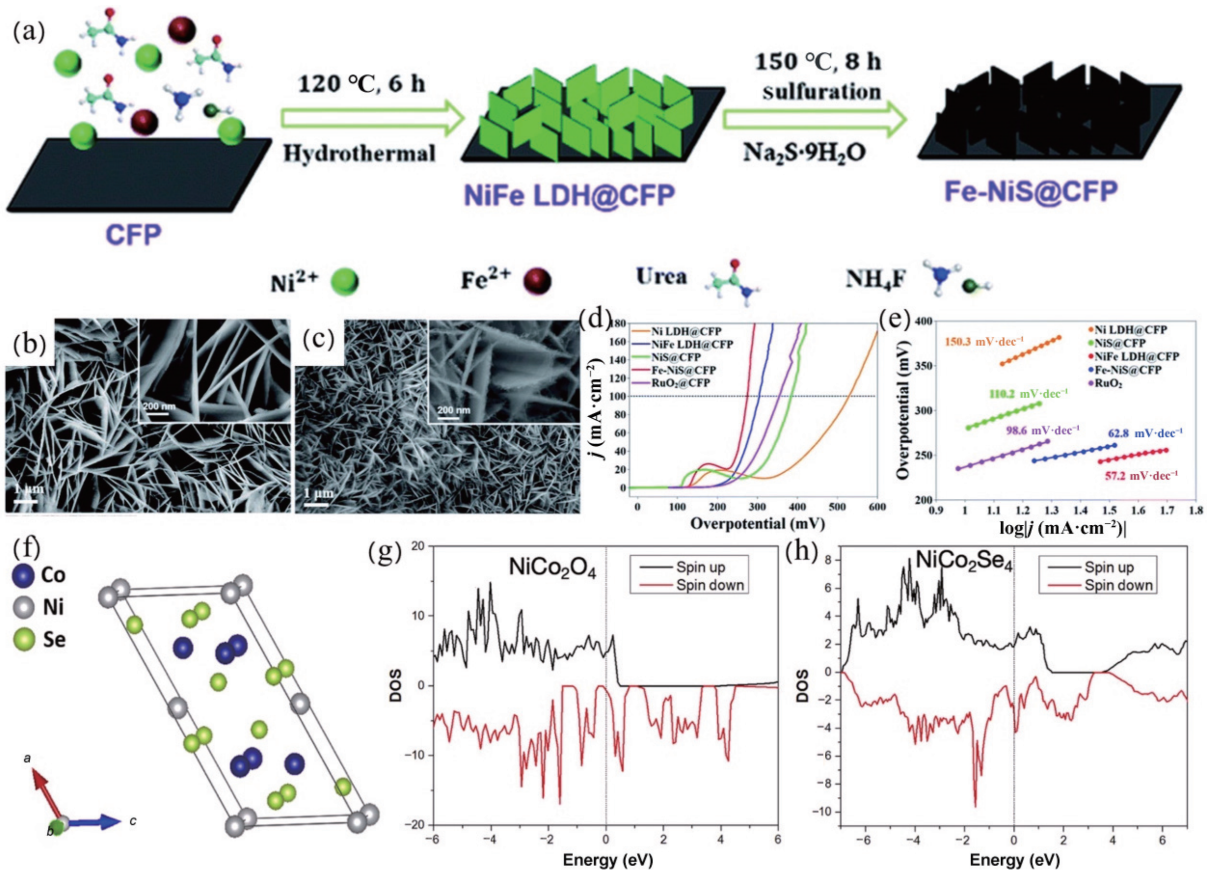

Figure 6 (a) Synthetic process of Fe–NiS@CFP. (b) and (c) SEM images of Ni LDH@CFP and NiFe LDH@CFP. (d) LSV curves of Ni LDH@CFP, NiFe LDH@CFP, NiS LDH@CFP, Fe-NiS LDH@CFP, and RuO_2@CFP. (e) Tafel plots. Reproduced with permission from Ref. [172], © The Royal Society of Chemistry 2022. (f) Crystal structure of $NiCo_2Se_4$. (g) Calculated density of states for $NiCo_2O_4$. (h) Calculated density of states for $NiCo_2Se_4$. Reproduced with permission from Ref. [176], © Sancho, H. et al. 2020

al. prepared Cu_2Se and Cu_2O hybrid needle like nanoparticles (Cu_2Se-Cu_2O/TF) via simple electrodeposition at the cathode [183]. Cu_2Se-Cu_2O was formed on the surface of copper oxide protective layer, which can catalyze the OER with η_{10} of 465 mV. Yang et al. prepared three dimensional hybrid thin film electrode on copper foil (Co-O@Co-Se/Cu) by electrodeposition [184]. When Se was incorporated, the structure and crystal phase transition occurred. Because copper foil was used as the substrate, the electron transfer resistance was reduced and the gas release was enhanced. The Co-Se species in the film was gradually transformed into Co-O species. Zuo et al. constructed Cu_2S/CM nanowires on copper foil by anion exchange method [185]. Copper oxide obtained by *in-situ* oxidation of cuprous sulfide showed excellent electrochemical OER performance. The electrode with high surface area and fast electron transfer rate showed an η_{10} of 286 mV. Yuan et al. used a simple hydrothermal method to directly grow Fe-Ni_3S_2/FeNi nanosheet arrays on FeNi alloy foils [186]. The adsorption free energy of Fe doped Ni_3S_2 was lower than that of Ni_3S_2 in the OER (Figs. 7(h) and 7(i)). In addition, the electronic structure of Ni_3S_2 is disordered due to the addition of Fe, which significantly increases the DOS. Fe-Ni_3S_2 showed more metallic states near the Fermi level than Ni_3S_2, resulting in accelerated electron transfer efficiency and excellent OER catalytic performance. The optimal Fe-Ni_3S_2/FeNi nanosheets exhibited remarkable OER activity with an η_{10} of 282 mV and a small Tafel slope of 54 mV·dec^{-1}.

4.5 Other substrates supported chalcogenides

Other substrates (such as stainless steel, fluorine-doped tin oxide (FTO) coated glass substrates, etc.) are also widely used in commerce [187–189]. Deng et al. synthesized adhesive-free self-supporting Co_9S_8@Co_3O_4 core/shell array electrocatalyst by simple hydrothermal method and vulcanization process [190]. Co_9S_8 nanosheets were grown on Co_3O_4 nanowire cores to form a unique core/shell array, which greatly increased the active surface area and stability, which exhibited an η_{20} of 260 mV and a small Tafel slope of 56 mV·dec^{-1}. Mondal et al. prepared CdSe thin film electrodes and CdSe modified by Pd quantum dots on FTO coated glass substrates by simple deposition technology and annealing process (Fig. 8(a)) [191]. The CdSe produced by the deposition process had better catalytic activity than that produced by the annealing process due to the formation of CdO film on the annealed surface in air, which produced resistance and affected the electrochemical catalytic performance. The electrocatalytic activity can be improved by coating the surface of CdSe with a thin metal (Pd). The deposited CdSe showed an η_{10} of 300 mV (Figs. 8(b) and 8(c)). Kim et al. fabricated CoTe nanotube film via a hydrothermal deposition coupled with reflow process [192]. SEM images showed that the surface of CoTe nanostructure was still porous and granular at the annealing temperature of 200°C, which accelerated the penetration of electrolyte and provided a more active surface for fast chemical reaction (Figs. 8(d)–8(g)). Joya et al. constructed NiO_x nanofilms on the surface of FTO by low temperature spraying [193]. Fominski et al. constructed MoOz(S)/WO_3/FTO heterostructure as photocatalytic oxygen evolution material by using MoS_x nanofilm as the precursor [194]. When the sulfur concentration in MoS_x films increases from $x = 2$ to $x = 4.5$, there is no difference in conductivity type. However, $MoS_{4.5}$ film showed the smallest energy band gap because the oxidation–reduction ability of charge carriers in the $MoS_{4.5}$ film is stronger than MoS_2 and $MoS_{3.2}$ (Fig. 8(h)). Light absorption leads to the generation of electron hole pairs in MoOz(S) and WO_3

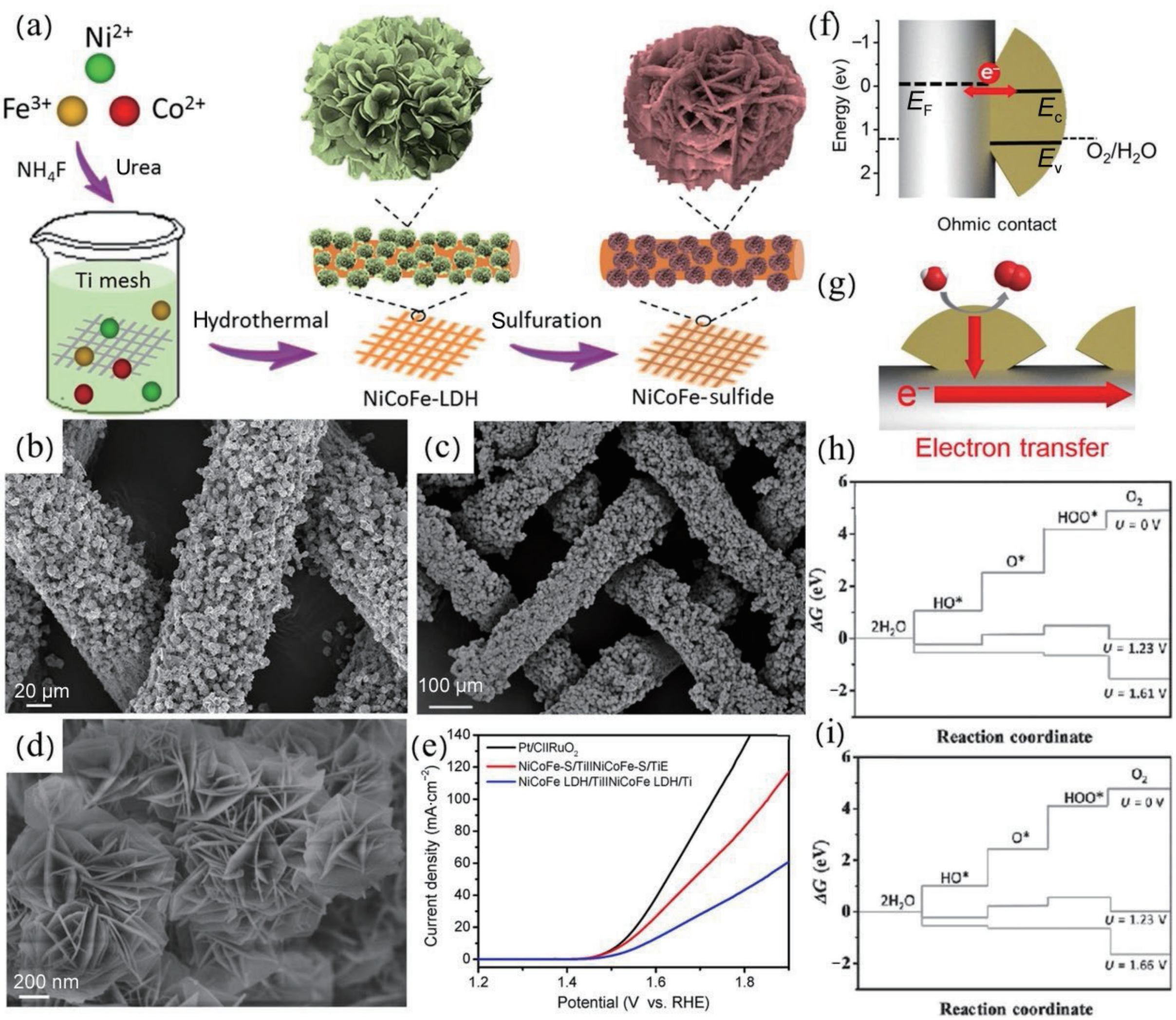

Figure 7 (a) Schematic of the synthesis of NiCoFeS/Ti. (b) and (c) SEM images of NiCoFe-LDH/Ti. (d) SEM image of NiCoFe-LDH/Ti after vulcanization. (e) Overpotential comparison. Reproduced with permission from Ref. [181], © Elsevier Ltd. 2020. (f) Electronic structure of Ti@$Co_{0.85}$Se ohm contact. (g) Strategy of Ti@$Co_{0.85}$Se hybrid structure for enhancing the electron transfer. Reproduced with permission from Ref. [182], © Elsevier Ltd. 2017. Free energy diagrams for (h) Fe-Ni_3S_2 and (i) Ni_3S_2. Reproduced with permission from Ref. [186], © WILEY-VCH Verlag GmbH & Co. KGaA, Weinheim 2017.

films. If the catalytic activity of MoOz(S) films is higher than that of WO_3, the accumulated holes in MoOz(S) films can improve the OER of MoOz(S)/WO_3/FTO surface (Fig. 8(i)).

In the general discussion, the self-supported catalysts grown on different substrates are promising candidates for the OER electrocatalysts, and have usually better OER performance than the non-substrated chalcogenide catalysts (Table 2). The close interaction between the substrate and the catalyst ensures the integrated structure of the catalyst in the harsh environment, and the use of no binder greatly simplifies the construction process and facilitates practical application. It can also effectively improve the electrochemical interface and the mass transport rate.

5 Optimization strategy of self-supporting chalcogenides

Optimization strategies such as vacancy engineering, heteroatomic doping, defect engineering, and interface engineering can enable the surface reconstruction of transition metal sulfide catalysts in the OER process, which will be finally reconstructed as hydroxides or amorphous species as real catalytically active species, thus improving the OER performance by reducing the energy barrier.

5.1 Vacancy engineering

The introduction of vacancies improves the conductivity and promotes the surface reaction kinetics [201]. The development of vacancy engineered sulfur-containing electrocatalysts has attracted extensive attention [202]. For example, Ganesan et al. constructed a hybrid electrocatalyst $(Fe_3NiS_{8-\delta})^{-4+\delta}$ on CNTs [203]. By controlling the composition ratio of Ni/Fe ions (Ni/Fe: 1/4, 2/3, and 3/2), it was found that the best Ni/Fe ratio is 2/3, and the high performance comes from the Fe^{III} self-doped d-p orbital formed by sulfur vacancy. DFT calculations showed that carbon nanotubes as a substrate successfully stabilized the valence state of Fe^{III}, reduced the energy barrier of O–O bond cracking, and thus promoted catalytic activity. Metals and nonmetals play an important role in vacancy engineering for the OER. Su et al. synthesized Ru-$NiCo_2S_{4-x}$ through a simple solvothermal photochemical two-step reaction strategy (Figs. 9(a) and 9(b)) [204]. The effects of V_S and metal Ru on the rate determination step and reaction barrier of $NiCo_2S_4$ were studied by DFT calculations (Fig. 9(c)). The phenomenon of "delocalization and confinement" of electrons caused by the anchoring of V_S and metal Ru promotes the interaction between electrons, reduces the barrier of reaction activity effectively, and is conducive to the desorption of O_2. The Ru-$NiCo_2S_{4-x}$ showed a low η_{50} of 190 mV (Fig. 9(d)), much lower than $NiCo_2S_4$, $NiCo_2S_{4-x}$, and Ru-$NiCo_2S_4$. Gao et al. synthesized ruthenium doped and sulfur vacancy Vs-Ru-Ni_9S_8 electrocatalyst by a simple and economical one-step hydrothermal method [205],

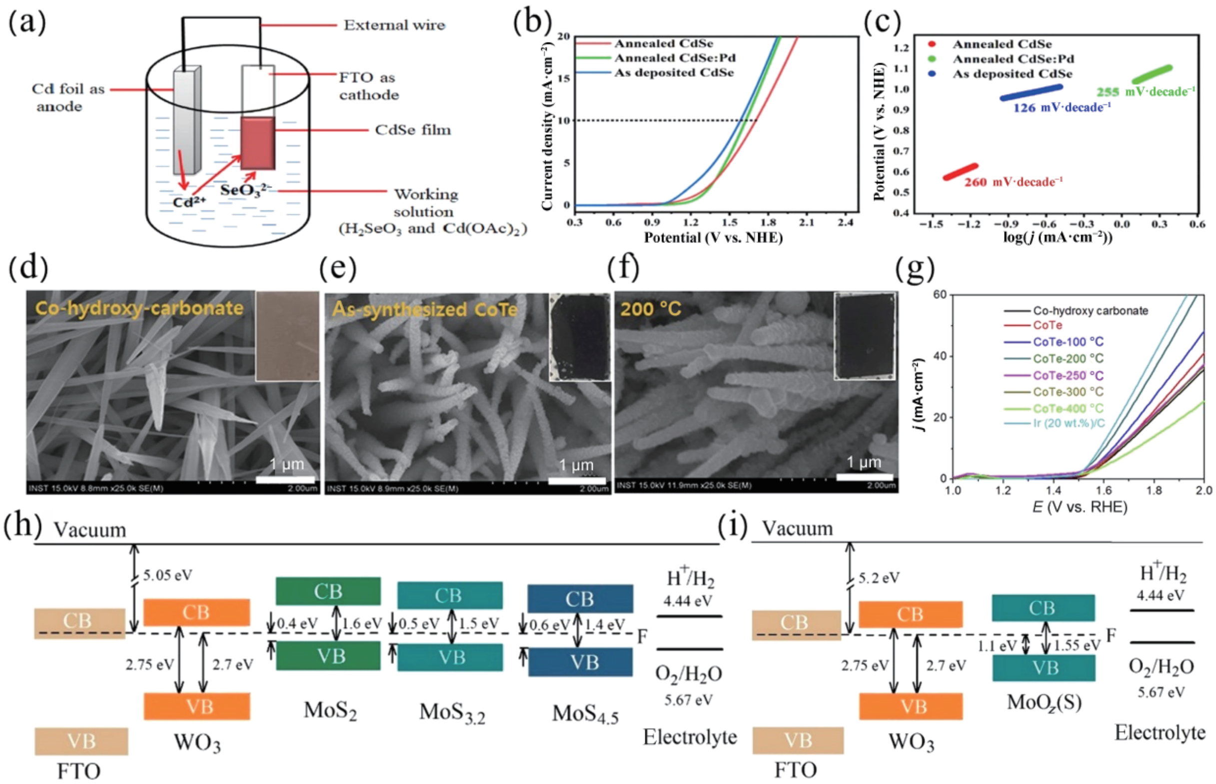

Figure 8 (a) Schematic diagram of electrodeposition of CdSe galvanized electrode, (b) LSV curves, and (c) Tafel plots. Reproduced with permission from Ref. [191], © Elsevier B.V. 2021. (d)–(f) SEM images of cobalt hydroxy-carbonate film, as-synthesized CoTe film, and CoTe film. (g) LSV curves. Reproduced with permission from Ref. [192], © Elsevier Ltd. 2017. (h) and (i) Band diagrams of MoOz(S)/WO_3/FTO. Reproduced with permission from Ref. [194], © Fominski, V. et al. 2020.

Table 2 OER performance on non-self-supported transition metal chalcogenides

Electrocatalysts	Electrolyte	η_{10} (mV)	Tafel slope (mV·dec^{-1})	Ref.
Co-CoO@NSC	1 M KOH	279	83	[254]
$NiCo_2S_4$	1 M KOH	337	64	[71]
3DOM N-$Co_{0.8}Fe_{0.1}Ni_{0.1}S_x$	1 M KOH	370	75	[255]
Co-Fe-S-1	1 M KOH	283	92.7	[256]
$Ni_{0.13}Co_{0.87}S_{1.097}$	1 M KOH	316	54.72	[257]
Co-S-O BBHS	1 M KOH	285	49.67	[258]
CoNiFeS-350	1 M KOH	288	72	[85]
$Ni_{1.29}Co_{1.49}Mn_{0.22}S_4$	1 M KOH	348	65	[259]
$Co_xNi_{1-x}S_2$, CNS	1 M KOH	290	46	[260]
CoCuFe-S	1 M KOH	300	79	[261]
c-Ti-Fe-S	1 M KOH	350	55	[262]
CoFeS	1 M KOH	290	52.6	[263]
CoS	1 M KOH	383	38	[264]
MCS@a-Ni_3S_2	1 M KOH	333	150.1	[265]
$CuCo_2S_4$	1 M KOH	290	81.3	[266]
$CoFe_{0.2}S_x$	1 M KOH	304	48.7	[267]
Ni/NiS/NC	1 M KOH	337	45	[268]
H-Fe-CoMoS	1 M KOH	282	58	[269]

showing ultra-low overpotentials of 218 and 268 mV at 100 and 300 mA·cm^{-2}, respectively. DFT calculations showed that the doped Ru atoms play a role in weakening the adsorption and in regulating the electron density in OER, which makes the surface adsorption strength of OER intermediates on the catalyst not strong or weak, and significantly improves the OER catalytic performance. The metal-vacancy pair composed of Ni atom and sulfur vacancy as the catalytic active site, showed catalytic synergy in the OER. Sulfur vacancy improves the OER performance by reducing the energy barrier and optimizing the adsorption free energy of oxygen-containing intermediates (OH*, O*, and OOH*). Huang et al. synthesized P-doped NiS_2 electrocatalyst with layered structure by phosphorylation using Prussian blue analog nanotubes as precursors [206]. DFT calculations showed that the P element not only acts as a new active site, but also enhances the electrochemical activity of Ni and S sites. The P-

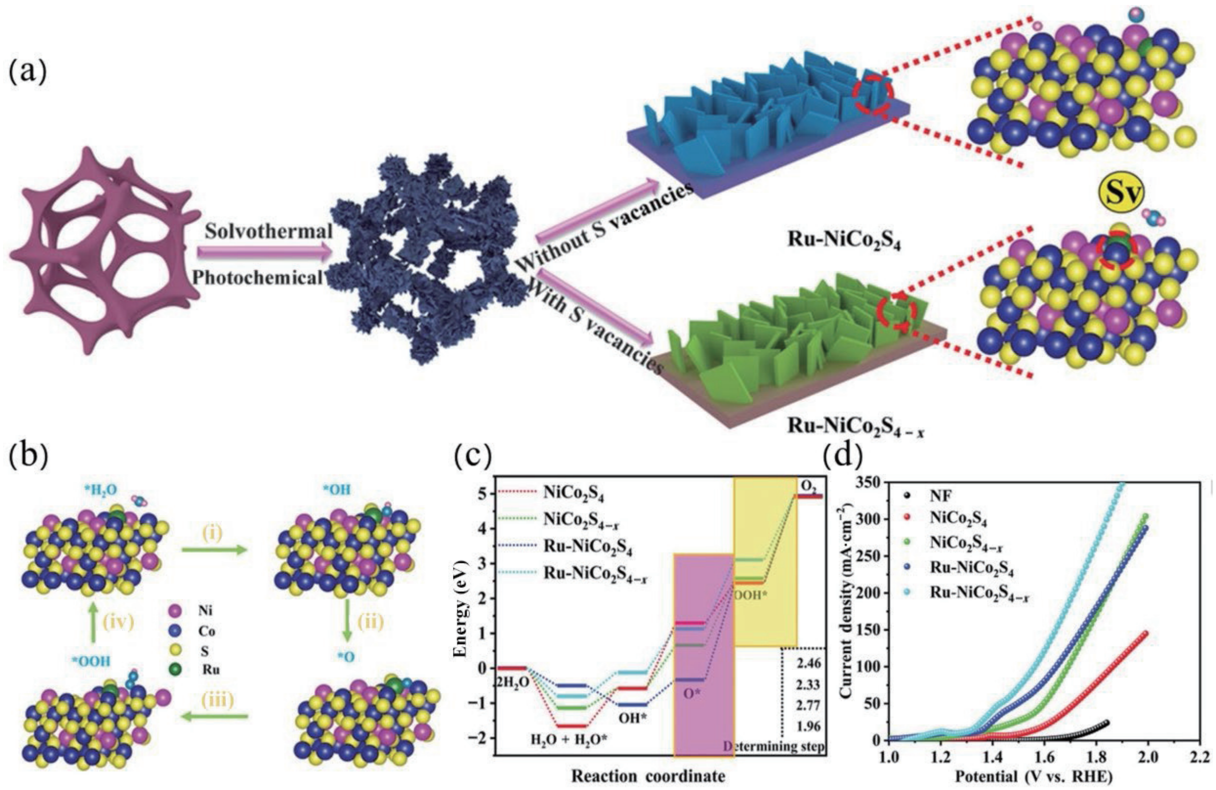

Figure 9 (a) Schematic of the synthesis of catalysts with and without S vacancy. (b) Structures models of Ru-$NiCo_2S_{4-x}$ for adsorption of intermediates (HO*, O*, and HOO*) for OER. (c) Calculated free energy diagram of $NiCo_2S_4$, $NiCo_2S_{4-x}$, Ru-$NiCo_2S_4$, and Ru-$NiCo_2S_{4-x}$. (d) LSV curves. Reproduced with permission from Ref. [204], © Wiley-VCH GmbH 2021.

doped NiS_2 electrode exhibited a low η_{20} of 255 mV in 1.0 M KOH.

Creating oxygen vacancies in electrocatalysts is a common and effective method to promote OER [207]. As revealed by the OER mechanism, all intermediates interact with the transition metal oxide surface through oxygen atoms, and the presence of oxygen vacancies will change the absorption and desorption process of the electrocatalyst and the reactants [208]. Oxygen vacancies also provide electrons, which lowers the Fermi level, enhances the electronic conductivity, and promotes charge transfer, thus affecting the OER performance. Zhuang et al. prepared $FeCoO_x$-Vo-S nanosheet catalyst by heat treatment synthesis strategy (Fig. 10(a)) [209]. The addition of S atoms modifies and stabilizes the oxygen vacancy, and forms Co–S coordination, which effectively regulates the electronic structure of the active site (Fig. 10(b)). The $FeCoO_x$-Vo-S electrocatalyst only needed an η_{50} of 240 mV in 1.0 M KOH (Figs. 10(c) and 10(d)). Jaouhari et al. studied the internal and dynamic behavior of selenium vacancies in $CoNiSe_2$ film on carbon cloth [210]. They found that selenium vacancies on the surface of $CoNiSe_2$ adjusted the electronic structure and promoted the adsorption of active sites by hydroxides, thus promoting the formation of Co/NiOOH, which can effectively adjust the center of d-band and the change of Gibbs free energy between different OER steps and enhance the catalytic activity of OER (Figs. 10(b)–10(d)). The defective $CoNiSe_2$ exhibited a low η_{10} of 252 mV, a low Tafel slope, and good stability.

5.2 Heteroatom doping

5.2.1 Metal doping

Doping metal elements (such as Fe, Mn, Cu, Co, etc.) to adjust the surface characteristics of catalysts is another common method to improve the OER performance [211, 212]. Metal cations can adjust the ligand field of the active center and have certain influence on the electronic configuration [213]. For example, Xie et al. synthesized Fe doped Ni_3S_2 electrocatalyst on 3D NF (Fe-doped Ni_3S_2–NF) by a simple one-step vulcanization method (Fig. 11(a)) [143]. The nucleation morphology and growth characteristics of Fe doped Ni_3S_2 on NF surface can be controlled by optimizing the reaction time and temperature. Fe doped Ni_3S_2 has low crystallinity in the (110) plane, and the changes of electronic structure and charge carrier density improve the electrocatalytic activity (η_{10} = 166 mV). Zare et al. synthesized Fe doped $CoSe_2$ nanoparticles on NF (Fe-$CoSe_2$/NF) using simple and economical electrodeposition technology [199]. The optimized Fe-$CoSe_2$/NF exhibited an η_{10} of 220 mV and small Tafel slope of 35.6 $mV\cdot dec^{-1}$ in 1.0 M KOH. Wu et al. prepared Fe doped Ni_3S_2 nanowires on nickel foam by one-step solvothermal method (Fig. 11(c)) [214]. When the content of dopant Fe was 13.7%, only 223 mV overpotential was needed to reach 200 $mA\cdot cm^{-2}$ in alkaline electrolyte. Fe doping into Ni_3S_2 nanowires increases the number of active site edges, changes the morphology, adjusts the electronic structure, and enhances the conductivity. The interaction between the surface atoms of the catalyst and the reactants can neither be too strong nor too weak, which shows the maximum catalytic activity to a certain extent [215, 216]. The metallic element Mn is also a promising doping material [217, 218]. Yu et al. prepared Mn doped $NiCo_2S_4$/NF three dimensional nanospheres by three-step hydrothermal synthesis [200], which showed excellent OER activity with a low η_{10} of 228 mV. Yuan et al. synthesized self-supporting Mn-doped Ni_3S_2 on NF (Mn-Ni_3S_2/NF) via one-step hydrothermal treatment [219], which showed enhanced OER activity with an η_{100} of 347 mV. The addition of Mn optimizes the electronic structure and enhances the conductivity, so as to achieve fast mass transfer. Kuila et al. used electrodeposition technology to construct a self-supporting Ni doped FeS electrocatalyst on NF [220]. By changing the electrodeposition time to control the amount of doped Ni, they found that the electrode prepared by depositing at 0.9 V for 30 min showed excellent catalytic activity. Ni doped into the lattice

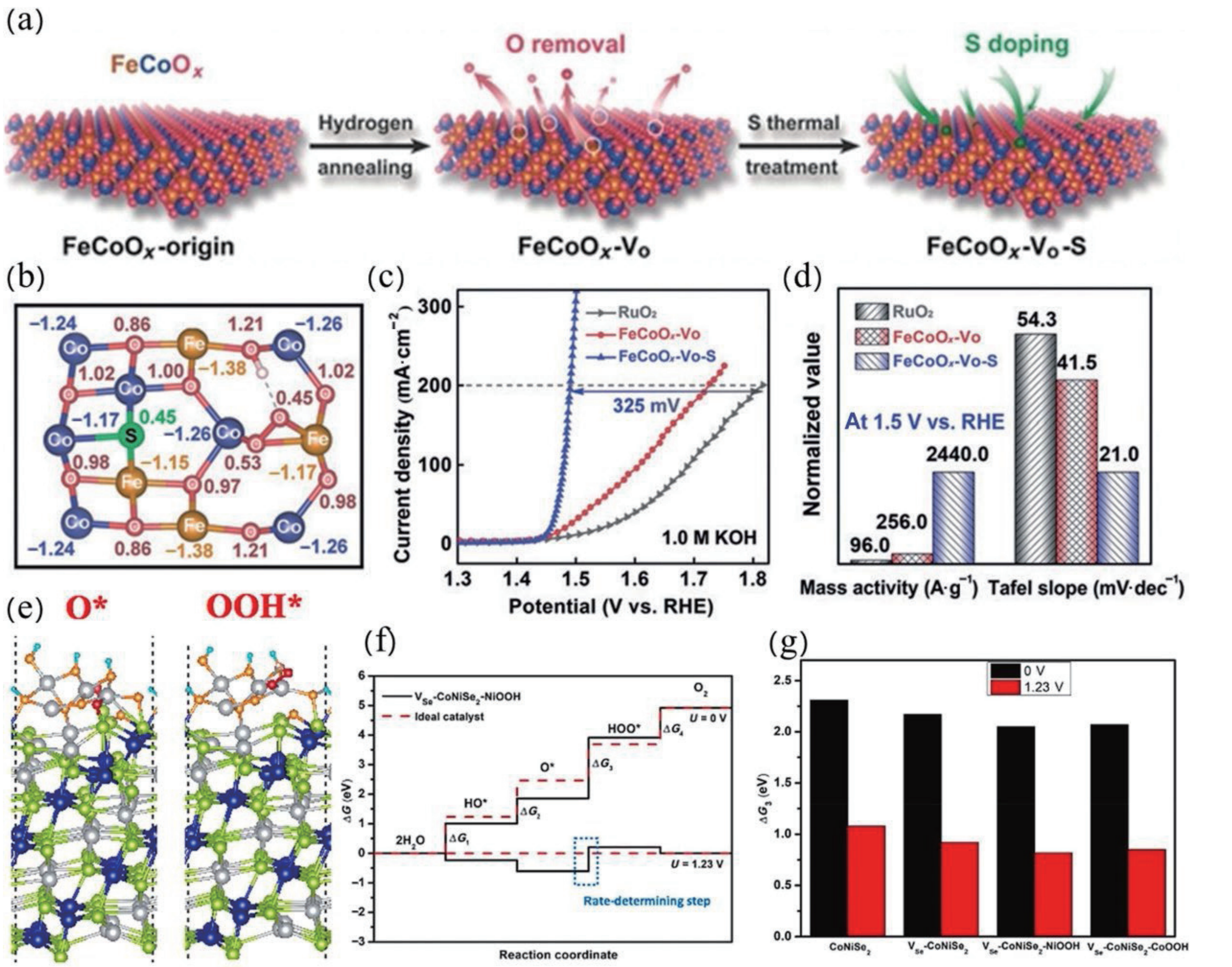

Figure 10 (a) Preparation process of $FeCoO_x$-Vo-S. (b) The Bader charge number of atoms when $FeCoO_x$-Vo-S is at the most appropriate level of OOH* adsorption strength. (c) LSV curves. (d) The comparison of mass activity and Tafel slope. Reproduced with permission from Ref. [209], © Wiley-VCH Verlag GmbH & Co. KGaA, Weinheim 2020. (e) Adsorption structure and (f) Gibbs free energy of intermediate of V_{Se}-$CoNiSe_2$-(102)-NiOOH. Green, blue, gray, orange, and cyan balls denote Se, Co, Ni, O, and H atoms, respectively. (g) Comparison of rate determination steps ($\Delta G_3 = |\Delta G_O - \Delta G_{OOH}|$). Reproduced with permission from Ref. [210], © Elsevier B.V. 2021.

domain of FeS can adjust the electronic structure and increase the charge density, which significantly improves the electrocatalytic activity.

In contrast to S and Se atoms, Te exhibits more metallic properties that can improve the electronic conductivity, leading to positive electrocatalytic properties. Sadaqat et al. used a simple one-step hydrothermal method to synthesize hexagonal nano ultra-thin electrocatalyst on foam nickel ($Ni_{0.4}Fe_{0.6}Te_2$/NF) with a thickness of about 21.3 nm [152]. The morphology and electronic structure were optimized by adjusting the concentration of Fe doping. Due to the synergistic effect of bimetallic and unique nanosheet structure, the electrocatalyst exhibited excellent OER performance. The low over-potential at the current density of 10, 100 and 500 $mA \cdot cm^{-2}$ is 190, 274, and 330 mV, respectively. According to the results of XPS test, the excellent OER activity of the electrocatalyst was attributed to the ability of various lattice oxygen changes in NiFeOOH (Te)/NF and the dual electronic effect, which reduced the free adsorption energy of the intermediate, resulting in high OER activity.

5.2.2 Non-metallic doping

Non-metallic elements (such as N, P, and F) as dopants can adjust the adsorption/desorption behavior, so as to improve the electrocatalysis ability [221]. He et al. constructed 3D self-supporting P-doped Ni_3S_2 nanosheet arrays on NF via a simple hydrothermal method combined with phosphating and vulcanization processes [198]. The prepared electrode showed enhanced OER activity with an η_{10} of 256 mV. The addition of P anion optimizes the adsorption of OER intermediates, adjusts the electronic structure, and greatly improves the electrochemical surface area and conductivity. Ding et al. synthesized P-doped Ni_3S_2 electrode material on NF by hydrothermal synthesis technology [222]. The doping of P element optimizes the electronic structure and provides simple adsorption of reactants, so as to achieve faster electron transfer speed. The optimized PNi_3S_2/NF exhibited an η_{100} of 306 mV. Liu et al. proposed a dual regulation strategy to construct nitrogen doping and carbon coating N-Ni_3S_2@C/NF electrode material [223]. The introduction of nitrogen accelerated the mass transfer, increased the number of active sites, and thus improved the catalytic activity. The optimized electrode showed excellent OER activity with an η_{10} of 100 mV. Kumar et al. synthesized Co/Co_9S_8/CNT nanowires doped with N and S atoms by thermal decomposition [224]. Due to the modification of N, the doping of S and the synergistic effect between graphene layer and metal, the electronic structure of Co is greatly adjusted to make it in the highest valence state. Compared with Co/CNT, Co/Co_9S_8/CNT showed higher OER activity. Wang et al. synthesized 3D self-supporting N-Co_4S_3/Ni_3S_2/NF nanosheets through hydrothermal treatment and calcination (Fig. 11(b)) [225]. N doping can optimize the d-band structure, overcome the inherent limitations of reaction kinetics, and improve the charge transfer ability and water oxidation ability. In

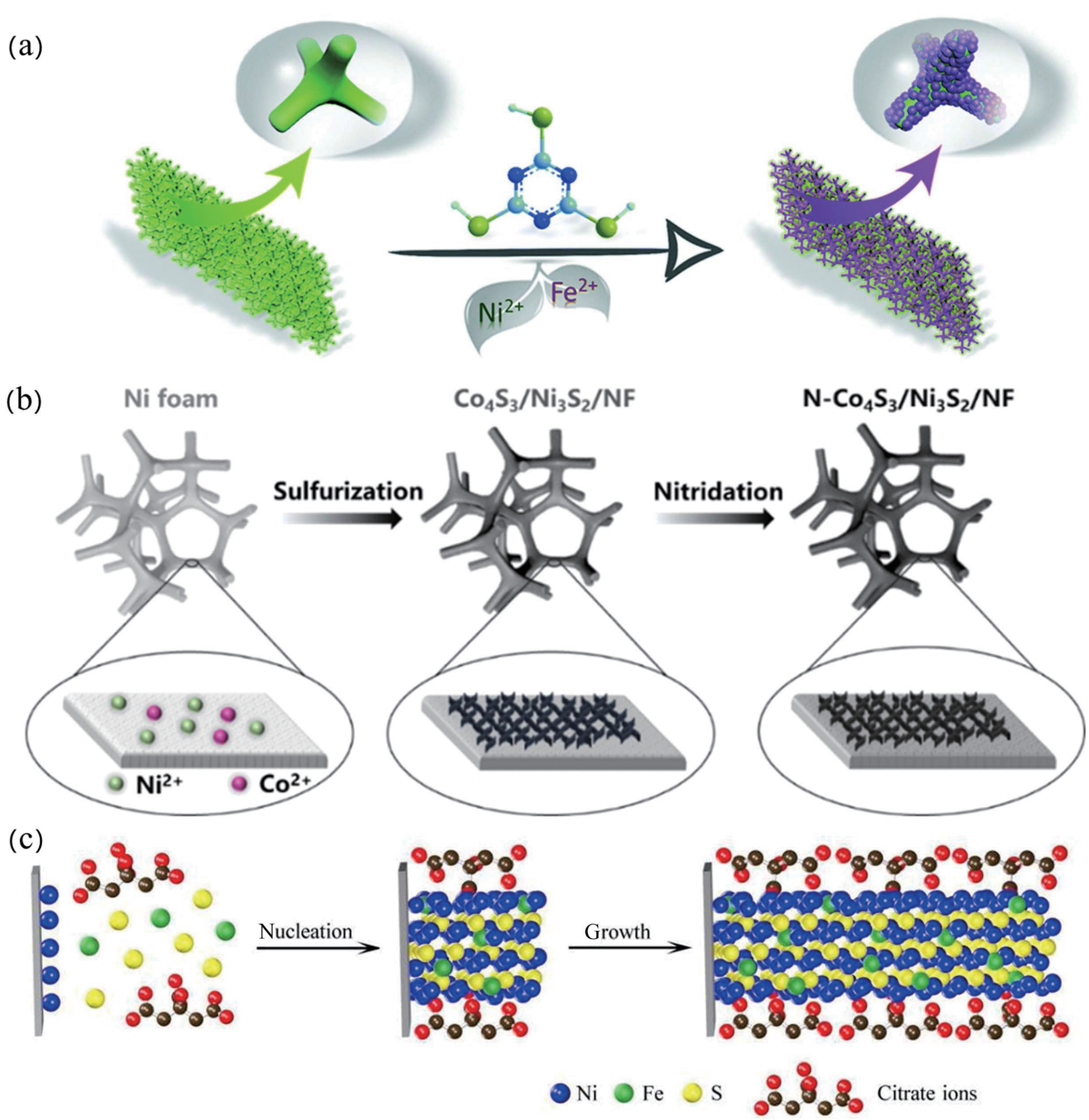

Figure 11 (a) Synthetic process of Fe-doped Ni_3S_2-NF. Reproduced with permission from Ref. [143], © The Royal Society of Chemistry 2021. (b) Preparation of N-Co_4S_3/Ni_3S_2/NF. Reproduced with permission from Ref. [225], © 2021 The Electrochemical Society ("ECS"). Published on behalf of ECS by IOP Publishing Limited. (c) Schematic representation for the fabrication of Fe-doped Ni_3S_2 nanowires on NF. Reproduced with permission from Ref. [214], © Wiley-VCH Verlag GmbH & Co. KGaA, Weinheim 2019.

addition, the defects induced by N doping provide rich catalytic sites, showing excellent OER catalytic activity. The optimized N-Co_4S_3/Ni_3S_2/NF exhibited an η_{100} of 331 mV.

5.3 Edge engineering

The active crystal plane with active valence bonds and high-density atomic ladder at the edge can realize rapid electron transfer between the surface and the interior of the system [226]. For highly exposed edge sites, edge engineering can adjust the growth dynamics to produce different electronic structures and achieve high OER performance [227–230]. There are abundant exposure sites at the marginal Mo sites. MoS_2 has a significant impact on the catalytic performance of water splitting due to its unique structure and electronic properties [231, 232]. Liu et al. synthesized 2D 1T-MoS_2 nanosheets precursor by Na^+ intercalation combined with stripping method, and then hybridized it with 30 wt.% carbon nanotubes to construct a self-supporting oxygen electrode 1T-MoS_2/CNT without adhesive (Fig. 12(a)) [233]. The metal Mo edge is oxidized and passivated in 2H-MoS_2, and the plane has no catalytic activity, resulting in the inability to generate O_2. The stripped 1T-MoS_2 has superior catalytic activity due to the synergistic effect between the metal Mo and the carbon porous substrate, which accelerates the charge transfer and generates a large number of reaction sites. 1T-MoS_2 showed an OER η_{10} of 1.52 V, which is much lower than that of both 2H-MoS_2 and Pt/C (Fig. 12(b)). Wang et al. synthesized CoS-MoS_2/Ni_3S_2/NF nanoarray electrocatalyst on nickel foam by microwave-assisted hydrothermal method and subsequent electrodeposition (Fig. 12(c)) [234]. CoS-MoS_2/Ni_3S_2 was deposited on NF at 4, 8, and 12 different deposition cycles and the obtained MoS_2/Ni_3S_2/NF at 12 cycles exhibited better catalytic activity (Fig. 12(e)). Benefiting from the porous network structure and high conductivity, the as-obtained CoS-MoS_2/Ni_3S_2/NF showed a low η_{100} of 225 mV in 1.0 M KOH (Figs. 12(d)–12(f)). Yu et al. synthesized porous Ni_3FeN nanosheets on N-WS_2 particles on NF (N-WS_2/Ni_3FeN) via two-step nitration method as self-supporting electrodes [235]. The combination of the catalyst and the conductive substrate produces rich edge sites, and the

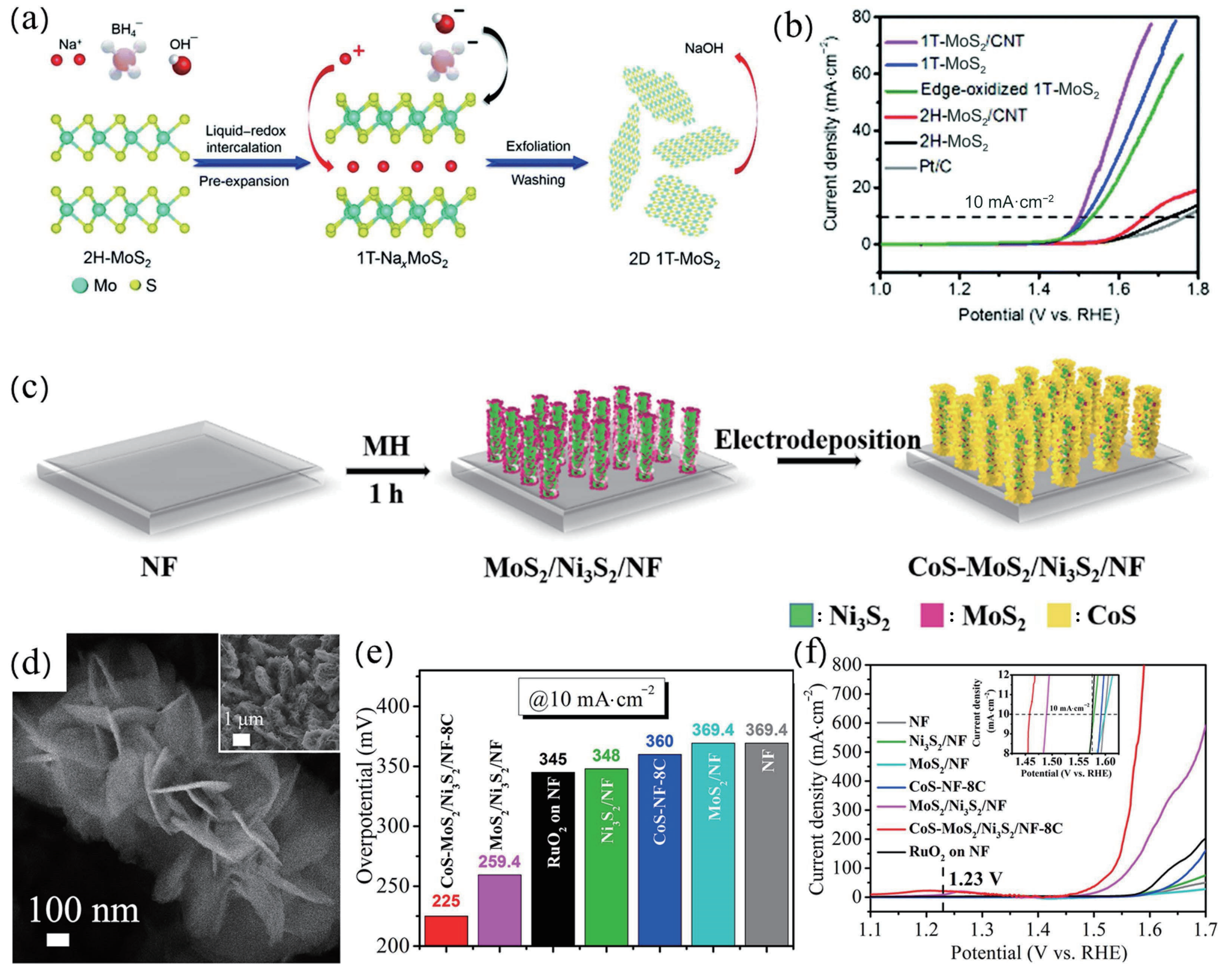

Figure 12 (a) Synthetic illustration of 2D 1T-MoS_2. (b) LSV curves. Reproduced with permission from Ref. [233], © The Royal Society of Chemistry 2018. (c) Synthetic illustration of CoS-MoS_2/Ni_3S_2/NF. (d) SEM images of CoS-MoS_2/Ni_3S_2/NF-8C. (e) η_{10} of different electrocatalysts. (f) LSV curves. Reproduced with permission from Ref. [234], © Hydrogen Energy Publications LLC 2018.

heterostructure accelerates the electron transfer. The N-WS_2/Ni_3FeN nanosheets exhibited an η_{500} of 285 mV in alkaline condition.

5.4 Surface morphology engineering

Surface morphology engineering is considered as an effective method to enhance the exposure of active sites and improve the mass transfer process, which is widely used in surface engineering [236]. One-dimensional nanostructure can provide electron transfer pathways, enhance gas diffusion, and thus improve catalytic activity. The well-arranged one-dimensional nanostructure array is grown *in situ* on the conductive substrate. The large specific surface area promotes mass transfer, exposes a large number of catalytic sites, and enhances the catalytic activity of OER [237]. Li et al. synthesized a self-supporting $NiCo_2S_4$/FeOOH nanowire array electrocatalyst without adhesive by hydrothermal preparation and subsequent selective anion exchange (Fig. 13(a)) [238]. The interface structure of $NiCo_2S_4$ and FeOOH provides many different active sites, which helps to reduce the energy barrier, adjust the electronic structure, and optimize the adsorption energy of intermediates (Figs. 13(b)–13(d)). DFT calculations showed that the enhancement of OER performance is attributed to the increase of FeOOH and the synergy of multiple sites (Fig. 13(e)). The optimized $NiCo_2S_4$/FeOOH nanocomposite exhibited an η_{10} of 200 mV and Tafel slope of 71 mV·dec^{-1} in alkaline condition. Feng et al. prepared NiMoSe/NF-2 nanoarray catalyst by hydrothermal and selenide two-step synthesis [239]. Selenium doped NiOOH is the real active site, showing the phase transition of low covalent Ni species into the oxidation state of selenium doped NiOOH. The free energy of the selenium doped NiOOH is the closest to zero (Fig. 13(g)) and the rate determining step is the third electron transfer process (Fig. 13(h)). Rich interface disorder and high conductivity endowed NiMoSe/NF-2 with good OER performance, showing an η_{100} of 307 mV, a small Tafel slope of 30.9 mV·dec^{-1}, and good stability in 1.0 M KOH (Figs. 13(i) and 13(j)). Yao et al. successfully constructed CoO_x modified cuprous sulfide nanowire array on Cu foam (Cu_2S-CoO_x/CF) by nitration pyrolysis (Fig. 13(f)) [240]. Cu_2S-CoO_x/CF showed better catalytic performance than Cu_2S/CF and CoO_x/CC due to synergistic effect and regulation of active sites on the interface. The defective Cu_2S-CoO_x/CF exhibited a low η_{25} of 255 mV and good stability. Deng et al. successfully constructed Cu_2S/TiO_2/Cu_2S branched nanowire arrays on the substrate TiO_2 through deposition and vulcanization [195]. The Cu_2S/TiO_2/Cu_2S core–branch arrays with rich interfaces exhibited superior OER performance, with an η_{10} of 284 mV, and Tafel slope of 72 mV·dec^{-1} in alkaline condition. Wang et al. prepared self-supporting N-Ni_3S_2/N-MoS_2/NF electrode via hydrothermal method and subsequent annealing process. N-doped Ni_3S_2/MoS_2 heterostructure was synthesized *in situ* on $NiMoO_4$ nanowire arrays [241]. The incorporation of nitrogen anions causes vacancies and increases the active sites, and the special heterostructure has strong electronic interaction, which helps to enhance the OER activity.

5.5 Construction of heterostructure

The combination of different components and elements will produce interaction, leading to strong synergy between electrons,

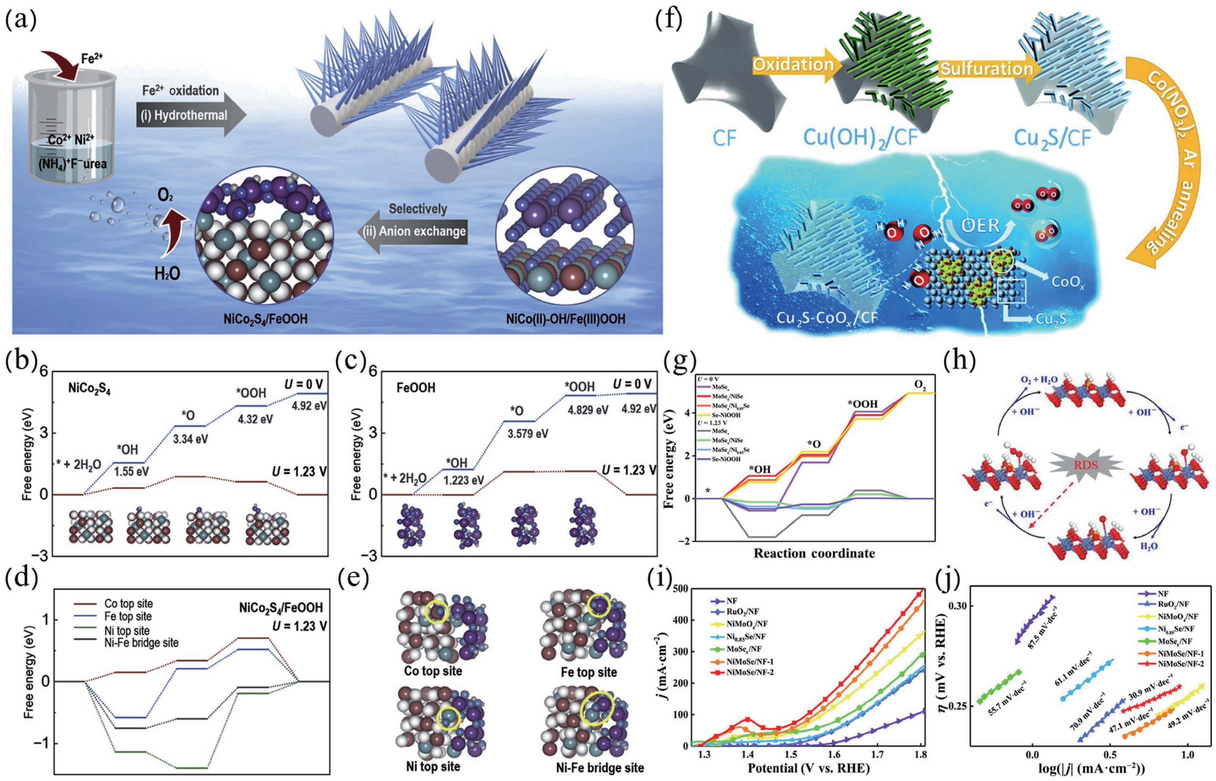

Figure 13 (a) Synthetic illustration of $NiCo_2S_4$/FeOOH. Free energy diagram of the OER on (b) $NiCo_2S_4$, (c) FeOOH surface, and (d) $NiCo_2S_4$/FeOOH. (e) Schematic to show different active sites in $NiCo_2S_4$/FeOOH. Reproduced with permission from Ref. [238], © Elsevier Ltd. 2020. (f) Schematic synthesis of Cu_2S-CoO_x/CF. Reproduced with permission from Ref. [240], © The Royal Society of Chemistry 2020. (g) Free energy diagram of the OER at 0 and 1.23 V. (h) Schematic diagram of OER mechanism. (i) Electrocatalytic performance in 1 M KOH and (j) Tafel slopes. Reproduced with permission from Ref. [239], © Feng, W. S. et al. 2021.

thus displaying higher catalytic activity than the corresponding single component [242, 243]. Constructing heterostructure is a primary method to construct advanced electrocatalysts for improving catalytic performance. The construction of interfacial synergy is conducive to the chemisorption of oxygen-containing intermediates [244]. Feng et al. prepared heterogeneous MoS_2/Ni_3S_2 electrocatalyst on NF by a simple one-step solvothermal method [245]. DFT calculations showed that due to the electronic interaction at the MoS_2/Ni_3S_2 heterogeneous interface, the Gibbs free energy of the OER intermediates is effectively reduced, which promotes the dissociation of O_2 intermediates, thus accelerating the OER process and improving the catalytic activity (Fig. 14(a)). For the OER, the MoS_2/Ni_3S_2 showed a low η_{10} of 218 mV in alkaline condition. Zhang et al. synthesized self-supported three dimensional layered MoS_2/NiS_2 heterostructure on carbon cloth by simple solvothermal method [246]. Ni ions were vertically staggered on CC, and then Mo ions were attached to the nanosheets array, and NiS_2/MoS_2 heterojunction was formed after vulcanization. MoS_2/NiS_2 heterostructure has rich defects, leading to the increase of active sites and exhibiting good catalytic activity with an η_{10} of 303 mV. Mg^{2+} has high hydration, which can improve the adsorption of water molecules on the catalyst surface. Wang et al. synthesized MgO/$NiCo_2S_4$ heterostructure on CC (MgO/NCS-CC) via electrodeposition and annealing (Fig. 14(b)) [197]. DFT calculations showed that the heterostructure between MgO and $NiCo_2S_4$ makes electrons flow from Ni to Co and Mg, changes the electronic structure, and redistributes charges (Fig. 14(c)). The heterojunction formed by the addition of Mg^{2+} enhances the adsorption of water on the surface of the electrocatalyst and improves the electrocatalytic OER activity (η_{10} = 145 mV) (Figs. 14(d) and 14(e)). Huang et al. synthesized Ni_3S_2-NiO_x heterostructure on NF (Ni_3S_2-NiO_x/NF) by plasma processing technology (Fig. 14(f)) [196]. According to the *in-situ* Raman spectra, prolonging the electrolysis time leads to the *in-situ* reconstruction of the active heterogeneous interface. Too much active substance NiOOH accumulates on the surface area of Ni_3S_2, which hinders the charge transfer and reduces the catalytic activity of OER (Fig. 14(g)). The Ni_3S_2 on Ni_3S_2/NF is easier to be oxidized to NiOOH than Ni_3S_2-NiO_x/NF, and thus the catalytic OER performance is improved by doping buffer surface oxidation (Fig. 14(h)). Li et al. prepared self-supporting CoS_2/Cu_2S heterostructure composite electrode material on NF (CoS_2/Cu_2S-NF) via electrospinning technology and annealing process [247]. The electrons in CoS_2/Cu_2S heterostructure interact with each other, accelerate the electron transfer, regulate the electronic structure of Co and Cu sites, and enhance the OER activity. Cai et al. anchored FeOOH on the surface of Ni_3S_2 nanosheets by chemical immersion method to form FeOOH-Ni_3S_2 heterostructure [248], which leads to strong synergistic effect between electrons, thus showing higher catalytic activity (η_{10} = 190 mV) than the original Ni_3S_2. A heterostructural material of NiTe-NiSe without toxic hydrazine was synthesized by the hydrothermal method [249]. This nanosheet heterostructural material has many exposed active sites and good structural stability, in which electron transfer and synergistic effects between different components contribute to improved OER dynamics. Further investigating the introduction of NiTe into NiSe by DFT calculations revealed that the interface charge transfer promoted the adsorption capacity of the oxygen intermediate. NiTe-NiSe shows larger DOS values near the NiTe or NiSe model, which indicates that the cooperative duplex heterojunction interface formed by the introduction of NiTe can increase the electron density, enrich the free electron concentration, and then promote the OER catalytic process.

5.6 Study on OER mechanism through *in-situ* characterization technologies

With the gradual development of research in the field of

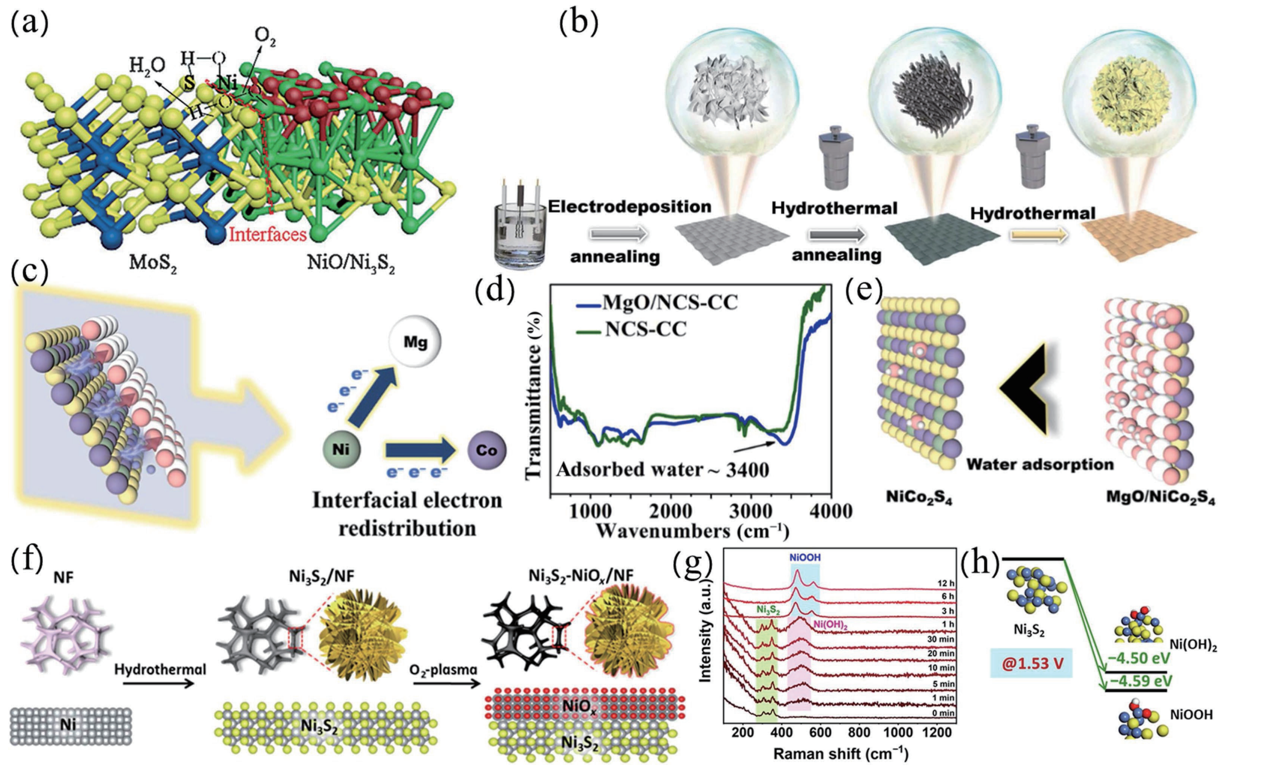

Figure 14 (a) Schematic diagram of dissociation mechanism of OER intermediates on MoS_2/Ni_3S_2. Reproduced with permission from Ref. [245], © WILEY-VCH Verlag GmbH & Co. KGaA, Weinheim 2016. (b) Schematic diagram of the preparation and morphology of the MgO/NCS-CC heterostructure. (c) Schematic diagram of electron transfer process in $MgO/NiCo_2S_4$. (d) FTIR spectra of MgO/NCS-CC and NCS-CC. (e) Schematic diagram of H_2O adsorption on $NiCo_2S_4$ and $MgO/NiCo_2S_4$. Reproduced with permission from Ref. [197], © Elsevier B.V. 2022. (f) Synthetic illustration of Ni_3S_2-NiO_x/NF. (g) *In-situ* Raman spectra related to the chronoamperometry test (g = 300 mV). (h) Free-energy diagrams of Ni_3S_2 reconstruction during OER. Reproduced with permission from Ref. [196], © Elsevier Inc. 2022.

electrocatalysis, researchers urgently need to further explore the reaction mechanism and structural change of the catalyst during the OER. *In-situ* characterization techniques can be used to better understand the structural changes of catalysts, real reaction intermediates, and the effective relationship between structure and OER property [250]. Different instruments can be used to carry out continuous and synchronous online analysis of specific substances, which is dynamic, real-time, and intuitive, by which we can observe the chemical reaction process, and structure and morphology changes in real time. *In-situ* XRD technology can provide precise crystallographic information such as lattice parameters and preferred orientation. Therefore, XRD can be used to analyze the strain, crystal facet, doping effect, and identify the crystal state of the catalyst surface. *In situ* X-ray absorption spectroscopy (XAS) analysis can be used to identify the active site, the change of oxidation state, and the deviation of atomic distance in the OER process. Liao et al. explored the catalytic OER mechanism over $FeCo_2S_4/NF$ catalyst by *in situ* XRD and XAS characterizations [251]. *In-situ* XRD results showed that $FeCo_2S_4/NF$ still maintained spinel structure under different voltages (Fig. 15(a)). XAS was used to analyze the influence of electronic and atomic structure, demonstrating that the intensity of the absorption peak was proportional to the number of unoccupied orbital states (Figs. 15(b) and 15(c)). Due to the dipole forbidden transition of 1s to 3d orbits, weak front edge features exist. When the potential was applied, the local structure of the symmetry of the crystal field was different or distorted, and the local structure became $Co(OH)_2$. The coordination sulfur was replaced by oxygen, which affects the electronic structure of Co. At 1.43 V, the oxidation state was close to +2 in cobalt hydroxide and there was Co–OOH with +3 valence on the surface. *In-situ* XPS can provide information about the electronic state and charge transfer behavior, making it easier to understand the electronic configuration changes during the OER electrocatalysis. Friebel et al. studied a Ni-Fe electrocatalyst for the OER through *in-situ* XPS [252]. The normalized XPS spectra in the Ni and Fe 2p region showed $Ni^{2+/3+}$ oxide and $Fe^{2+/3+}$ oxide (Figs. 15(d) and 15(e)). At 0.3 V, Fe ion was completely oxidized to Fe^{3+}, indicating that the Ni-Fe electrocatalyst was completely oxidized at a positive potential. *In-situ* Raman spectroscopy can be used for quantitative or semi-quantitative analysis of samples, which has the characteristics of fast and sensitive identification of characteristic vibration and wide testing range, especially for the study of amorphous or poorly crystalline materials. Cao et al. observed the Raman peaks of Co–O and Co–OOH bonds, and revealed the transformation of Co–O to Co–OOH species during the OER by changing the potential (Figs. 15(f) and 15(g)) [252]. It showed that the Co-OOH species is a real active substance, which makes the catalyst have excellent OER catalytic performance.

Electrocatalytic materials with high-density active centers but low conductivity would display poor overall catalytic performance. The surface engineering strategy is widely used to improve the electrocatalytic OER activity. By reasonably designing the surface morphology of the catalyst (such as 2D nanosheet and 3D nanosheet/rod/array structure), the active sites can be effectively created and increased, and the electron transfer efficiency can be improved. The whole charge transfer interface process can affect the performance of the catalyst. In addition, whether the catalyst is crystalline or amorphous has an impact on the activity and stability of OER. The controllable structure cannot be guaranteed under hot pressing and acid etching. It is necessary to develop efficient and simple methods to synthesize electrocatalytic materials with controllable structure and defects. Therefore, interface engineering is also very important to improve the performance of self-supported electrocatalysts.

Nano Res. 2023, 16(7): 8684–8711

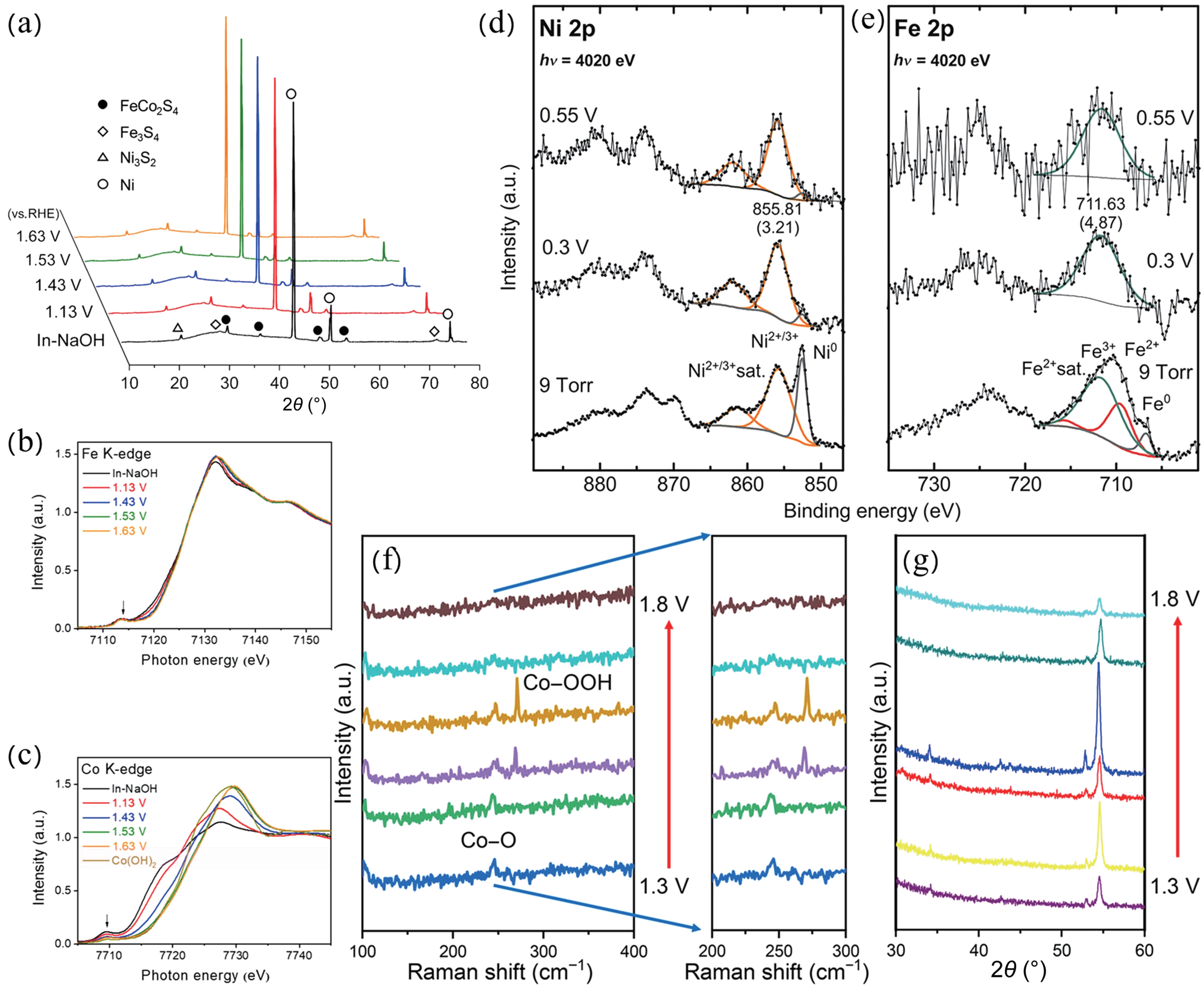

Figure 15 (a) XRD patterns of $FeCo_2S_4$/NF at different potentials. XANES spectra of (b) Fe and (c) Co K-edges. Reproduced with permission from Ref. [251], © American Chemical Society 2021. XPS spectra of (d) Ni 2p and (e) Fe 2p. Reproduced with permission from Ref. [252], © American Chemical Society 2016. (f) Raman spectra and (g) XRD patterns of EG/CoS_2/CoS_2-NC at different potentials. Reproduced with permission from Ref. [253], © Wiley-VCH Verlag GmbH & Co. KGaA, Weinheim 2019.

6 Conclusions and perspectives

The development of OER electrocatalysts with high efficiency, low cost, and stability is of great significance to the application of electrocatalytic water splitting. At present, most of the powder-like catalysts need to be fixed to the working electrode with adhesive in the performance evaluation process. Instead, the electrocatalyst is *in situ* self-supported on a conductive substrate to form a self-supporting electrode, and there is no aggregation without the use of polymerization agent, which is conducive to the adsorption and desorption processes, the release of produced gas, and the improvement of the activity and stability. In addition, the conductive substrate has high conductivity, which can accelerate the rapid transfer of charge and greatly increase the catalytic performance. In this review, the basic principles and main evaluation parameters of OER were introduced, including Tafel slope, overpotential, turnover frequency, and stability. Then, we systematically summarized the synthesis strategies for preparing various independent electrocatalysts, such as solvothermal/hydrothermal synthesis, electrochemical deposition, chemical vapor deposition, vacuum filtration, freeze-drying, and template synthesis methods. Afterwards, we emphatically discussed the OER performance of transition metal chalcogenides (including transition metal sulfides, selenides, and tellurides) grown on conductive substrates (NF, CC, CFP, and metal meshplate). Finally, we proposed advanced optimization strategies (including vacancy engineering, surface morphology engineering, heteroatom doping, and construction of heterostructure) to improve the inherent catalytic OER activity of self-supporting electrocatalysts.

Although great progress has been made in the design/synthesis of self-supporting chalcogenides, we cannot ignore some shortcomings and challenges in the current research. (1) Among the self-supporting chalcogenides, sulfides and selenides are relatively widely used, while transition metal telluride is very challenging in self-supporting materials due to the small content of tellurium in the earth's crust and its toxicity. Actually, tellurium has good electronic conductivity, which is better than selenium and sulfur, and its electronegativity is lower than selenium and sulfur, and therefore, it has stronger covalent properties when combined with metals. Therefore, the development of metal tellurides for the OER will become a research hotspot [270, 271]. (2) At present, the methods of synthesizing self-supporting electrodes are not suitable for large-scale preparation of large-area electrodes. In the future, advanced methods should be developed or combined with other technologies to prepare high-performance large-area OER electrodes. Although there are many preparation methods for constructing transition metal chalcogenides, and each synthesis method has its own characteristics, but it also has limitations. To date, there is still a lack of an effective way to synthesize self-supporting transition metal chalcogenides with high yield and low cost. (3) During the OER at high current densities, a lot of gas is produced which causes the transition metal chalcogenides to fall off the surface of self-supporting conductive substrates, thus reducing the catalytic activity. To avoid the use of adhesives, the efforts in the study of the electrocatalyst grown *in situ* on a conductive substrate should be considered. The development of self-supporting transition metal OER electrocatalysts that can maintain high activity and long-term stability at high current densities remains a challenging task in the future. (4) The OER mechanism on self-supported transition metal chalcogenides is not clear. At present, the most commonly proposed mechanism is the electron transfer between different metal chalcogenides to promote the adsorption of hydrogen or oxygen. The research on desorption process should be paid equal attention to, but the relevant research is very rare. Moreover, the composition of the interface between the conductive substrate and the catalyst is complex, which brings difficulties to understand the catalytic mechanism. (5) To better design the electrocatalyst, an advanced theoretical model should be proposed. The inconsistency between theoretical and experimental results is an inevitable problem. Theoretical calculation is a good strategy, which can selectively predict the choice of the best catalyst to save time and labor costs. (6) These questions deserve further investigation that whether all OER electrocatalysts can undergo structural reconstruction and whether the pathway of the reconstruction process is single. How to effectively control the surface structure reconstruction process to optimize the electrocatalyst to obtain the enhanced OER performance is still a huge challenge. (7) Developing more advanced interface engineering, intrinsic defect structure, interface engineering and catalyst electrolyte interface regulation to accurately identify the real catalytic active sites and explore the intrinsic catalytic activity of catalysts will become the research hotspot of OER. With the efforts of scientific researchers and technical workers, it is believed that self-supporting materials will achieve gratifying results in the renewable energy industrial revolution to solve the problems of environmental pollution and energy shortage.

Acknowledgements

This work was supported by the National Natural Science Foundation of China (No. 22075099), the Natural Science Foundation of Jilin Province (No. 20220101051JC), and the Education Department of Jilin Province (No. JJKH20220967KJ).

References

[1] Li, S. S.; Gao, Y. Q.; Li, N.; Ge, L.; Bu, X. H.; Feng, P. Y. Transition metal-based bimetallic MOFs and MOF-derived catalysts for electrochemical oxygen evolution reaction. *Energy Environ. Sci.* **2021**, *14*, 1897–1927.

[2] Xie, X. H.; Du, L.; Yan, L. T.; Park, S.; Qiu, Y.; Sokolowski, J.; Wang, W.; Shao, Y. Y. Oxygen evolution reaction in alkaline environment: Material challenges and solutions. *Adv. Funct. Mater.* **2022**, *32*, 2110036.

[3] Zhang, Y.; Zhu, X. J.; Zhang, G. L.; Shi, P. D.; Wang, A. L. Rational catalyst design for oxygen evolution under acidic conditions: Strategies toward enhanced electrocatalytic performance. *J. Mater. Chem. A* **2021**, *9*, 5890–5914.

[4] Wang, J.; Kong, H.; Zhang, J. Y.; Hao, Y.; Shao, Z. P.; Ciucci, F. Carbon-based electrocatalysts for sustainable energy applications. *Prog. Mater Sci.* **2021**, *116*, 100717.

[5] Kang, Z. M.; Khan, M. A.; Gong, Y. M.; Javed, R.; Xu, Y.; Ye, D. X.; Zhao, H. B.; Zhang, J. J. Recent progress of MXenes and MXene-based nanomaterials for the electrocatalytic hydrogen evolution reaction. *J. Mater. Chem. A* **2021**, *9*, 6089–6108.

[6] Shiraz, H. G.; Crispin, X.; Berggren, M. Transition metal sulfides for electrochemical hydrogen evolution. *Int. J. Hydrogen Energy* **2021**, *46*, 24060–24077.

[7] Xu, Q. C.; Zhang, J. H.; Zhang, H. X.; Zhang, L. Y.; Chen, L.; Hu, Y. J.; Jiang, H.; Li, C. Z. Atomic heterointerface engineering overcomes the activity limitation of electrocatalysts and promises highly-efficient alkaline water splitting. *Energy Environ. Sci.* **2021**, *14*, 5228–5259.

[8] Han, J. Y.; Zhang, M. Z.; Bai, X.; Duan, Z. Y.; Tang, T. M.; Guan, J. Q. Mesoporous Mn-Fe oxyhydroxides for oxygen evolution. *Inorg. Chem. Front.* **2022**, *9*, 3559–3565.

[9] Zhang, S. L.; Sun, L.; Fan, Q. N.; Zhang, F. L.; Wang, Z. J.; Zou, J. S.; Zhao, S. Y.; Mao, J. F.; Guo, Z. P. Challenges and prospects of lithium-CO_2 batteries. *Nano Res. Energy* **2022**, *1*, 9120001.

[10] Chen, Q. R.; Yu, Y. H.; Li, J.; Nan, H. X.; Luo, S. X.; Jia, C. M.; Deng, P. L.; Zhong, S. K.; Tian, X. L. Recent progress in layered double hydroxide-based electrocatalyst for hydrogen evolution reaction. *ChemElectroChem* **2022**, *9*, e202101387.

[11] Xia, H.; Shi, Z. D.; Gong, C. S.; He, Y. M. Recent strategies for activating the basal planes of transition metal dichalcogenides towards hydrogen production. *J. Mater. Chem. A* **2022**, *10*, 19067–19089.

[12] Zhang, L. S.; Shi, Z.; Lin, Y. P.; Chong, F. L.; Qi, Y. H. Design strategies for large current density hydrogen evolution reaction. *Front. Chem.* **2022**, *10*, 866415.

[13] Bai, X.; Guan, J. Q. MXenes for electrocatalysis applications: Modification and hybridization. *Chin. J. Catal.* **2022**, *43*, 2057–2090.

[14] Tang, T. M.; Li, S. S.; Sun, J. R.; Wang, Z. L.; Guan, J. Q. Advances and challenges in two-dimensional materials for oxygen evolution. *Nano Res.* **2022**, *15*, 8714–8750.

[15] Lamy, C.; Millet, P. A critical review on the definitions used to calculate the energy efficiency coefficients of water electrolysis cells working under near ambient temperature conditions. *J. Power Sources* **2020**, *447*, 227350.

[16] Andaveh, R.; Barati Darband, G.; Maleki, M.; Sabour Rouhaghdam, A. Superaerophobic/superhydrophilic surfaces as advanced electrocatalysts for the hydrogen evolution reaction: A comprehensive review. *J. Mater. Chem. A* **2022**, *10*, 5147–5173.

[17] Liu, X.; Zhang, X. Y.; Li, D. S.; Zhang, S. Q.; Zhang, Q. C. Recent advances in the “on-off” approaches for on-demand liquid-phase hydrogen evolution. *J. Mater. Chem. A* **2021**, *9*, 18164–18174.

[18] Mao, M.; Xu, J.; Li, L. J.; Zhao, S.; Li, X. H. The p-n heterojunction constructed by $NiMnO_3$ nanoparticles and Ni_3S_4 to promote charge separation and efficient catalytic hydrogen evolution. *Int. J. Hydrogen Energy* **2021**, *46*, 23190–23204.

[19] Zhang, H. Y.; Song, F. Recent advances in photo-assisted electrocatalysts for energy conversion. *J. Mater. Chem. A* **2021**, *9*, 27193–27214.

[20] Li, R. P.; Li, Y.; Yang, P. X.; Wang, D.; Xu, H.; Wang, B.; Meng, F.; Zhang, J. Q.; An, M. Z. Electrodeposition: Synthesis of advanced transition metal-based catalyst for hydrogen production via electrolysis of water. *J. Energy Chem.* **2021**, *57*, 547–566.

[21] Li, Y. Z.; Niu, S. Q.; Rakov, D.; Wang, Y.; Cabán-Acevedo, M.; Zheng, S. J.; Song, B.; Xu, P. Metal organic framework-derived CoPS/N-doped carbon for efficient electrocatalytic hydrogen evolution. *Nanoscale* **2018**, *10*, 7291–7297.

[22] Chen, F. Y.; Wu, Z. Y.; Adler, Z.; Wang, H. T. Stability challenges of electrocatalytic oxygen evolution reaction: From mechanistic understanding to reactor design. *Joule* **2021**, *5*, 1704–1731.

[23] Tang, T. M.; Wang, Z. L.; Guan, J. Q. Electronic structure regulation of single-site M-N-C electrocatalysts for carbon dioxide reduction. *Acta Phys. Chim. Sin.* **2023**, *39*, 2208033.

[24] Meng, L.; Li, L. Recent research progress on operational stability of metal oxide/sulfide photoanodes in photoelectrochemical cells. *Nano Res. Energy* **2022**, *1*, 9120020.

[25] Liu, J. L.; Zhu, D. D.; Zheng, Y.; Vasileff, A.; Qiao, S. Z. Self-supported earth-abundant nanoarrays as efficient and robust electrocatalysts for energy-related reactions. *ACS Catal.* **2018**, *8*, 6707–6732.

[26] Lian, Y. B.; Sun, H.; Wang, X. B.; Qi, P. W.; Mu, Q. Q.; Chen, Y. J.; Ye, J.; Zhao, X. H.; Deng, Z.; Peng, Y. Carved nanoframes of cobalt-iron bimetal phosphide as a bifunctional electrocatalyst for efficient overall water splitting. *Chem. Sci.* **2019**, *10*, 464–474.

[27] Yao, D. X.; Gu, L. L.; Zuo, B.; Weng, S.; Deng, S. W.; Hao, W. J. A strategy for preparing high-efficiency and economical catalytic

electrodes toward overall water splitting. *Nanoscale* **2021**, *13*, 10624–10648.
[28] Bai, X.; Wang, L. M.; Nan, B.; Tang, T. M.; Niu, X. D.; Guan, J. Q. Atomic manganese coordinated to nitrogen and sulfur for oxygen evolution. *Nano Res.* **2022**, *15*, 6019–6025.
[29] Wang, W. F.; Yang, Z.; Jiao, F. X.; Gong, Y. Q. (P, W)-codoped MoO_2 nanoflowers on nickel foam as an efficient bifunctional electrocatalyst for overall water splitting. *Appl Surf Sci.* **2020**, *529*, 146987.
[30] Zhang, Q. Q.; Qi, H.; Hou, C. M.; Liu, N.; Guan, J. Q. High-performance Fe-Co-Sn oxide electrocatalysts for oxygen evolution reaction. *Mater. Today Energy* **2019**, *14*, 100364.
[31] Luo, J.; Guo, W. H.; Zhang, Q.; Wang, X. H.; Shen, L.; Fu, H. C.; Wu, L. L.; Chen, X. H.; Luo, H. Q.; Li, N. B. One-pot synthesis of Mn-Fe bimetallic oxide heterostructures as bifunctional electrodes for efficient overall water splitting. *Nanoscale* **2020**, *12*, 19992–20001.
[32] Yang, Y. Y.; Zhu, C. M.; Zhang, Y.; Xie, Y. D.; Lv, L. W.; Chen, W. L.; He, Y. Y.; Hu, Z. Construction of Co_3O_4/Fe_2O_3 nanosheets on nickel foam as efficient electrocatalyst for the oxygen evolution reaction. *J. Phys. Chem. Solids* **2021**, *148*, 109680.
[33] Li, S. S.; Sun, J. R.; Guan, J. Q. Strategies to improve electrocatalytic and photocatalytic performance of two-dimensional materials for hydrogen evolution reaction. *Chin. J. Catal.* **2021**, *42*, 511–556.
[34] Youn, D. H.; Park, Y. B.; Kim, J. Y.; Magesh, G.; Jang, Y. J.; Lee, J. S. One-pot synthesis of NiFe layered double hydroxide/reduced graphene oxide composite as an efficient electrocatalyst for electrochemical and photoelectrochemical water oxidation. *J. Power Sources* **2015**, *294*, 437–443.
[35] Li, D. D.; Hao, G. Y.; Guo, W. J.; Liu, G.; Li, J. P.; Zhao, Q. Highly efficient Ni nanotube arrays and Ni nanotube arrays coupled with NiFe layered-double-hydroxide electrocatalysts for overall water splitting. *J. Power Sources* **2020**, *448*, 227434.
[36] Yang, J. H.; Xu, X. H.; Chen, M. M.; Yang, D.; Lu, H. Y.; Sun, Y. Z.; Shao, C.; Song, Q. Q.; Zhang, J.; Gao, L. et al. Morphology-controllable nanocrystal β-$Ni(OH)_2$/NF designed by hydrothermal etching method as high-efficiency electrocatalyst for overall water splitting. *J. Electroanal. Chem.* **2021**, *882*, 115035.
[37] Han, J. Y.; Guan, J. Q. Multicomponent transition metal oxides and (oxy)hydroxides for oxygen evolution. *Nano Res.* **2023**, *16*, 1913–1966.
[38] Wang, S.; Xue, W. D.; Fang, Y.; Li, Y. Q.; Yan, L. L.; Wang, W. J.; Zhao, R. Bismuth activated succulent-like binary metal sulfide heterostructure as a binder-free electrocatalyst for enhanced oxygen evolution reaction. *J. Colloid Interface Sci.* **2020**, *573*, 150–157.
[39] Yang, Y. Y.; Meng, H. X.; Kong, C.; Yan, S. H.; Ma, W. X.; Zhu, H.; Ma, F. Q.; Wang, C. J.; Hu, Z. A. Heterogeneous Ni_3S_2@$FeNi_2S_4$@NF nanosheet arrays directly used as high efficiency bifunctional electrocatalyst for water decomposition. *J. Colloid Interface Sci.* **2021**, *599*, 300–312.
[40] Fan, A. R.; Hou, T. Y.; Sun, X. H.; Xie, D. L.; Li, X.; Zhang, N.; Guo, J. Z.; Jin, S. B.; Zhou, Y. M.; Cai, S. et al. One-pot hydrothermal synthesis of ZnS nanospheres anchored on 3D conductive MWCNTs networks as high-rate and cold-resistant anode materials for sodium-ion batteries. *ChemElectroChem* **2020**, *7*, 1904–1913.
[41] Yang, Y. Y.; Meng, H. X.; Yan, S. H.; Zhu, H.; Ma, W. X.; Wang, C. J.; Ma, F. Q.; Hu, Z. The *in-situ* construction of NiFe sulfide with nanoarray structure on nickel foam as efficient bifunctional electrocatalysts for overall water splitting. *J. Alloys Compd.* **2021**, *874*, 159874.
[42] Wang, N.; Li, L. G.; Zhao, D. K.; Kang, X. W.; Tang, Z. H.; Chen, S. W. Graphene composites with cobalt sulfide: Efficient trifunctional electrocatalysts for oxygen reversible catalysis and hydrogen production in the same electrolyte. *Small* **2017**, *13*, 1701025.
[43] Li, Y.; Zhao, Y.; Li, F. M.; Dang, Z. Y.; Gao, P. Q. Ultrathin NiSe nanosheets on Ni foam for efficient and durable hydrazine-assisted electrolytic hydrogen production. *ACS Appl. Mater. Interfaces* **2021**, *13*, 34457–34467.
[44] Guo, K. L.; Wang, Y. T.; Yang, S. Z.; Huang, J. F.; Zou, Z. H.; Pan, H. R.; Shinde, P. S.; Pan, S. L.; Huang, J. E.; Xu, C. L. Bonding interface boosts the intrinsic activity and durability of NiSe@Fe_2O_3 heterogeneous electrocatalyst for water oxidation. *Sci. Bull.* **2021**, *66*, 52–61.
[45] Das, M.; Kumar, G.; Dey, R. S. Electrochemical growth and formation mechanism of Cu_2Se/$CoSe_2$-based bifunctional electrocatalyst: A strategy for the development of efficient material toward water electrolysis. *ACS Appl. Energy Mater.* **2022**, *5*, 3915–3925.
[46] Hu, C. S.; Chen, J.; Wang, Y. Q.; Huang, Y.; Wang, S. T. A telluride-doped porous carbon as highly efficient bifunctional catalyst for rechargeable Zn-air batteries. *Electrochim. Acta* **2022**, *404*, 139606.
[47] Hu, L. Y.; Zeng, X.; Wei, X. Q.; Wang, H. J.; Wu, Y.; Gu, W. L.; Shi, L.; Zhu, C. Z. Interface engineering for enhancing electrocatalytic oxygen evolution of NiFe LDH/NiTe heterostructures. *Appl. Catal. B:Environ.* **2020**, *273*, 119014.
[48] Guo, P.; Cao, S. F.; Wang, Y. J.; Lu, X. Q.; Zhang, Y. Z.; Xin, X.; Chi, X.; Yu, X. J.; Tojiboyev, I.; Salari, H. et al. Surface self-reconstruction of telluride induced by *in-situ* cathodic electrochemical activation for enhanced water oxidation performance. *Appl. Catal. B:Environ.* **2022**, *310*, 121355.
[49] Chen, Z. L.; Chen, M.; Yan, X. X.; Jia, H. X.; Fei, B.; Ha, Y.; Qing, H.; Yang, H. Y.; Liu, M.; Wu, R. B. Vacancy occupation-driven polymorphic transformation in cobalt ditelluride for boosted oxygen evolution reaction. *ACS Nano* **2020**, *14*, 6968–6979.
[50] Papaderakis, A.; Matouli, I.; Spyridou, O. N.; Grammenos, A. O.; Banti, A.; Touni, A.; Pliatsikas, N.; Patsalas, P.; Sotiropoulos, S. Ternary IrO_2-Pt-Ni deposits prepared by galvanic replacement as bifunctional oxygen catalysts. *J. Electroanal. Chem.* **2020**, *877*, 114499.
[51] Rivera-Gavidia, L. M.; Fernández De La Puente, I.; Hernández-Rodríguez, M. A.; Celorrio, V.; Sebastián, D.; Lázaro, M. J.; Pastor, E.; García, G. Bi-functional carbon-based catalysts for unitized regenerative fuel cells. *J. Catal.* **2020**, *387*, 138–144.
[52] Tang, T. M.; Duan, Z. Y.; Baimanov, D.; Bai, X.; Liu, X. Y.; Wang, L. M.; Wang, Z. L.; Guan, J. Q. Synergy between isolated Fe and Co sites accelerates oxygen evolution. *Nano Res.* **2023**, *16*, 2218–2223.
[53] Peugeot, A.; Creissen, C. E.; Schreiber, M. W.; Fontecave, M. Advancing the anode compartment for energy efficient CO_2 reduction at neutral pH. *ChemElectroChem* **2021**, *8*, 2726–2736.
[54] Yang, G. Q.; Yu, S. L.; Li, Y. F.; Li, K.; Ding, L.; Xie, Z. Q.; Wang, W. T.; Dohrmann, Y.; Zhang, F. Y. A simple convertible electrolyzer in membraneless and membrane-based modes for understanding water splitting mechanism. *J. Power Sources* **2021**, *487*, 229353.
[55] Kwon, J.; Han, H.; Choi, S.; Park, K.; Jo, S.; Paik, U.; Song, T. Current status of self-supported catalysts for robust and efficient water splitting for commercial electrolyzer. *ChemCatChem* **2019**, *11*, 5898–5912.
[56] Wang, P. C.; Jia, T.; Wang, B. G. A critical review: 1D/2D nanostructured self-supported electrodes for electrochemical water splitting. *J. Power Sources* **2020**, *474*, 228621.
[57] Wu, L. B.; Yu, L.; Xiao, X.; Zhang, F. H.; Song, S. W.; Chen, S.; Ren, Z. F. Recent advances in self-supported layered double hydroxides for oxygen evolution reaction. *Research* **2020**, *2020*, 3976278.
[58] Liu, W. W.; Lu, C. X.; Wang, X. L.; Liang, K.; Tay, B. K. In situ fabrication of three-dimensional, ultrathin graphite/carbon nanotube/NiO composite as binder-free electrode for high-performance energy storage. *J. Mater. Chem. A* **2015**, *3*, 624–633.
[59] Chen, G. F.; Ma, T. Y.; Liu, Z. Q.; Li, N.; Su, Y. Z.; Davey, K.; Qiao, S. Z. Efficient and stable bifunctional electrocatalysts Ni/Ni_xM_y (M = P, S) for overall water splitting. *Adv. Funct. Mater.* **2016**, *26*, 3314–3323.
[60] Guo, Y.; Zhou, S.; Zhao, J. J. Oxidation behaviors of two-dimensional metal chalcogenides. *ChemNanoMat* **2020**, *6*, 838–849.
[61] Bai, X.; Duan, Z. Y.; Nan, B.; Wang, L. M.; Tang, T. M.; Guan, J.

Q. Unveiling the active sites of ultrathin Co-Fe layered double hydroxides for the oxygen evolution reaction. *Chin. J. Catal.* **2022**, *43*, 2240–2248.
[62] Han, J. Y.; Guan, J. Q. A macro library for monatomic catalysts. *Chin. J. Catal.* **2023**, *44*, 1–3.
[63] Sun, H. M.; Yan, Z. H.; Liu, F. M.; Xu, W. C.; Cheng, F. Y.; Chen, J. Self-supported transition-metal-based electrocatalysts for hydrogen and oxygen evolution. *Adv. Mater.* **2020**, *32*, 1806326.
[64] Zhao, Y.; Wei, S. Z.; Pan, K. M.; Dong, Z. L.; Zhang, B.; Wu, H. H.; Zhang, Q. B.; Lin, J. P.; Pang, H. Self-supporting transition metal chalcogenides on metal substrates for catalytic water splitting. *Chem. Eng. J.* **2021**, *421*, 129645.
[65] Tang, T. M.; Wang, Z. L.; Guan, J. Q. Optimizing the electrocatalytic selectivity of carbon dioxide reduction reaction by regulating the electronic structure of single-atom M-N-C materials. *Adv. Funct. Mater.* **2022**, *32*, 2111504.
[66] Bai, X.; Guan, J. Applications of MXene-based single-atom catalysts. *Small Struct.* **2023**, 2200354.
[67] Bagheri, R.; Hussain, N.; Wattoo, A. G.; Assefi Pour, R.; Xu, C.; Song, Z. L. Introducing a self-improving catalyst for hydrogen evolution and efficient catalyst for oxygen evolution reaction. *J. Mol. Liq.* **2021**, *334*, 116511.
[68] Liu, J. L.; Zhu, D. D.; Ling, T.; Vasileff, A.; Qiao, S. Z. S-NiFe_2O_4 ultra-small nanoparticle built nanosheets for efficient water splitting in alkaline and neutral pH. *Nano Energy* **2017**, *40*, 264–273.
[69] Shit, S.; Chhetri, S.; Jang, W.; Murmu, N. C.; Koo, H.; Samanta, P.; Kuila, T. Cobalt sulfide/nickel sulfide heterostructure directly grown on nickel foam: An efficient and durable electrocatalyst for overall water splitting application. *ACS Appl. Mater. Interfaces* **2018**, *10*, 27712–27722.
[70] Jayaramulu, K.; Masa, J.; Tomanec, O.; Peeters, D.; Ranc, V.; Schneemann, A.; Zboril, R.; Schuhmann, W.; Fischer, R. A. Nanoporous nitrogen-doped graphene oxide/nickel sulfide composite sheets derived from a metal-organic framework as an efficient electrocatalyst for hydrogen and oxygen evolution. *Adv. Funct. Mater.* **2017**, *27*, 1700451.
[71] Jiang, J. Y.; Yan, C. Y.; Zhao, X. H.; Luo, H. X.; Xue, Z. M.; Mu, T. C. A PEGylated deep eutectic solvent for controllable solvothermal synthesis of porous $NiCo_2S_4$ for efficient oxygen evolution reaction. *Green Chem.* **2017**, *19*, 3023–3031.
[72] Hou, J. G.; Wu, Y. Z.; Zhang, B.; Cao, S. Y.; Li, Z. W.; Sun, L. C. Rational design of nanoarray architectures for electrocatalytic water splitting. *Adv. Funct. Mater.* **2019**, *29*, 1808367.
[73] Yang, Q.; Li, T.; Lu, Z. Y.; Sun, X. M.; Liu, J. F. Hierarchical construction of an ultrathin layered double hydroxide nanoarray for highly-efficient oxygen evolution reaction. *Nanoscale* **2014**, *6*, 11789–11794.
[74] Nisar, L.; Sadaqat, M.; Hassan, A.; Babar, N. U. A.; Shah, A.; Najam-Ul-Haq, M.; Ashiq, M. N.; Ehsan, M. F.; Joya, K. S. Ultrathin CoTe nanoflakes electrode demonstrating low overpotential for overall water splitting. *Fuel* **2020**, *280*, 118666.
[75] Tang, T. M.; Zhang, Q. Q.; Bai, X.; Wang, Z. L.; Guan, J. Q. Enhanced oxygen evolution activity on mesoporous cobalt-iron oxides. *Chem. Commun.* **2021**, *57*, 11843–11846.
[76] Guan, J. Q.; Bai, X.; Tang, T. M. Recent progress and prospect of carbon-free single-site catalysts for the hydrogen and oxygen evolution reactions. *Nano Res.* **2022**, *15*, 818–837.
[77] Shi, Z. P.; Wang, X.; Ge, J. J.; Liu, C. P.; Xing, W. Fundamental understanding of the acidic oxygen evolution reaction: Mechanism study and state-of-the-art catalysts. *Nanoscale* **2020**, *12*, 13249–13275.
[78] Qiao, C.; Hao, Y. Y.; Cao, C. B.; Zhang, J. T. Transformation mechanism of high-valence metal sites for the optimization of Co- and Ni-based OER catalysts in an alkaline environment: Recent progress and perspectives. *Nanoscale* **2023**, *15*, 450–460.
[79] Yoo, J. S.; Rong, X.; Liu, Y. S.; Kolpak, A. M. Role of lattice oxygen participation in understanding trends in the oxygen evolution reaction on perovskites. *ACS Catal.* **2018**, *8*, 4628–4636.
[80] Zhang, Q. Q.; Guan, J. Q. Applications of single-atom catalysts. *Nano Res.* **2022**, *15*, 38–70.
[81] Wu, J.; Zhang, Y. Y.; Zhang, B.; Li, S. W.; Xu, P. Zn-doped CoS_2 nanoarrays for an efficient oxygen evolution reaction: Understanding the doping effect for a precatalyst. *ACS Appl. Mater. Interfaces* **2022**, *14*, 14235–14242.
[82] Ji, Q. Q.; Kong, Y.; Tan, H.; Duan, H. L.; Li, N.; Tang, B.; Wang, Y.; Feng, S. H.; Lv, L. Y.; Wang, C. et al. Operando identification of active species and intermediates on sulfide interfaced by Fe_3O_4 for ultrastable alkaline oxygen evolution at large current density. *ACS Catal.* **2022**, *12*, 4318–4326.
[83] Zhang, X. Y.; Yu, W. L.; Zhao, J.; Dong, B.; Liu, C. G.; Chai, Y. M. Recent development on self-supported transition metal-based catalysts for water electrolysis at large current density. *Appl. Mater. Today* **2021**, *22*, 100913.
[84] Di, J.; Yan, C.; Handoko, A. D.; Seh, Z. W.; Li, H. M.; Liu, Z. Ultrathin two-dimensional materials for photo- and electrocatalytic hydrogen evolution. *Mater. Today* **2018**, *21*, 749–770.
[85] Cheng, H.; Zhou, H.; Zhuang, Y. Y.; Chen, B. Y.; Chen, J. F.; Yuan, A. H. Controllable synthesis and phase-dependent electrocatalytic oxygen evolution performance of CoNiFe sulfide nanocubes. *J. Alloys Compd.* **2022**, *909*, 164774.
[86] Wang, D. D.; Zhang, H.; Liu, G. Y.; Liu, Y.; Shan, D. F.; Shen, G. X.; Peng, S. L.; Wang, L. F.; Wang, X. D. Tuning the Co^{3+}/Co^{2+} ratios of the CoS_x/CNT nanocomposites for efficient oxygen evolution reaction (OER). *Mater. Lett.* **2022**, *318*, 132108.
[87] Yan, Y.; Xia, B. Y.; Zhao, B.; Wang, X. A review on noble-metal-free bifunctional heterogeneous catalysts for overall electrochemical water splitting. *J. Mater. Chem. A* **2016**, *4*, 17587–17603.
[88] Chen, M.; Hu, Y. P.; Liang, K.; Zhao, Z. M.; Luo, Y. T.; Luo, S.; Ma, J. T. Interface engineering triggered by carbon nanotube-supported multiple sulfides for boosting oxygen evolution. *Nanoscale* **2021**, *13*, 18763–18772.
[89] Shi, W. H.; Lian, J. S. Facile synthesis of copper selenide with fluffy intersected-nanosheets decorating nanotubes structure for efficient oxygen evolution reaction. *Int. J. Hydrogen Energy* **2019**, *44*, 22983–22990.
[90] Zhou, H. Q.; Yu, F.; Liu, Y. Y.; Sun, J. Y.; Zhu, Z.; He, R.; Bao, J. M.; Goddard, W. A.; Chen, S.; Ren, Z. F. Outstanding hydrogen evolution reaction catalyzed by porous nickel diselenide electrocatalysts. *Energy Environ. Sci.* **2017**, *10*, 1487–1492.
[91] Alobaid, A.; Wang, C. S.; Adomaitis, R. A. Mechanism and kinetics of HER and OER on NiFe LDH films in an alkaline electrolyte. *J. Electrochem. Soc.* **2018**, *165*, J3395.
[92] Sadaqat, M.; Nisar, L.; Babar, N. U. A.; Hussain, F.; Ashiq, M. N.; Shah, A.; Ehsan, M. F.; Najam-Ul-Haq, M.; Joya, K. S. Zinc-telluride nanospheres as an efficient water oxidation electrocatalyst displaying a low overpotential for oxygen evolution. *J. Mater. Chem. A* **2019**, *7*, 26410–26420.
[93] Jiao, S. L.; Fu, X. W.; Wang, S. Y.; Zhao, Y. Perfecting electrocatalysts via imperfections: Towards the large-scale deployment of water electrolysis technology. *Energy Environ. Sci.* **2021**, *14*, 1722–1770.
[94] Anantharaj, S.; Karthik, P. E.; Kundu, S. Petal-like hierarchical array of ultrathin $Ni(OH)_2$ nanosheets decorated with $Ni(OH)_2$ nanoburls: A highly efficient OER electrocatalyst. *Catal. Sci. Technol.* **2017**, *7*, 882–893.
[95] Xu, J. Y.; Liu, T. F.; Li, J. J.; Li, B.; Liu, Y. F.; Zhang, B. S.; Xiong, D. H.; Amorim, I.; Li, W.; Liu, L. F. Boosting the hydrogen evolution performance of ruthenium clusters through synergistic coupling with cobalt phosphide. *Energy Environ. Sci.* **2018**, *11*, 1819–1827.
[96] Manivelan, N.; Karuppanan, S.; Prabakar, K. Djurleite copper sulfide-coupled cobalt sulfide interface for a stable and efficient electrocatalyst. *ACS Appl. Mater. Interfaces* **2022**, *14*, 30812–30823.
[97] Wei, L.; Goh, K.; Birer, Ö.; Karahan, H. E.; Chang, J.; Zhai, S. L.; Chen, X. C.; Chen, Y. A hierarchically porous nickel-copper phosphide nano-foam for efficient electrochemical splitting of water. *Nanoscale* **2017**, *9*, 4401–4408.
[98] Anantharaj, S.; Ede, S. R.; Sakthikumar, K.; Karthick, K.; Mishra, S.; Kundu, S. Recent trends and perspectives in electrochemical water splitting with an emphasis on sulfide, selenide, and phosphide

catalysts of Fe, Co, and Ni: A review. *ACS Catal.* **2016**, *6*, 8069–8097.
[99] Wang, P. Y.; Qin, R.; Ji, P. X.; Pu, Z. H.; Zhu, J. W.; Lin, C.; Zhao, Y. F.; Tang, H. L.; Li, W. Q.; Mu, S. C. Synergistic coupling of Ni nanoparticles with Ni_3C nanosheets for highly efficient overall water splitting. *Small* **2020**, *16*, 2001642.
[100] Li, S. L.; Xu, C. X.; Zhou, Q. L.; Liu, Z.; Yang, Z. X.; Gu, Y.; Ma, Y. P.; Xu, W. J. Rational design of self-supported $WC/Co_3W_3N/Co$@NC yolk/shell nitrogen-doped porous carbon catalyst for highly efficient overall water splitting. *J. Alloys Compd.* **2022**, *902*, 163627.
[101] Xie, M. W.; Ma, Y.; Lin, D. M.; Xu, C. G.; Xie, F. Y.; Zeng, W. Bimetal-organic framework MIL-53(Co-Fe): An efficient and robust electrocatalyst for the oxygen evolution reaction. *Nanoscale* **2020**, *12*, 67–71.
[102] Voiry, D.; Chhowalla, M.; Gogotsi, Y.; Kotov, N. A.; Li, Y.; Penner, R. M.; Schaak, R. E.; Weiss, P. S. Best practices for reporting electrocatalytic performance of nanomaterials. *ACS Nano* **2018**, *12*, 9635–9638.
[103] Wu, Z. P.; Lu, X. F.; Zang, S. Q.; Lou, X. W. Non-noble-metal-based electrocatalysts toward the oxygen evolution reaction. *Adv. Funct. Mater.* **2020**, *30*, 1910274.
[104] Yu, R.; Wang, C.; Liu, D. M.; Wu, Z. Y.; Li, J.; Du, Y. K. Bimetallic sulfide particles incorporated in Fe/Co-based metal-organic framework ultrathin nanosheets toward boosted electrocatalysis of the oxygen evolution reaction. *Inorg. Chem. Front.* **2022**, *9*, 3130–3137.
[105] Niu, S.; Jiang, W. J.; Wei, Z. X.; Tang, T.; Ma, J. M.; Hu, J. S.; Wan, L. J. Se-doping activates FeOOH for cost-effective and efficient electrochemical water oxidation. *J. Am. Chem. Soc.* **2019**, *141*, 7005–7013.
[106] Rauf, M.; Pi, L. L.; Wang, J. W.; Mi, H. W.; Zhang, Q. L.; Zhang, P. X.; Ren, X. Z.; Li, Y. L. Zeolitic-imidazolate frameworks-derived Co_3S_4/NiS@Ni foam heterostructure as highly efficient electrocatalyst for oxygen evolution reaction. *Int. J. Hydrogen Energy* **2022**, *47*, 13616–13628.
[107] Chen, J. L.; Wang, Y. M.; Qian, G. F.; Yu, T. Q.; Wang, Z. L.; Luo, L.; Shen, F.; Yin, S. B. In situ growth of volcano-like FeIr alloy on nickel foam as efficient bifunctional catalyst for overall water splitting at high current density. *Chem. Eng. J.* **2021**, *421*, 129892.
[108] Zhang, Q.; Yan, D. F.; Nie, Z. Z.; Qiu, X. B.; Wang, S. Y.; Yuan, J. M.; Su, D. W.; Wang, G. X.; Wu, Z. J. Iron-doped NiCoP porous nanosheet arrays as a highly efficient electrocatalyst for oxygen evolution reaction. *ACS Appl. Energy Mater.* **2018**, *1*, 571–579.
[109] Browne, M. P.; Vasconcelos, J. M.; Coelho, J.; O'Brien, M.; Rovetta, A. A.; McCarthy, E. K.; Nolan, H.; Duesberg, G. S.; Nicolosi, V.; Colavita, P. E. et al. Improving the performance of porous nickel foam for water oxidation using hydrothermally prepared Ni and Fe metal oxides. *Sustainable Energy Fuels* **2017**, *1*, 207–216.
[110] Song, S. W.; Wang, Y. H.; Li, W.; Tian, P. F.; Zhou, S. Y.; Gao, H. W.; Tian, X. Q.; Zang, J. B. Amorphous MoS_2 coated Ni_3S_2 nanosheets as bifunctional electrocatalysts for high-efficiency overall water splitting. *Electrochim. Acta* **2020**, *332*, 135454.
[111] Hu, J.; Zhu, S. L.; Liang, Y. Q.; Wu, S. L.; Li, Z. Y.; Luo, S. Y.; Cui, Z. D. Self-supported Ni_3Se_2@NiFe layered double hydroxide bifunctional electrocatalyst for overall water splitting. *J. Colloid Interface Sci.* **2021**, *587*, 79–89.
[112] Shang, X.; Hu, W. H.; Han, G. Q.; Liu, Z. Z.; Dong, B.; Liu, Y. R.; Li, X.; Chai, Y. M.; Liu, C. G. Crystalline phase-function relationship of *in situ* growth Ni_xS_y controlled by sulfuration degree for oxygen evolution reaction. *Int. J. Hydrogen Energy* **2016**, *41*, 13032–13038.
[113] Qin, K. Q.; Wang, L. P.; Wen, S. W.; Diao, L. C.; Liu, P.; Li, J. J.; Ma, L. Y.; Shi, C. S.; Zhong, C.; Hu, W. B. et al. Designed synthesis of NiCo-LDH and derived sulfide on heteroatom-doped edge-enriched 3D rivet graphene films for high-performance asymmetric supercapacitor and efficient OER. *J. Mater. Chem. A* **2018**, *6*, 8109–8119.
[114] Guo, P.; Wu, J.; Li, X. B.; Luo, J.; Lau, W. M.; Liu, H.; Sun, X. L.; Liu, L. M. A highly stable bifunctional catalyst based on 3D $Co(OH)_2$@NCNTs@NF towards overall water-splitting. *Nano Energy* **2018**, *47*, 96–104.
[115] Xia, Z.; Sun, H.; He, X.; Sun, Z. T.; Lu, C.; Li, J.; Peng, Y.; Dou, S. X.; Sun, J. Y.; Liu, Z. F. *In situ* construction of $CoSe_2$@vertical-oriented graphene arrays as self-supporting electrodes for sodium-ion capacitors and electrocatalytic oxygen evolution. *Nano Energy* **2019**, *60*, 385–393.
[116] Zhou, J. H.; Wang, Z. G.; Yang, D. X.; Zhang, W. L.; Chen, Y. F. Free-standing S, N co-doped graphene/Ni foam as highly efficient and stable electrocatalyst for oxygen evolution reaction. *Electrochim. Acta* **2019**, *317*, 408–415.
[117] Ali, Z.; Mehmood, M.; Ahmad, J.; Malik, T. S.; Ahmad, B. *In-situ* growth of novel CNTs-graphene hybrid structure on Ni-silica nanocomposites by CVD method for oxygen evolution reaction. *Ceram. Int.* **2020**, *46*, 19158–19169.
[118] Liu, X. B.; Yue, T.; Qi, K.; Qiu, Y. B.; Xia, B. Y.; Guo, X. P. Metal-organic framework membranes: From synthesis to electrocatalytic applications. *Chin. Chem. Lett.* **2020**, *31*, 2189–2201.
[119] Wang, J.; Kim, J.; Choi, S.; Wang, H. S.; Lim, J. A review of carbon-supported nonprecious metals as energy-related electrocatalysts. *Small Methods* **2020**, *4*, 2000621.
[120] Li, H. X.; Han, X.; Zhao, W.; Azhar, A.; Jeong, S.; Jeong, D.; Na, J.; Wang, S. P.; Yu, J. X.; Yamauchi, Y. Electrochemical preparation of nano/micron structure transition metal-based catalysts for the oxygen evolution reaction. *Mater. Horiz.* **2022**, *9*, 1788–1824.
[121] Shang, X.; Yan, K. L.; Lu, S. S.; Dong, B.; Gao, W. K.; Chi, J. Q.; Liu, Z. Z.; Chai, Y. M.; Liu, C. G. Controlling electrodeposited ultrathin amorphous Fe hydroxides film on V-doped nickel sulfide nanowires as efficient electrocatalyst for water oxidation. *J. Power Sources* **2017**, *363*, 44–53.
[122] Xu, S. S.; Lv, X. W.; Zhao, Y. M.; Ren, T. Z.; Yuan, Z. Y. Engineering morphologies of cobalt oxide/phosphate-carbon nanohybrids for high-efficiency electrochemical water oxidation and reduction. *J. Energy Chem.* **2021**, *52*, 139–146.
[123] Liu, T. J.; Ding, J. W.; Su, Z. Q.; Wei, G. Porous two-dimensional materials for energy applications: Innovations and challenges. *Mater. Today Energy* **2017**, *6*, 79–95.
[124] Kwon, O.; Choi, Y.; Choi, E.; Kim, M.; Woo, Y. C.; Kim, D. W. Fabrication techniques for graphene oxide-based molecular separation membranes: Towards industrial application. *Nanomaterials* **2021**, *11*, 757.
[125] Kong, P.; Zhu, L.; Li, F. R.; Xu, G. B. Self-supporting electrode composed of SnSe nanosheets, thermally treated protein, and reduced graphene oxide with enhanced pseudocapacitance for advanced sodium-ion batteries. *ChemElectroChem* **2019**, *6*, 5642–5650.
[126] Topçu, E.; Kıranşan, K. D. Flexible and free-standing PtNLs-MoS_2/reduced graphene oxide composite paper: A high-performance rolled paper catalyst for hydrogen evolution reaction. *ChemistrySelect* **2018**, *3*, 5941–5949.
[127] Tian, W. L.; Li, H. Y.; Qin, B. C.; Xu, Y. Q.; Hao, Y. C.; Li, Y. P.; Zhang, G. X.; Liu, J. F.; Sun, X. M.; Duan, X. Tuning the wettability of carbon nanotube arrays for efficient bifunctional catalysts and Zn-air batteries. *J. Mater. Chem. A* **2017**, *5*, 7103–7110.
[128] Zhang, G. Q.; Xing, J. Y.; Zhao, Y. Y.; Yang, F. L. Hierarchical N, P co-doped graphene aerogels framework assembling vertically grown CoMn-LDH nanosheets as efficient bifunctional electrocatalyst for rechargeable Zinc-air battery. *J. Colloid Interface Sci.* **2021**, *590*, 476–486.
[129] Pittkowski, R.; Divanis, S.; Klementová, M.; Nebel, R.; Nikman, S.; Hoster, H.; Mukerjee, S.; Rossmeisl, J.; Krtil, P. Engendering unprecedented activation of oxygen evolution via rational pinning of Ni oxidation state in prototypical perovskite: Close juxtaposition of synthetic approach and theoretical conception. *ACS Catal.* **2021**, *11*, 985–997.
[130] Shudo, Y.; Fukuda, M.; Islam, M. S.; Kuroiwa, K.; Sekine, Y.; Karim, M. R.; Hayami, S. 3D porous Ni/NiO_x as a bifunctional oxygen electrocatalyst derived from freeze-dried $Ni(OH)_2$. *Nanoscale* **2021**, *13*, 5530–5535.

[131] Poorahong, S.; Harding, D. J.; Keawmorakot, S.; Siaj, M. Free standing bimetallic nickel cobalt selenide nanosheets as three-dimensional electrocatalyst for water splitting. *J. Electroanal. Chem.* **2021**, *897*, 115568.
[132] Hu, X. J.; Li, T. C.; Tang, Y. D.; Wang, Y. R.; Wang, A.; Fu, G. T.; Li, X. D.; Tang, Y. W. Hydrogel-derived honeycomb Ni_3S_4/N, P-C as an efficient oxygen evolution catalyst. *Chem. -Eur. J.* **2019**, *25*, 7561–7568.
[133] Yan, B.; Zheng, J. J.; Wang, F.; Zhao, L. Y.; Zhang, Q.; Xu, W. H.; He, S. J. Review on porous carbon materials engineered by ZnO templates: Design, synthesis and capacitance performance. *Mater. Des.* **2021**, *201*, 109518.
[134] Ma, Y. L.; Zhang, Y.; Wang, X.; Fan, M. H.; Li, K. Q.; Wang, T.; Liu, Y. L.; Huo, Q. S.; Qiao, Z. A.; Dai, S. A chelation-induced cooperative self-assembly methodology for the synthesis of mesoporous metal hydroxide and oxide nanospheres. *Nanoscale* **2018**, *10*, 5731–5737.
[135] Li, G. F.; Yu, H. M.; Wang, X. Y.; Yang, D. L.; Li, Y. K.; Shao, Z. G.; Yi, B. L. Triblock polymer mediated synthesis of Ir-Sn oxide electrocatalysts for oxygen evolution reaction. *J. Power Sources* **2014**, *249*, 175–184.
[136] Wu, Y. Y.; Li, G. D.; Liu, Y. P.; Yang, L.; Lian, X. R.; Asefa, T.; Zou, X. X. Overall water splitting catalyzed efficiently by an ultrathin nanosheet-built, hollow Ni_3S_2-based electrocatalyst. *Adv. Funct. Mater.* **2016**, *26*, 4839–4847.
[137] Riaz, M. S.; Zhao, S. W.; Dong, C. L.; Nong, S. Y.; Zhao, Y. T.; Iqbal, M. J.; Huang, F. Q. ZnO-templated selenized and phosphorized cobalt-nickel oxide microcubes as rapid alkaline water oxidation electrocatalysts. *Chem. -Eur. J.* **2020**, *26*, 1306–1313.
[138] Amer, M. S.; Arunachalam, P.; Ghanem, M. A.; Al-Shalwi, M.; Ahmad, A.; Alharthi, A. I.; Al-Mayouf, A. M. Synthesis of iron and vanadium co-doped mesoporous cobalt oxide: An efficient and robust catalysts for electrochemical water oxidation. *Int. J. Energy Res.* **2021**, *45*, 9422–9437.
[139] Feng, X. J.; Hu, Z.; Shi, Y. L.; Wang, X. T.; Hou, L. J.; Zhang, Y. L.; Ma, W. X. Construction of hierarchical nickel/cobalt iron-hydroxide and nickel/cobalt selenide nanotubes for efficient electrocatalytic water splitting. *New J. Chem.* **2020**, *44*, 7552–7560.
[140] Han, Y.; Chen, X.; Qian, C.; Zhang, X. Y.; He, W.; Ren, H. J.; Li, H. B.; Diao, G. W.; Chen, M. $Co_{0.85}Se$ nanoparticles armored by N-doped carbon layer with electronic structure regulation functions: An efficient oxygen evolution electrocatalyst. *Chem. Eng. J.* **2021**, *420*, 130461.
[141] Yan, K. L.; Qin, J. F.; Liu, Z. Z.; Dong, B.; Chi, J. Q.; Gao, W. K.; Lin, J. H.; Chai, Y. M.; Liu, C. G. Organic-inorganic hybrids-directed ternary NiFeMoS anemone-like nanorods with scaly surface supported on nickel foam for efficient overall water splitting. *Chem. Eng. J.* **2018**, *334*, 922–931.
[142] Zhang, R. L.; Duan, J. J.; Feng, J. J.; Mei, L. P.; Zhang, Q. L.; Wang, A. J. Walnut kernel-like iron-cobalt-nickel sulfide nanosheets directly grown on nickel foam: A binder-free electrocatalyst for high-efficiency oxygen evolution reaction. *J. Colloid Interface Sci.* **2021**, *587*, 141–149.
[143] Xie, N.; Ma, D. D.; Wu, X. T.; Zhu, Q. L. Facile construction of self-supported Fe-doped Ni_3S_2 nanoparticle arrays for the ultralow-overpotential oxygen evolution reaction. *Nanoscale* **2021**, *13*, 1807–1812.
[144] Chen, Q. Y.; Huang, L.; Kong, Q. Q.; An, X. G.; Wu, X. Q.; Yao, W. T.; Sun, C. H. Facile synthesis of self support Fe doped Ni_3S_2 nanosheet arrays for high performance alkaline oxygen evolution. *J. Electroanal. Chem.* **2022**, *907*, 116047.
[145] Pan, Z. Y.; Yaseen, M.; Shen, P. K.; Zhan, Y. Z. Designing highly efficient 3D porous Ni-Fe sulfide nanosheets based catalyst for the overall water splitting through component regulation. *J. Colloid Interface Sci.* **2022**, *616*, 422–432.
[146] Tang, M. Y.; Liu, Y.; Cao, H.; Zheng, Q. J.; Wei, X. J.; Lam, K. H.; Lin, D. M. Cu_2S/Ni_3S_2 ultrathin nanosheets on Ni foam as a highly efficient electrocatalyst for oxygen evolution reaction. *Int. J. Hydrogen Energy* **2022**, *47*, 3013–3021.
[147] Ren, H. N.; Yu, L. X.; Yang, L. P.; Huang, Z. H.; Kang, F. Y.; Lv, R. T. Efficient electrocatalytic overall water splitting and structural evolution of cobalt iron selenide by one-step electrodeposition. *J. Energy Chem.* **2021**, *60*, 194–201.
[148] Zhao, J.; Yang, L. N.; Li, H. Y.; Huang, T. Q.; Cheng, H.; Meng, A. L.; Lin, Y. S.; Wu, P.; Yuan, X. C.; Li, Z. J. Ni_3Se_2 nanosheets *in-situ* grown on 3D NiSe nanowire arrays with enhanced electrochemical performances for supercapacitor and efficient oxygen evolution. *Mater. Charact.* **2021**, *172*, 110819.
[149] Zhou, T. N.; Bai, J.; Gao, Y. H.; Zhao, L. X.; Jing, X. F.; Gong, Y. Q. Selenide-based 3D folded polymetallic nanosheets for a highly efficient oxygen evolution reaction. *J. Colloid Interface Sci.* **2022**, *615*, 256–264.
[150] Qian, G. F.; Mo, Y. S.; Yu, C.; Zhang, H.; Yu, T. Q.; Luo, L.; Yin, S. B. Free-standing bimetallic $CoNiTe_2$ nanosheets as efficient catalysts with high stability at large current density for oxygen evolution reaction. *Renewable Energy* **2020**, *162*, 2190–2196.
[151] Yang, L.; Xu, H. X.; Liu, H. B.; Cheng, D. J.; Cao, D. P. Active site identification and evaluation criteria of *in situ* grown CoTe and NiTe nanoarrays for hydrogen evolution and oxygen evolution reactions. *Small Methods* **2019**, *3*, 1900113.
[152] Sadaqat, M.; Manzoor, S.; Nisar, L.; Hassan, A.; Tyagi, D.; Shah, J. H.; Ashiq, M. N.; Joya, K. S.; Alshahrani, T.; Najam-Ul-Haq, M. Iron doped nickel ditelluride hierarchical nanoflakes arrays directly grown on nickel foam as robust electrodes for oxygen evolution reaction. *Electrochim. Acta* **2021**, *371*, 137830.
[153] Kim, M.; Park, D.; Kim, J. A thermoelectric generator comprising selenium-doped bismuth telluride on flexible carbon cloth with n-type thermoelectric properties. *Ceram. Int.* **2022**, *48*, 10852–10861.
[154] Pang, S. Y.; Lin, L. Y.; Shen, Y. Q.; Chen, S. S.; Chen, W.; Tan, N.; Ahmad, A.; Al-Kahtani, A. A.; Tighezza, A. M. Surface activated commercial carbon cloth as superior electrodes for symmetric supercapacitors. *Mater. Lett.* **2022**, *315*, 131985.
[155] Song, M. K.; Yim, J. H.; Baek, S. H.; Lee, J. W. A carbon cloth with a coating layer containing aluminum fluoride as an interlayer for lithium metal batteries. *Appl. Surf. Sci.* **2022**, *588*, 152935.
[156] Wang, D. S.; Li, J. M.; Li, X.; Wang, Q.; Liu, P. High performance flexible carbon cloth-based solid-state supercapacitors with redox-mediated gel electrolytes. *Appl. Surf. Sci.* **2022**, *583*, 152397.
[157] Wu, X. Y.; Wang, C. C.; Wang, Z.; Qin, Y.; Kong, Y. Nanostructured Co_9S_8/polypyrrole hybrids grown on carbon cloth for battery-type supercapacitor electrode. *Synth. Met.* **2022**, *286*, 117034.
[158] Qian, H.; Wu, B. X.; Nie, Z. W.; Liu, T. T.; Liu, P.; He, H.; Wu, J. H.; Chen, Z. Y.; Chen, S. G. A flexible Ni_3S_2/Ni@CC electrode for high-performance battery-like supercapacitor and efficient oxygen evolution reaction. *Chem. Eng. J.* **2021**, *420*, 127646.
[159] Jiang, S.; Shao, H.; Cao, G. Y.; Li, H.; Xu, W. L.; Li, J. L.; Fang, J.; Wang, X. G. Waste cotton fabric derived porous carbon containing Fe_3O_4/NiS nanoparticles for electrocatalytic oxygen evolution. *J. Mater. Sci. Technol.* **2020**, *59*, 92–99.
[160] Zhan, C. H.; Liu, Z.; Zhou, Y.; Guo, M. L.; Zhang, X. L.; Tu, J. C.; Ding, L.; Cao, Y. Triple hierarchy and double synergies of NiFe/Co_9S_8/carbon cloth: A new and efficient electrocatalyst for the oxygen evolution reaction. *Nanoscale* **2019**, *11*, 3378–3385.
[161] Li, Y. J.; Mao, Z. F.; Wang, Q.; Li, D. B.; Wang, R.; He, B. B.; Gong, Y. S.; Wang, H. W. Hollow nanosheet array of phosphorus-anion-decorated cobalt disulfide as an efficient electrocatalyst for overall water splitting. *Chem. Eng. J.* **2020**, *390*, 124556.
[162] Yan, Q.; Yan, P.; Wei, T.; Wang, G. L.; Cheng, K.; Ye, K.; Zhu, K.; Yan, J.; Cao, D. X.; Li, Y. J. A highly efficient and durable water splitting system: Platinum sub-nanocluster functionalized nickel-iron layered double hydroxide as the cathode and hierarchical nickel-iron selenide as the anode. *J. Mater. Chem. A* **2019**, *7*, 2831–2837.
[163] Ghosh, S.; Samanta, M.; Das, B.; Maity, S.; Howli, P.; Sarkar, S.; Chattopadhyay, K. K. Hexagonal nickel selenide nanoflakes decorated carbon fabric: An efficient binder-free water loving electrode for electrochemical water splitting. *Solid State Sci.* **2021**, *116*, 106613.
[164] Wan, Z. X.; He, Q. T.; Qu, Y.; Dong, J. X.; Shoko, E.; Yan, P. X.; Taylor Isimjan, T.; Yang, X. L. Designing coral-like Fe_2O_3-

regulated Se-rich $CoSe_2$ heterostructure as a highly active and stable oxygen evolution electrocatalyst for overall water splitting. *J. Electroanal. Chem.* **2022**, *904*, 115928.
[165] Liu, Z. Y.; He, Y. J.; Yao, C. M.; Ji, X. Y.; Zhao, B.; Gao, D. J.; Koudakan, P. A. Self-supported Cu-Ni-Se nanostuctures on carbon cloth derived from Cu-Ni-MOF nanorectangles with exceptional electrocatalytic performance for oxygen evolution reaction. *J. Phys. Chem. Solids* **2022**, *163*, 110602.
[166] Yang, L.; Qin, H. Y.; Dong, Z. H.; Wang, T. Z.; Wang, G. C.; Jiao, L. F. Metallic S-CoTe with surface reconstruction activated by electrochemical oxidation for oxygen evolution catalysis. *Small* **2021**, *17*, 2102027.
[167] Xu, J.; Yin, Y. Q.; Xiong, H. Q.; Du, X. D.; Jiang, Y. J.; Guo, W.; Wang, Z.; Xie, Z. Z.; Qu, D. Y.; Tang, H. L. et al. Improving catalytic activity of metal telluride by hybridization: An efficient Ni_3Te_2-CoTe composite electrocatalyst for oxygen evolution reaction. *Appl. Surf. Sci.* **2019**, *490*, 516–521.
[168] Wu, T. L.; Pi, M. Y.; Zhang, D. K.; Chen, S. J. 3D structured porous CoP_3 nanoneedle arrays as an efficient bifunctional electrocatalyst for the evolution reaction of hydrogen and oxygen. *J. Mater. Chem. A* **2016**, *4*, 14539–14544.
[169] Cao, N.; Chen, S.; Di, Y. M.; Li, C.; Qi, H.; Shao, Q. G.; Zhao, W. M.; Qin, Y. J.; Zang, X. B. High efficiency in overall water-splitting via Co-doping heterointerface-rich NiS_2/MoS_2 nanosheets electrocatalysts. *Electrochim. Acta* **2022**, *425*, 140674.
[170] Yang, H.; Lin, K. D.; Zhou, Z. H.; Peng, C. T.; Peng, S. M.; Sun, M.; Yu, L. Surface phosphorization of Ni-Co-S as an efficient bifunctional electrocatalyst for full water splitting. *Dalton Trans.* **2021**, *50*, 16578–16586.
[171] Guo, Y. J.; Guo, D.; Ye, F.; Wang, K.; Shi, Z. Q. Synthesis of lawn-like NiS_2 nanowires on carbon fiber paper as bifunctional electrode for water splitting. *Int. J. Hydrogen Energy* **2017**, *42*, 17038–17048.
[172] Li, W. R.; Zhao, H. F.; Li, H.; Wang, R. M. Fe doped NiS nanosheet arrays grown on carbon fiber paper for a highly efficient electrocatalytic oxygen evolution reaction. *Nanoscale Adv.* **2022**, *4*, 1220–1226.
[173] Huang, N.; Yan, S. F.; Yang, L.; Zhang, M. Y.; Sun, P. P.; Lv, X. W.; Sun, X. H. Morphology and defect modification on *in-situ* derived Co_9S_8-porous nitrogen-doped carbon as a bifunctional electrocatalyst for oxygen evolution and reduction. *J. Solid State Chem.* **2020**, *285*, 121185.
[174] Liu, Z. C.; Zhang, J. F.; Liu, Y. X.; Zhu, W. K.; Zhang, X. W.; Wang, Q. F. Electrodeposition of cobalt phosphosulfide nanosheets on carbon fiber paper as efficient electrocatalyst for oxygen evolution. *ChemElectroChem* **2018**, *5*, 1677–1682.
[175] Huang, Y. Z.; Huang, J. C.; Xu, K. S.; Geng, R. R. Constructing $NiSe_2@MoS_2$ nano-heterostructures on a carbon fiber paper for electrocatalytic oxygen evolution. *RSC Adv.* **2021**, *11*, 26928–26936.
[176] Sancho, H.; Zhang, Y.; Liu, L. D.; Barevadia, V. G.; Wu, S. Y.; Zhang, Y. M.; Huang, P. W.; Zhang, Y. F.; Wu, T. H.; You, W. Q. et al. $NiCo_2Se_4$ nanowires as a high-performance bifunctional oxygen electrocatalyst. *J. Electrochem. Soc.* **2020**, *167*, 056503.
[177] Ganguli, S.; Ghosh, S.; Das, S.; Mahalingam, V. Inception of molybdate as a "pore forming additive" to enhance the bifunctional electrocatalytic activity of nickel and cobalt based mixed hydroxides for overall water splitting. *Nanoscale* **2019**, *11*, 16896–16906.
[178] Zhang, L.; Xie, L. S.; Ma, M.; Qu, F. L.; Du, G.; Asiri, A. M.; Chen, L.; Sun, X. P. Co-based nanowire films as complementary hydrogen- and oxygen-evolving electrocatalysts in neutral electrolyte. *Catal. Sci. Technol.* **2017**, *7*, 2689–2694.
[179] Dong, Y. C.; Ji, S.; Wang, H.; Linkov, V.; Wang, R. F. In-site hydrogen bubble template method to prepare Ni coated metal meshes as effective bi-functional electrodes for water splitting. *Dalton Trans.* **2022**, *51*, 9681–9688.
[180] Jović, V. D.; Jović, B. M.; Lačnjevac, U. Č.; Krstajić, N. V.; Zabinski, P.; Elezović, N. R. Accelerated service life test of electrodeposited NiSn alloys as bifunctional catalysts for alkaline water electrolysis under industrial operating conditions. *J. Electroanal. Chem.* **2018**, *819*, 16–25.
[181] Li, D.; Liu, Z.; Wang, J. R.; Liu, B. P.; Qin, Y. C.; Yang, W. R.; Liu, J. Q. Hierarchical trimetallic sulfide $FeCo_2S_4$-$NiCo_2S_4$ nanosheet arrays supported on a Ti mesh: An efficient 3D bifunctional electrocatalyst for full water splitting. *Electrochim. Acta* **2020**, *340*, 135957.
[182] Zhang, J. J.; Su, H.; Wang, H. H.; Xue, Z. H.; Zhang, B.; Wei, X.; Li, X. H.; Hirano, S. I.; Chen, J. S. Constructing Ohmic contact in cobalt selenide/Ti dyadic electrode: The third aspect to promote the oxygen evolution reaction. *Nano Energy* **2017**, *39*, 321–327.
[183] Chen, H.; Gao, Y.; Ye, L.; Yao, Y. N.; Chen, X. Y.; Wei, Y.; Sun, L. C. A Cu_2Se-Cu_2O film electrodeposited on titanium foil as a highly active and stable electrocatalyst for the oxygen evolution reaction. *Chem. Commun.* **2018**, *54*, 4979–4982.
[184] Yang, W. Q.; Hua, Y. X.; Zhang, Q. B.; Lei, H.; Xu, C. Y. Electrochemical fabrication of 3D quasi-amorphous pompon-like Co-O and Co-Se hybrid films from choline chloride/urea deep eutectic solvent for efficient overall water splitting. *Electrochim. Acta* **2018**, *273*, 71–79.
[185] Zuo, Y.; Liu, Y. P.; Li, J. S.; Du, R. F.; Han, X.; Zhang, T.; Arbiol, J.; Divins, N. J.; Llorca, J.; Guijarro, N. et al. *In situ* electrochemical oxidation of Cu_2S into CuO nanowires as a durable and efficient electrocatalyst for oxygen evolution reaction. *Chem. Mater.* **2019**, *31*, 7732–7743.
[186] Yuan, C. Z.; Sun, Z. T.; Jiang, Y. F.; Yang, Z. K.; Jiang, N.; Zhao, Z. W.; Qazi, U. Y.; Zhang, W. H.; Xu, A. W. One-step *in situ* growth of iron-nickel sulfide nanosheets on FeNi alloy foils: High-performance and self-supported electrodes for water oxidation. *Small* **2017**, *13*, 1604161.
[187] Han, G. Q.; Li, X.; Liu, Y. R.; Dong, B.; Hu, W. H.; Shang, X.; Zhao, X.; Chai, Y. M.; Liu, Y. Q.; Liu, C. G. Controllable synthesis of three dimensional electrodeposited Co-P nanosphere arrays as efficient electrocatalysts for overall water splitting. *RSC Adv.* **2016**, *6*, 52761–52771.
[188] Dey, A.; Chandrabose, G.; Damptey, L. A. O.; Erakulan, E. S.; Thapa, R.; Zhuk, S.; Dalapati, G. K.; Ramakrishna, S.; Braithwaite, N. S. J.; Shirzadi, A. et al. Cu_2O/CuO heterojunction catalysts through atmospheric pressure plasma induced defect passivation. *Appl. Surf. Sci.* **2021**, *541*, 148571.
[189] Khan, M. Y.; Asim, M.; Ehsan, M. A.; Zeama, M.; Al-Tayeb, M. A.; Alshitari, W.; Khan, A. Graphitic-polytriaminopyrimidine (g-PTAP): A novel bifunctional catalyst for photoelectrochemical water splitting. *Int. J. Hydrogen Energy* **2022**, *47*, 21119–21129.
[190] Deng, S. J.; Shen, S. H.; Zhong, Y.; Zhang, K. L.; Wu, J. B.; Wang, X. L.; Xia, X. H.; Tu, J. P. Assembling Co_9S_8 nanoflakes on Co_3O_4 nanowires as advanced core/shell electrocatalysts for oxygen evolution reaction. *J. Energy Chem.* **2017**, *26*, 1203–1209.
[191] Ahamed, S. T.; Kulsi, C.; Kirti; Banerjee, D.; Srivastava, D. N.; Mondal, A. Synthesis of multifunctional CdSe and Pd quantum dot decorated CdSe thin films for photocatalytic, electrocatalytic and thermoelectric applications. *Surf. Interfaces* **2021**, *25*, 101149.
[192] Kim, E. K.; Bui, H. T.; Shrestha, N. K.; Shin, C. Y.; Patil, S. A.; Khadtare, S.; Bathula, C.; Noh, Y. Y.; Han, S. H. An enhanced electrochemical energy conversion behavior of thermally treated thin film of 1-dimensional CoTe synthesized from aqueous solution at room temperature. *Electrochim. Acta* **2018**, *260*, 365–371.
[193] Babar, N. U. A.; Joya, K. S. Spray-coated thin-film Ni-oxide nanoflakes as single electrocatalysts for oxygen evolution and hydrogen generation from water splitting. *ACS Omega* **2020**, *5*, 10641–10650.
[194] Fominski, V.; Romanov, R.; Fominski, D.; Soloviev, A.; Rubinkovskaya, O.; Demin, M.; Maksimova, K.; Shvets, P.; Goikhman, A. Performance and mechanism of photoelectrocatalytic activity of MoS_x/WO_3 heterostructures obtained by reactive pulsed laser deposition for water splitting. *Nanomaterials* **2020**, *10*, 871.
[195] Deng, S. J.; Shen, Y. B.; Xie, D.; Lu, Y. F.; Yu, X. L.; Yang, L.; Wang, X. L.; Xia, X. H.; Tu, J. P. Directional construction of Cu_2S branch arrays for advanced oxygen evolution reaction. *J. Energy Chem.* **2019**, *39*, 61–67.

[196] Huang, Z. N.; He, L. Q.; Zhang, W. B.; Huang, W. J.; Mo, Q. J.; Yang, L. C.; Fu, Q.; Gao, Q. S. Nickel sulfide-oxide heterostructured electrocatalysts: Bi-functionality for overall water splitting and *in-situ* reconstruction. *J. Colloid Interface Sci.* **2022**, *622*, 728–737.

[197] Chen, W. Z.; Zhang, M.; Liu, Y.; Yao, X. M.; Liu, P. Y.; Liu, Z. L.; He, J. L.; Wang, Y. Q. Super-hydrophilic MgO/$NiCo_2S_4$ heterostructure for high-efficient oxygen evolution reaction in neutral electrolytes. *Appl. Catal. B:Environ.* **2022**, *312*, 121432.

[198] He, W. J.; Jia, D. B.; Cheng, J. N.; Wang, F. Q.; Zhang, L.; Li, Y.; Liu, C. C.; Hao, Q. Y.; Zhao, J. L. P-doped nickel sulfide nanosheet arrays for alkaline overall water splitting. *Catal. Sci. Technol.* **2020**, *10*, 7581–7590.

[199] Zare, A.; Bayat, A.; Saievar-Iranizad, E.; Naffakh-Moosavy, H. One step preparation of Fe doped $CoSe_2$ supported on nickel foam by facile electrodeposition method as a highly efficient oxygen evolution reaction electrocatalyst. *J. Electroanal. Chem.* **2020**, *878*, 114595.

[200] Yu, X.; Xu, S. R.; Liu, X.; Cheng, X. H.; Du, Y. S.; Wu, Q. Mn-doped $NiCo_2S_4$ nanosheet array as an efficient and durable electrocatalyst for oxygen evolution reaction. *J. Alloys Compd.* **2021**, *878*, 160388.

[201] Wang, F.; Li, K.; Li, J. J.; Wolf, L. M.; Liu, K.; Zhang, H. J. A bifunctional electrode engineered by sulfur vacancies for efficient electrocatalysis. *Nanoscale* **2019**, *11*, 16658–16666.

[202] Wang, X.; Zhang, Y. W.; Si, H. N.; Zhang, Q. H.; Wu, J.; Gao, L.; Wei, X. F.; Sun, Y.; Liao, Q. L.; Zhang, Z. et al. Single-atom vacancy defect to trigger high-efficiency hydrogen evolution of MoS_2. *J. Am. Chem. Soc.* **2020**, *142*, 4298–4308.

[203] Ganesan, P.; Staykov, A.; Shu, H.; Uejima, M.; Nakashima, N. Designing an Fe^{III}-doped nickel sulfide/carbon nanotube hybrid catalyst for alkaline electrolyte membrane water electrolyzers and Zn-air battery performances. *ACS Appl. Energy Mater.* **2020**, *3*, 10961–10975.

[204] Su, H.; Song, S. J.; Gao, Y. Q.; Li, N.; Fu, Y.; Ge, L.; Song, W. Y.; Liu, J.; Ma, T. Y. In situ electronic redistribution tuning of $NiCo_2S_4$ nanosheets for enhanced electrocatalysis. *Adv. Funct. Mater.* **2022**, *32*, 2109731.

[205] Gao, Q.; Luo, W.; Ma, X. Y.; Ma, Z. M.; Li, S. J.; Gou, F. L.; Shen, W.; Jiang, Y. M.; He, R. X.; Li, M. Electronic modulation and vacancy engineering of Ni_9S_8 to synergistically boost efficient water splitting: Active vacancy-metal pairs. *Appl. Catal. B:Environ.* **2022**, *310*, 121356.

[206] Huang, S. S.; Jin, Z. Q.; Ning, P.; Gao, C. Y.; Wu, Y.; Liu, X.; Xin, P. J.; Chen, Z. X.; Jiang, Y.; Hu, Z. J. et al. Synergistically modulating electronic structure of NiS_2 hierarchical architectures by phosphorus doping and sulfur-vacancies defect engineering enables efficient electrocatalytic water splitting. *Chem. Eng. J.* **2021**, *420*, 127630.

[207] Li, J. W.; Lian, R. Q.; Wang, J. Y.; He, S.; Jiang, S. P.; Rui, Z. B. Oxygen vacancy defects modulated electrocatalytic activity of iron-nickel layered double hydroxide on Ni foam as highly active electrodes for oxygen evolution reaction. *Electrochim. Acta* **2020**, *331*, 135395.

[208] Zhu, K. Y.; Wu, T.; Li, M. R.; Lu, R. F.; Zhu, X. F.; Yang, W. S. Perovskites decorated with oxygen vacancies and Fe-Ni alloy nanoparticles as high-efficiency electrocatalysts for the oxygen evolution reaction. *J. Mater. Chem. A* **2017**, *5*, 19836–19845.

[209] Zhuang, L. Z.; Jia, Y.; Liu, H. L.; Li, Z. H.; Li, M. R.; Zhang, L. Z.; Wang, X.; Yang, D. J.; Zhu, Z. H.; Yao, X. D. Sulfur-modified oxygen vacancies in iron-cobalt oxide nanosheets: Enabling extremely high activity of the oxygen evolution reaction to achieve the industrial water splitting benchmark. *Angew. Chem., Int. Ed.* **2020**, *59*, 14664–14670.

[210] El Jaouhari, A.; Slassi, A.; Zhang, B. W.; Pershin, A.; Liu, W.; Cornil, D.; Liu, X. H.; Zhu, J. H. The role of selenium vacancies in the enhancement of electrocatalytic activity of $CoNiSe_2$ for the oxygen evolution reaction. *J. Power Sources* **2021**, *514*, 230596.

[211] Wang, P. C.; Lin, Y. Q.; Wan, L.; Wang, B. G. Autologous growth of Fe-doped $Ni(OH)_2$ nanosheets with low overpotential for oxygen evolution reaction. *Int. J. Hydrogen Energy* **2020**, *45*, 6416–6424.

[212] Zhou, M.; Wang, H. L.; Guo, S. J. Towards high-efficiency nanoelectrocatalysts for oxygen reduction through engineering advanced carbon nanomaterials. *Chem. Soc. Rev.* **2016**, *45*, 1273–1307.

[213] Zheng, X. B.; Yang, J. R.; Xu, Z. F.; Wang, Q. S.; Wu, J. B.; Zhang, E. H.; Dou, S. X.; Sun, W. P.; Wang, D. S.; Li, Y. D. Ru-Co pair sites catalyst boosts the energetics for the oxygen evolution reaction. *Angew. Chem., Int. Ed.* **2022**, *61*, e202205946.

[214] Wang, X. Y.; Zhang, W. Z. Z.; Zhang, J. L.; Wu, Z. C. Fe-doped Ni_3S_2 nanowires with surface-restricted oxidation toward high-current-density overall water splitting. *ChemElectroChem* **2019**, *6*, 4550–4559.

[215] Li, W. H.; Yang, J. R.; Wang, D. S. Long-range interactions in diatomic catalysts boosting electrocatalysis. *Angew. Chem., Int. Ed.* **2022**, *61*, e202213318.

[216] Wang, Y.; Wang, D. S.; Li, Y. D. Rational design of single-atom site electrocatalysts: From theoretical understandings to practical applications. *Adv. Mater.* **2021**, *33*, 2008151.

[217] Xu, S. R.; Du, Y. S.; Liu, X.; Yu, X.; Teng, C. L.; Cheng, X. H.; Chen, Y. F.; Wu, Q. Three-dimensional (3D) hierarchical coral-like Mn-doped Ni_2P-Ni_5P_4/NF catalyst for efficient oxygen evolution. *J. Alloys Compd.* **2020**, *826*, 154210.

[218] Liu, Y. H.; Ran, N.; Ge, R. Y.; Liu, J. J.; Li, W. X.; Chen, Y. Y.; Feng, L. Y.; Che, R. C. Porous Mn-doped cobalt phosphide nanosheets as highly active electrocatalysts for oxygen evolution reaction. *Chem. Eng. J.* **2021**, *425*, 131642.

[219] Yin, M. M.; Miao, H.; Chen, B.; Hu, R. G.; Xia, L.; Zhang, C. F.; Wang, F.; Zhang, H. C.; Yuan, J. L. Self-supported metal sulfide electrode for flexible quasi-solid-state zinc-air batteries. *J. Alloys Compd.* **2021**, *878*, 160434.

[220] Shit, S.; Bolar, S.; Murmu, N. C.; Kuila, T. Binder-free growth of nickel-doped iron sulfide on nickel foam via electrochemical deposition for electrocatalytic water splitting. *ACS Sustainable Chem. Eng.* **2019**, *7*, 18015–18026.

[221] Kang, H. Y.; Li, H.; Zhao, X. Y.; Yang, L.; Xu, S. L. Anion doped bimetallic selenide as efficient electrocatalysts for oxygen evolution reaction. *Ceram. Int.* **2020**, *46*, 2792–2797.

[222] Ding, Y. H.; Li, H. Y.; Hou, Y. Phosphorus-doped nickel sulfides/nickel foam as electrode materials for electrocatalytic water splitting. *Int. J. Hydrogen Energy* **2018**, *43*, 19002–19009.

[223] Hao, Q. Y.; Li, S. Y.; Liu, H.; Mao, J.; Li, Y.; Liu, C. C.; Zhang, J.; Tang, C. C. Dual tuning of nickel sulfide nanoflake array electrocatalyst through nitrogen doping and carbon coating for efficient and stable water splitting. *Catal. Sci. Technol.* **2019**, *9*, 3099–3108.

[224] Ashok, A.; Kumar, A.; Ponraj, J.; Mansour, S. A. Development of Co/Co_9S_8 metallic nanowire anchored on N-doped CNTs through the pyrolysis of melamine for overall water splitting. *Electrochim. Acta* **2021**, *368*, 137642.

[225] Jiang, H.; Yuan, H. T.; Zhang, L. G.; Dong, W. J.; Chang, Y. Q.; Jia, X. L.; Wang, G. A self-standing 3D heterostructured N-doped Co_4S_3/Ni_3S_2/NF for high-performance overall water splitting. *J. Electrochem. Soc.* **2021**, *168*, 076504.

[226] Jing, H. Y.; Zhu, P.; Zheng, X. B.; Zhang, Z. D.; Wang, D. S.; Li, Y. D. Theory-oriented screening and discovery of advanced energy transformation materials in electrocatalysis. *Adv. Powder Mater.* **2022**, *1*, 100013.

[227] Shi, Z. X.; Zhao, J. W.; Li, C. F.; Xu, H.; Li, G. R. Fully exposed edge/corner active sites in Fe substituted-$Ni(OH)_2$ tube-in-tube arrays for efficient electrocatalytic oxygen evolution. *Appl. Catal. B:Environ.* **2021**, *298*, 120558.

[228] Zheng, Y.; Gao, R.; Zheng, L. R.; Sun, L. M.; Hu, Z. B.; Liu, X. F. Ultrathin Co_3O_4 nanosheets with edge-enriched {111} planes as efficient catalysts for lithium-oxygen batteries. *ACS Catal.* **2019**, *9*, 3773–3782.

[229] Sun, Z. M.; He, J. L.; Yuan, M. W.; Lin, L.; Zhang, Z.; Kang, Z.; Liao, Q. L.; Li, H. F.; Sun, G. B.; Yang, X. J. et al. Li^+-clipping for edge S-vacancy MoS_2 quantum dots as an efficient bifunctional electrocatalyst enabling discharge growth of amorphous Li_2O_2 film. *Nano Energy* **2019**, *65*, 103996.

[230] Tang, B. S.; Yu, Z. G.; Seng, H. L.; Zhang, N. D.; Liu, X. X.;

Zhang, Y. W.; Yang, W. F.; Gong, H. Simultaneous edge and electronic control of MoS_2 nanosheets through Fe doping for an efficient oxygen evolution reaction. *Nanoscale* **2018**, *10*, 20113–20119.

[231] Kong, D. S.; Wang, H. T.; Cha, J. J.; Pasta, M.; Koski, K. J.; Yao, J.; Cui, Y. Synthesis of MoS_2 and $MoSe_2$ films with vertically aligned layers. *Nano Lett.* **2013**, *13*, 1341–1347.

[232] Zhang, N.; Gan, S. Y.; Wu, T. S.; Ma, W. G.; Han, D. X.; Niu, L. Growth control of MoS_2 nanosheets on carbon cloth for maximum active edges exposed: An excellent hydrogen evolution 3D cathode. *ACS Appl. Mater. Interfaces* **2015**, *7*, 12193–12202.

[233] Sadighi, Z.; Liu, J. P.; Zhao, L.; Ciucci, F.; Kim, J. K. Metallic MoS_2 nanosheets: Multifunctional electrocatalyst for the ORR, OER and Li-O_2 batteries. *Nanoscale* **2018**, *10*, 22549–22559.

[234] Lu, W. Q.; Song, Y.; Dou, M. L.; Ji, J.; Wang, F. Self-supported Ni_3S_2@MoS_2 core/shell nanorod arrays via decoration with CoS as a highly active and efficient electrocatalyst for hydrogen evolution and oxygen evolution reactions. *Int. J. Hydrogen Energy* **2018**, *43*, 8794–8804.

[235] Zeng, J. S.; Zhang, L.; Zhou, Q.; Liao, L. L.; Qi, Y.; Zhou, H. Q.; Li, D. Y.; Cai, F. M.; Wang, H.; Tang, D. S. et al. Boosting alkaline hydrogen and oxygen evolution kinetic process of tungsten disulfide-based heterostructures by multi-site engineering. *Small* **2022**, *18*, e2104624.

[236] Wang, W. Y.; Ren, X.; Hao, S.; Liu, Z. A.; Xie, F. Y.; Yao, Y. D.; Asiri, A. M.; Chen, L.; Sun, X. P. Self-templating construction of hollow amorphous $CoMoS_4$ nanotube array towards efficient hydrogen evolution electrocatalysis at neutral pH. *Chem. -Eur. J.* **2017**, *23*, 12718–12723.

[237] Ansari, M. S.; Kim, H. Enhanced electrocatalytic oxygen evolution reaction kinetics using dual-phase engineering of self-supported hierarchical $NiCoV(OH)_x$ nanowire arrays. *Fuel* **2021**, *304*, 121309.

[238] Li, X.; Kou, Z. K.; Xi, S. B.; Zang, W. J.; Yang, T.; Zhang, L.; Wang, J. Porous $NiCo_2S_4$/FeOOH nanowire arrays with rich sulfide/hydroxide interfaces enable high OER activity. *Nano Energy* **2020**, *78*, 105230.

[239] Feng, W. S.; Bu, M. M.; Kan, S. T.; Gao, X. H.; Guo, A. M.; Liu, H. T.; Deng, L. W.; Chen, W. Interfacial hetero-phase construction in nickel/molybdenum selenide hybrids to promote the water splitting performance. *Appl. Mater. Today* **2021**, *25*, 101175.

[240] Guan, X.; Sun, X.; Feng, H.; Zhang, J.; Wen, H.; Tian, W. L.; Zheng, D. C.; Yao, Y. D. Rational interface engineering of Cu_2S-CoO_x/CF enhances oxygen evolution reaction activity. *Chem. Commun.* **2020**, *56*, 13571–13574.

[241] Xu, Y.; Chai, X. J.; Ren, T. L.; Yu, H. J.; Yin, S. L.; Wang, Z. Q.; Li, X. N.; Wang, L.; Wang, H. J. Synergism of interface and electronic effects: Bifunctional N-doped Ni_3S_2/N-doped MoS_2 hetero-nanowires for efficient electrocatalytic overall water splitting. *Chem. -Eur. J.* **2019**, *25*, 16074–16080.

[242] Zhao, G. Q.; Rui, K.; Dou, S. X.; Sun, W. P. Boosting electrochemical water oxidation: The merits of heterostructured electrocatalysts. *J. Mater. Chem. A* **2020**, *8*, 6393–6405.

[243] Zhao, G. Q.; Rui, K.; Dou, S. X.; Sun, W. P. Heterostructures for electrochemical hydrogen evolution reaction: A review. *Adv. Funct. Mater.* **2018**, *28*, 1803291.

[244] Du, C.; Men, Y.; Hei, X.; Yu, J. H.; Cheng, G. Z.; Luo, W. Mo-doped Ni_3S_2 nanowires as high-performance electrocatalysts for overall water splitting. *ChemElectroChem* **2018**, *5*, 2564–2570.

[245] Zhang, J.; Wang, T.; Pohl, D.; Rellinghaus, B.; Dong, R. H.; Liu, S. H.; Zhuang, X. D.; Feng, X. L. Interface engineering of MoS_2/Ni_3S_2 heterostructures for highly enhanced electrochemical overall-water-splitting activity. *Angew. Chem., Int. Ed.* **2016**, *55*, 6702–6707.

[246] Xu, J. C.; Rong, J.; Zheng, Y. H.; Zhu, Y.; Mao, K. L.; Jing, Z. F.; Zhang, T.; Yang, D. Y.; Qiu, F. X. Construction of sheet-on-sheet hierarchical MoS_2/NiS_2 heterostructures as efficient bifunctional electrocatalysts for overall water splitting. *Electrochim. Acta* **2021**, *385*, 138438.

[247] Li, W. Q.; Wu, L.; Wu, X. C.; Shi, C.; Li, Y. L.; Zhang, L.; Mi, H. W.; Zhang, Q. L.; He, C. X.; Ren, X. Z. Regulation and mechanism study of the CoS_2/Cu_2S-NF heterojunction as highly-efficient bifunctional electrocatalyst for oxygen reactions. *Appl. Catal. B: Environ.* **2022**, *303*, 120849.

[248] Yang, Y. Q.; Mao, H.; Sun, K. S.; Ning, R.; Zheng, X. H.; Sui, J.; Cai, W. Facile synthesis of FeOOH-Ni_3S_2 nanosheet arrays on nickel foam via chemical immersion toward electrocatalytic water splitting. *ChemistrySelect* **2022**, *7*, e202103393.

[249] Wang, J. J.; Huang, J.; Chen, G. L.; Chen, W.; Li, T. T.; Meng, A. K.; Ostrikov, K. *In-situ* engineered heterostructured nickel tellur-selenide nanosheets for robust overall water splitting. *Chem. Eng. J.* **2022**, *446*, 137297.

[250] Gong, F. L.; Ye, S.; Liu, M. M.; Zhang, J. W.; Gong, L. H.; Zeng, G.; Meng, E. C.; Su, P. P.; Xie, K. F.; Zhang, Y. H. et al. Boosting electrochemical oxygen evolution over yolk–shell structured O-MoS_2 nanoreactors with sulfur vacancy and decorated Pt nanoparticles. *Nano Energy* **2020**, *78*, 105284.

[251] Liao, C. W.; Chen, S. Y.; Hsu, L. C.; Lin, C. W.; Chen, J. L.; Kuo, C. H.; Chang, Y. H. Insights into electrocatalytic oxygen evolution over hierarchical $FeCo_2S_4$ nanospheres. *ACS Sustainable Chem. Eng.* **2021**, *10*, 431–440.

[252] Ali-Löytty, H.; Louie, M. W.; Singh, M. R.; Li, L.; Sanchez Casalongue, H. G.; Ogasawara, H.; Crumlin, E. J.; Liu, Z.; Bell, A. T.; Nilsson, A. et al. Ambient-pressure XPS study of a Ni-Fe electrocatalyst for the oxygen evolution reaction. *J. Phys. Chem. C* **2016**, *120*, 2247–2253.

[253] Cao, J. H.; Lei, C. J.; Yang, B.; Li, Z. J.; Lei, L. C.; Hou, Y.; Feng, X. L. Zeolitic imidazolate framework-derived core–shell-structured CoS_2/CoS_2-N-C supported on electrochemically exfoliated graphene foil for efficient oxygen evolution. *Batteries Supercaps* **2019**, *2*, 348–354.

[254] Tan, Y. Y.; Zhang, Z. Y.; Lei, Z.; Wu, W.; Zhu, W. B.; Cheng, N. C.; Mu, S. C. Thiourea-zeolitic imidazolate framework-67 assembly derived Co-CoO nanoparticles encapsulated in N, S codoped open carbon shell as bifunctional oxygen electrocatalyst for rechargeable flexible solid Zn-air batteries. *J. Power Sources* **2020**, *473*, 228570.

[255] Li, J.; Wan, T. T.; Li, J. D.; Zhang, Z. S.; Wang, Y. J.; Liu, G. H. Three-dimensionally ordered mesoporous trimetal sulfide as efficient electrocatalyst for rechargeable zinc-air batteries. *Appl. Surf. Sci.* **2022**, *575*, 151728.

[256] Zhang, R. X.; Hu, Z. C.; Ning, T. Y.; Chen, N.; Shang, Z. B.; He, M. M.; Wu, J. B.; Shi, H. Heterophase stimulated active species evolution in iron/cobalt sulfide nanocomposites for oxygen evolution. *Colloids Surf. A:Physicochem. Eng. Aspects* **2022**, *648*, 129181.

[257] Zhang, J. C.; Zhang, D. J.; Zhang, R. C.; Zhang, N. N.; Cui, C. C.; Zhang, J. R.; Jiang, B.; Yuan, B. Q.; Wang, T. Y.; Xie, H. et al. Facile synthesis of mesoporous and thin-walled Ni-Co sulfide nanotubes as efficient electrocatalysts for oxygen evolution reaction. *ACS Appl. Energy Mater.* **2018**, *1*, 495–502.

[258] Li, Y. R.; Guo, Q. F.; Jiang, Y. M.; Shen, W.; Li, M.; He, R. X. A novel ball-in-ball hollow oxygen-incorporating cobalt sulfide spheres as high-efficient electrocatalyst for oxygen evolution reaction. *Chin. Chem. Lett.* **2021**, *32*, 755–760.

[259] Xu, Y. J.; Sumboja, A.; Groves, A.; Ashton, T.; Zong, Y.; Darr, J. A. Enhancing bifunctional catalytic activity of cobalt-nickel sulfide spinel nanocatalysts through transition metal doping and its application in secondary zinc-air batteries. *RSC Adv.* **2020**, *10*, 41871–41882.

[260] Hong, Y. R.; Mhin, S.; Kim, K. M.; Han, W. S.; Choi, H.; Ali, G.; Chung, K. Y.; Lee, H. J.; Moon, S. I.; Dutta, S. et al. Electrochemically activated cobalt nickel sulfide for an efficient oxygen evolution reaction: Partial amorphization and phase control. *J. Mater. Chem. A* **2019**, *7*, 3592–3602.

[261] Zhang, S. S.; Sun, Y. Y.; Liao, F.; Shen, Y. W.; Shi, H. X.; Shao, M. W. Co_9S_8-CuS-FeS trimetal sulfides for excellent oxygen evolution reaction electrocatalysis. *Electrochim. Acta* **2018**, *283*, 1695–1701.

[262] Nai, J. W.; Lu, Y.; Yu, X. Y. Formation of Ti-Fe mixed sulfide nanoboxes for enhanced electrocatalytic oxygen evolution. *J. Mater. Chem. A* **2018**, *6*, 21891–21895.

[263] Zhou, Y. X.; Luo, M.; Zhang, Z. C.; Li, W. R.; Shen, X. S.; Xia, W.

W.; Zhou, M.; Zeng, X. H. Iron doped cobalt sulfide derived boosted electrocatalyst for water oxidation. *Appl. Surf. Sci.* **2018**, *448*, 9–15.

[264] Adamson, W.; Jia, C.; Li, Y. B.; Zhao, C. Cobalt oxide micro flowers derived from hydrothermal synthesised cobalt sulphide pre-catalyst for enhanced water oxidation. *Electrochim. Acta* **2020**, *355*, 136802.

[265] Li, Z. J.; Wang, X. M.; Wang, X. H.; Lin, Y. S.; Meng, A. L.; Yang, L. N.; Li, Q. D. Mn-Cd-S@amorphous-Ni_3S_2 hybrid catalyst with enhanced photocatalytic property for hydrogen production and electrocatalytic OER. *Appl. Surf. Sci.* **2019**, *491*, 799–806.

[266] Zhang, R. X.; Hu, Z. C.; Cheng, S. Q.; Ke, W. T.; Ning, T. Y.; Wu, J. B.; Fu, X. Q.; Zhu, G. X. Molecular precursor route to $CuCo_2S_4$ nanosheets: A high-performance pre-catalyst for oxygen evolution and its application in Zn-air batteries. *Inorg. Chem.* **2021**, *60*, 6721–6730.

[267] Wang, M.; Dong, C. L.; Huang, Y. C.; Shen, S. H. Operando spectral and electrochemical investigation into the heterophase stimulated active species transformation in transition-metal sulfides for efficient electrocatalytic oxygen evolution. *ACS Catal.* **2020**, *10*, 1855–1864.

[268] Ding, J. T.; Ji, S.; Wang, H.; Gai, H. J.; Liu, F. S.; Linkov, V.; Wang, R. F. Mesoporous nickel-sulfide/nickel/N-doped carbon as HER and OER bifunctional electrocatalyst for water electrolysis. *Int. J. Hydrogen Energy* **2019**, *44*, 2832–2840.

[269] Guo, Y. N.; Zhou, X.; Tang, J.; Tanaka, S.; Kaneti, Y. V.; Na, J.; Jiang, B.; Yamauchi, Y.; Bando, Y.; Sugahara, Y. Multiscale structural optimization: Highly efficient hollow iron-doped metal sulfide heterostructures as bifunctional electrocatalysts for water splitting. *Nano Energy* **2020**, *75*, 104913.

[270] Tang, Y. J.; Zou, Y.; Zhu, D. D. Efficient water oxidation using an Fe-doped nickel telluride-nickel phosphide electrocatalyst by partial phosphating. *J. Mater. Chem. A* **2022**, *10*, 12438–12446.

[271] Rasmussen, F. A.; Thygesen, K. S. Computational 2D materials database: Electronic structure of transition-metal dichalcogenides and oxides. *J. Phys. Chem. C* **2015**, *119*, 13169–13183.